RCA
Review

Miniature (5 × 5 mm) Microwave Power Amplifier

Cover: All but one of the papers in this issue of *RCA Review* are concerned with microwave devices and circuits. The first four papers were presented at an IEEE Princeton Section Symposium on "GaAs FET Devices and Circuits" held at RCA Laboratories, Princeton, NJ on March 25, 1983. Our cover photo shows such a device, a GaAs FET microwave power amplifier (1 W, Ku band) designed using the computer-controlled microwave tuner described in the paper by F. Sechi, et al. The black patch in the middle of the photo is the back side of the FET, which is flip chip mounted.

RCA Review

Contents

-

Government Systems and GaAs Monolithic Components*

Kenneth J. Sleger
Naval Research Laboratory, Washington, DC 20375

Abstract—The major thrust of this paper is to present a broad brush overview of current and future applications of monolithic GaAs technology to government systems. Both analog and digital monolithic components are discussed. In addition, problem areas, future trends and various areas of uncertainty are identified. These include commercial market impact, government investment strategy, new technology, and challenges from Si technology.

Historical Background/Problem Areas

Generally speaking, the U.S. semiconductor industry has evolved from the needs of the U.S. Department of Defense (DOD). The DOD funded much of the basic research on silicon technology in the "fifties" and "sixties" which quickly expanded to serve a variety of commercial applications and needs that completely overshadowed any military market. As a result of the commercial driving force on silicon technology, virtually all (an exception would be radiation tolerance) of the military performance/cost requirements were quickly satisfied in a relatively short period of time. The silicon technology evolution covers the period from 1954 (first commercially available device) to today's VLSI devices, a period of almost 30 years.

GaAs technology has also been, with certain limited exceptions, developed on the basis of DOD needs, but only in areas where performance requirements exceeded that commonly believed achiev-

able with silicon or where fundamental band-structure features excluded silicon. Depending on device type and application, GaAs has carved out an analog performance niche beginning at about 1 GHz and extending to at least 100 GHz. Devices of interest include FETs, TEDs, IMPATTs, mixer diodes, and derivatives of these devices. This is not to say that certain silicon devices, such as bipolar transistors or IMPATTs, do not offer serious competition in certain areas of the 1-100 GHz frequency spectrum.

Unlike silicon, however, GaAs technology has evolved over the past 20 years with little to show in the way of a commercial product line. As an example, consider FETs, which are the current workhorse of both analog and digital monolithic GaAs integrated circuits (ICs). These devices, in discrete form, became commercially available in the early "seventies". However, in a monolithic format, "announced" commercial availability did not occur until 1982 and has yet to be realized. This is contrary to the silicon evolution pattern especially when one considers the plethora of advanced processing and fabrication equipment available to GaAs as a result of silicon technology evolution. It is also in contradistinction to laboratory experimental results which have demonstrated GaAs circuit functionality (dynamic and static) at up to LSI levels of complexity. The remaining paragraphs in this section attempt to shed some light on this atypical situation.

The DOD, directly or indirectly, has funded virtually all of the research and development on GaAs FETs and ICs employing these devices. There are several reasons for the government's interest in these circuits:

● Cost reduction for large buys
● Reliability (radiation tolerance)
● Performance
● Maintainability

Funding was driven by potential IC use in updating existing weapons systems and supplying building blocks for totally new systems designs. Today, the author can identify at least 40 domestic industrial firms pursuing GaAs IC development. Both commercial and military applications are being touted. However, there is a dichotomy in commercial and military GaAs markets that obviates the traditional silicon evolutionary pattern (i.e., military performance financed with commercial needs). Table 1 draws attention to this observation.

Note that potential military and commercial buys differ by at least an order of magnitude. But more striking is the performance

Table 1—A Dichotomy of Market Requirements

	Military		Commercial?
	#1	#2	
Application	Missile Seeker Phased Array Radar Expendable Decoy	Radar Warning Recvr Satellite Communications	Direct Satellite Brdcst
Quantity (No. of Chips)	10^5-10^6	10^3-10^4	10^6-10^7
Performance	Beyond State of the Art		Near State of the Art
Reliability	MTBF $>10^6$ Hours (Radar) MTBF $>10^4$ Hours (Seeker, Decoy)	MTBF 10^6-10^8 Hours	MTBF $>10^5$ Hours
Cost	$50/Chip	>$100/Chip?	$25/Chip (Single Chip Receiver)

and reliability requirements imposed by military needs. Finally, the military requirement is in many instances (say, buys below 10^4 chips) somewhat more tolerant of higher chip costs than is the commercial sector. This is based on a trade-off with performance, quantity, and reliability requirements. However, to achieve the cited military-chip cost goals, a major breakthrough will be required in manufacturing technology and in an understanding of which parameters affect circuit yield. Today's spot yields on analog ICs generally do not exceed 40%, while on digital circuits of 1000-gate complexity the yields are below 0.1% and rise to 20–30% for circuits of 100-gate complexity. Even with projected overall yields approaching 20% for 3-inch wafers, systems employing these chips will be very expensive unless further cost reduction scenarios can be devised.

In Table 1, a question mark follows the commercial market heading. This reflects the lack of a well defined commercial market for GaAs ICs. Several application areas have been identified, such as direct satellite broadcast, cellular radios, super computers, and fiber optics communications. But, in general, the commercial suppliers of GaAs products are applying their talent to established markets—discrete devices for direct and hybrid circuit application. Consequently, at present, the GaAs IC industry lacks the commercial-market driving force necessary for it to achieve IC cost reduction. Even more important, the DOD organizations funding GaAs

IC research and development are not seeking out commercial organizations that are interested in establishing commercial markets. Rather, they are funding large-systems house laboratories with well established relationships with DOD. These organizations have not addressed a commercial market and spend DOD funds primarily to insure their future position in serving government systems markets. The results of this funding relationship (besides severely limited commercial availability) are (1) many one-of-a-kind high performance circuits, (2) an almost total disregard for reproducibility, (3) total neglect of reliability issues, and (4) little emphasis on yield enhancement and process improvements. In almost all cases, these systems house laboratories fail to operate in a "silicon-like" frame of mind where wafer throughput and cost reduction are paramount, even though silicon expertise may exist in other divisions of the laboratories. At present there is no reliability base for any type of GaAs IC. This dilemma has resulted from the "attractiveness" of performing R&D work on military system monolithic circuits that results in additional development contracts. Until this relationship is changed, monolithic GaAs circuits will not become a reality in military systems. Without focussing on factors (2) to (4), plus packaging and performance, chip performance will not be relatable to effectiveness in a system.

Partly as a result of the aforementioned problem, DOD has recently begun a multi-service coordination effort to take a close look at GaAs monolithic funding. Issues being examined are (a) total funding, (b) programs, (c) program technical overlap, and (d) investment strategy. Within the Navy, the overall investment strategy for GaAs monolithic circuit development is being reorganized to include proper prioritization of systems needs, program focus to include strong system demonstration vehicles, and careful analysis of trade-offs between purely monolithic and miniature hybrid approaches for cost effective problem solution. Prior to Fiscal Year (FY) 1982, the government's investment strategy in GaAs monolithics can be best described as unfocused with a variety of programs, many of which encouraged one-of-a-kind demonstrations.

Fig. 1 shows a representation of the total DOD, NASA exploratory development funding for GaAs monolithic circuits from FY-73, when the first program was initiated by the Air Force, until the end of FY-82. Funding data past FY-82 is incomplete and, at this time, confidential to the government. Over the period FY-73 to FY-82, the total amount of funds integrates out to approximately $35 million. The total number of efforts is 55 with the following breakdown by service: Navy (30, $17.5 million); Air Force (12, $12.4 mil-
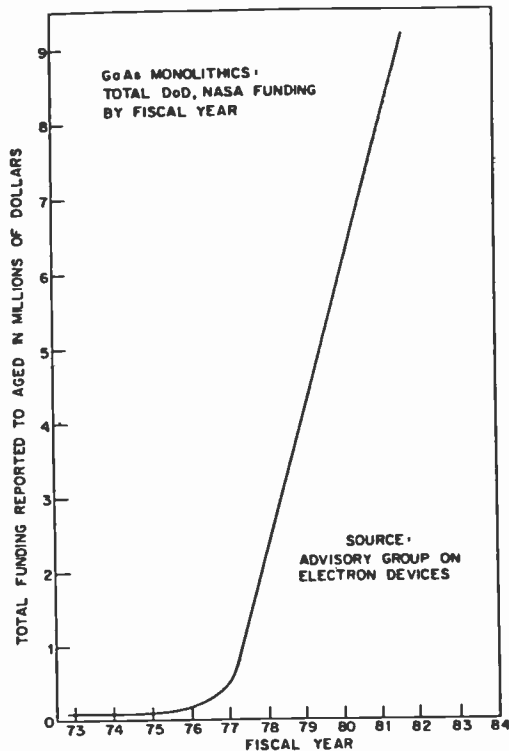
Fig. 1—DoD, NASA Investment in GaAs monolithics, principally 6.2 (exploratory development) funds.

lion); Army (9, $3.0 million); and NASA (4, $2.1 million). Fig. 1 does not, however, represent the total investment in GaAs monolithics. It is estimated that as much as $60 million may have been invested to date to cover only manpower and not capital equipment. This follows through gauging the use of capital and internal research and development funds by many companies to supplement direct government funding. As an example, the Defense Advanced Research Projects Agency (DARPA) and the Air Force have invested $12.5 million in the STRAM (Strategic and Tactical Array Module) program with an additional $20 million originating from corporate investment. Additional sources of funding also occur from advanced development programs that require GaAs IC development. Most DOD agencies are currently requesting, either directly or indirectly, corporate investment commitments of at least 30% on most GaAs IC development programs. In the future, even more corporate funding commitments will be necessary. Funding projections for FY-83 and beyond are difficult, even within the government, due

to Congressional uncertainties on the budget and lack of a coordinated DOD investment strategy.

GaAs Monolithic IC Technology Data Base

To establish a point of reference, the subject of this paper was discussed with a wide range of (1) DOD and NASA program managers having specific involvement with GaAs ICs and (2) DOD systems engineers and program managers having familiarity with a variety of current and future systems that are contenders for GaAs technology insertion. As a result of these discussions, coupled with the author's broad familiarity with the GaAs technology base, six areas are identified for the establishment of a data base that can serve as a reference point for the status of GaAs IC technology. These are:

1. The System Type and its Acronym
2. The System Technical Description
3. The Critical R and D needed to develop the Particular IC
4. The Specific Application or Function of the IC in the System
5. The Year of Implementation of the IC in the System
6. The Potential Chip Buy

In general, the aforementioned discussions tended to paint a broad-brush picture as a result of generic future-systems-needs attitude toward GaAs ICs. However, in several cases, specific requirements were cited and definite trends were derivable from the discussions.

At this point it is necessary to make some comments on the military sensitivity of the following information. It is the author's intention to cite specific systems whenever possible. In some cases, generic IC performance will be mentioned. However, citing specific performance specifications for a given chip in a given system or even citing acronyms for certain systems is disallowed either by confidentiality requests from systems engineers or by classification/ ITARS (International Traffic in Arms Regulations) restrictions.

Table 2 contains a variety of raw information obtained from GaAs IC and systems program managers. The information is arranged to address the six areas cited above. This table contains considerable detail and, in order to discuss it in a reasonable fashion, it will be necessary to abstract the following key information areas:

- High Volume Applications
- High Volume Chips
- Issues
- Areas of Uncertainty

High volume applications, those with chip counts of 10^6 or more,

were clearly identified as phased arrays (radar and communication), expendable decoys, missile seekers and satellite signal processors. The high volume chip functions are as follows:

- Transmit and Receive Functions Employed for Phased Arrays
- Monopulse Wideband Receiver Front Ends
- Multioctave, Medium Power Amplifiers
- Wideband Tunable Sources
- Millimeter Wave Receiver Front Ends
- Microwave Frequency Wideband IF Amplifiers
- Multioctave, Low Noise Amplifiers
- A/D, D/A High Speed Converters
- Cache or Scratchpad High Speed Memories
- Signal Preprocessors

Depending on chip commonality, buys for these chips could exceed the 10^6 range over a three- to five-year time period. Table 3 shows these high volume chips arranged by frequency and by system type, while Table 4 indicates service and NASA interest for GaAs technology insertion into various systems. Tables 2–4 indicate a great deal of military interest and application areas for GaAs ICs. However, this interest is tempered by areas of uncertainty and controversy encompassing a variety of technical issues. The major issues are outlined below:

Production
    Lack of Accurate Process/Device/Materials Models ⎫
    Material/Process Uniformity (Defects) ⎬ Yield
    Passive Circuit Uniformity/Models ⎭
    Limits of Ion Implantation
    Real Estate Consumption (Linear Circuits)
Devices/Circuits
    Frequency-Bandwidth ⎫
    Noise Figure ⎬ Demonstrated
    Power Consumption ⎭
    Linear Dynamic Range (Restricted)
    Functionality (e.g., FET/Varactor on a Chip)
Systems Application of IC
    Reliability (Nonexistent Data Base)
    Radiation Tolerance (Limited Data Base)
    Availability (Zero) ⎫
    Maintainability? ⎪
    Cost? ⎬ No Data Base
    Architecture? ⎪
    Size, Weight, Power ⎭

Table 2—Data Obtained from Survey to Determine Status of GaAs IC Technology

System Type	IC Description	IC Development	IC Application	Year Of Implementation	Potential Chip Buy
Satellite Signal Processor	Digital Multiplier 4K Gate Array 15 Bit/100 MHz ADC	Yield Radiation Tolerance Substrate Uniformity MT Programs Process Uniformity	Memory, Glue Digital Signal Processing	1988–1990	10^6
Communications, Navigation and Identification With Anti-Jam	Agile Bandpass Programmable Filter; High Speed CCD	Yield Radiation Tolerance? Embrionic Tech. Base	Binary-Analog Correlation For Signal Processing	1988–1990	3×10^5
Advanced Phased Array Radar	X, Ku Band Amplifier Octave Bandwidth	Yield Radiation Tolerance	Ku Band Transceiver; Mobile Ground Terminal For Satellites	1990	10^6
EW Receiver ECM	2–4 Bit, 2 GSPS ADC 4K Memory	Yield Packaging Substrate Uniformity Device Uniformity Speed	Storage Of RF Waveforms For Later Retransmission; Rapid Algorithm Execution	1985 (ADC only) 1988 (Memory)	10^3–10^4
Expendable Decoy	Multi-Octave, Medium Power Amplifier And FET Switches	Yield Reproducibility MT Programs	Use In Active Phased Array In Missile	1990–1992	10^5–10^6
Missile Seeker (Arm)	Multi Chip Acceptable Mixer Front End FET/Varactor VCO	Yield Bandwidth Multi/Device Compatibility	Superhet Monopulse Receiver 4–5 Octave Bandwidth (Microwave)	1988–1990	10^4–10^5
EW Receiver (ARM)	Broadband Passive Front End	Yield Bandwidth Integration Of Tunable LO	Radar Warning	1988–1990	10^4

Application	Circuit/Component	Technology Issues	Function	Year	Quantity
EW ESM	Wide Band Low Noise Amplifier Covering As Many As 10 Bands	Yield / Band Defining Tuned Ckts Input Multiplexing	Channelized Receiver Compatible With OTH Surveillance	1990	10^4
Satellite Communications	Medium Power, Narrow Band Amplifier With Gain/Phase Control	Material Process Yield	Transmit/Receive Module; MultiBeam/Scanning Beam Transmission; Phased Arrays	1990	10^3/Satellite
Satellite to Satellite Communications	Narrow Band, Low Noise And Amplifiers With Phase Shift Control	Efficient Power Source; Low Noise Amplifier; Yield/Reproducibility	Transmit/Receive Phased Array	1990	10^3 Modules/ Array
EW ELINT Receiver	Multi-Octave, Low Noise Front End With Image Reject	Passive Component Value Control and Modelling Reproducible, Dual Gate FET Tuning Varactor; Implant Profiles; Process Control Yield	ELINT Receiver	1988?	10^2–10^3?
Advanced EW Receivers (A-O Processor)	Optical/Electronic Conversion Using Detector Array (Analog)	High Dynamic Range High Sensitivity Yield, Reproducibility	Provide Interface Between Optical and Electrical Signal Processing (Analog)	1990	5×10^4
EW Jammer	Multi-Octave Medium Power Amplifier With RF Switch	Yield, Reproducibility, MT Program, Material/Process	Lens FED Array For Aircraft	1988	2×10^5
Generic Decoy (Expendable)	Multi-Octave Medium Power Amplifier	Yield, Reproducibility, MT Program		1988	$>10^5$
Space Based Radar	Transmit and Receive Amplifiers/Switches	Yield, Radiation Tolerance, Substrate Uniformity, MT Programs, Process Uniformity	T/R Modules Also Ground Based Application	1988–1990	10^6

Table 3—Chip Function Versus System Function for High Volume Chips (M = Microwave, m = Millimeter Wave, X = Baseband Signal Processing)

	Trans./Rec. Amplifiers	Broadband Passive Front End	Multi-octave LNA	Multi-octave Med. Power Amplifier	Wideband Tunable Source	Wideband Tunable Front End	A/D Converter	High-Speed Memory	A/D Converter
Phased Array Radars	M,m	m	M,m	M,m	M,m	M,m	X	X	X
Satellite Comms.	M,m	m					X	X	X
Jammers (ECM)				M,m	M,m		X	X	X
Missile Seekers		m	M,m	M,m	M,m	M,m	X	X	X
ECM	M,m		M,m	M,m	M,m	M,m	X	X	X
ESM Receivers		m	M,m				X	X	X
ELINT Receivers		m	M,m		M,m	M,m	X	X	X
Smart Munitions	m	m			m	m	X	X	X
Fire Control		m	M,m		m	m			
Ground Based Communications	m	m		m	m	m	X	X	X
Radiometers		M,m	M,m		M,m	M,m	X	X	X
Warning Receivers	M	m	M,m				X	X	X

Table 4—Expressed System Interest for Possible GaAs Technology Insertion

	Army	Navy	AF	NASA		Army	Navy	AF	NASA
Phased Array Radar	X	X	X	X	Fire Control	X			
Satellite Communications	X	X	X	X	Fire/Forget Weapons	X	X		
Navigation/ Communications	X	X	X	X	Passive Imaging		X	X	
Mini RPV	X	X	X		Deep Space Comm.				X
Smart Shells	X				Data Relay				X
Anti-Personnel Radar	X				Sensors				X
Expendable Decoys	X	X	X		Submunitions	X			
Missile Seekers	X	X	X		Battlefield Comm.	X			
ELINT Receiver	X	X	X		Jammers	X	X	X	
ESM Receiver	X	X	X		Digital Receiver			X	
Anti-Radiation Seeker	X	X	X		Data Handler			X	
Intersatellite Communications		X		X	Radar Warning Receiver	X	X	X	

The most pressing issue is *yield*—a key factor in determining chip cost. Most program managers are deeply concerned by the low yields presently available and suggest a greater program emphasis on determining which factors affect yield. Defect density, currently between 10^3 and 10^4 cm^{-2}, has already been cited as a serious limitation to achieving LSI digital circuit complexity. Defect density reduction and sensitivity analysis will be of great value in solving this problem.

Another important issue cited is the limits of ion implantation, especially for power ICs or millimeter wave ICs. To date, the best power results from discrete GaAs FETs (say at X and Ku Band) have not been obtained with ion implantation, but rather with epitaxial techniques. Will this trend prevail for planar ICs where the preferred dopant introduction technique is ion implantation? Will ion implantation be a viable technology for millimeter wave ICs where, for some devices, doping-layer thicknesses are less than 1000Å? Can dielectric isolation by ion implantation be equivalent to that of bulk semi-insulating GaAs? Can methods be devised to reduce real estate that is dominated by passive components at microwave frequencies? In the case of device/circuit issues, it may be observed that issues appear to be less pressing than those of pro-

duction simply because of the proliferation of "one of a kind demonstrations" in the last few years. However, significant performance improvement is still necessary, especially in linear dynamic range, which must be increased well above 50 dB for certain types of rear end signal processing.

The most complicated and demanding issue is the actual implementation of GaAs IC technology in systems. Chips must exhibit required performance and be low cost and reliable. To date, chips with these collective attributes have not been demonstrated. Current laboratory chip costs start at around $10,000/chip and extend, in some cases, to hundreds of thousands of dollars per chip. Additional problems facing system implementation include packaging and chip partitioning for optimum cost–performance trade-off. These considerations are not only issues but "areas of uncertainty". Should a miniature hybrid approach be used rather than an "all on one chip" approach? What types of packages are necessary for high speed (1-5 GSPS) GaAs digital circuits?

Future R&D programs are an area of uncertainty presently confronting DOD managers. That is, what are the appropriate programs necessary to produce high-performance, low cost, reproducible, and reliable GaAs ICs? Most current DOD thinking on this subject is directed toward devising effective manufacturing technology (MT) programs that focus on (1) reproducible performance demonstration on, say, 100–200 chips earmarked for a specific system brassboard and (2) a foundry concept similar to that being explored for silicon ICs. The Army and Navy are pursing MT programs of the first kind for analog GaAs ICs, whereas DARPA is pursuing the latter MT approach for digital GaAs ICs.

Microwave Systems Applications

Most applications for linear GaAs ICs fall into the microwave frequency range (1–30 GHz). The complexity of this type of circuit rarely exceeds the SSI level. However, fabrication procedures are demanding for FET gates, which are typically 0.25–1.0 microns long and from 100 to 10,000 microns wide. A break or short between the gate and any other metallization results in a limited yield across a wafer. An equivalent situation is rarely encountered in present day silicon technology, which for the most part does not employ such fine lines with accompanying long continuous widths. In addition, the linear device and circuit requirements impose stringent materials and process uniformity over a relatively large area. Such tight materials and process issues (when translated into chip cost) have

refocussed at least two domestic firms towards a miniature-hybrid approach for low cost GaAs circuits.

Tables 2–4 cite a variety of application areas for microwave GaAs ICs and they will not be repeated here. However, it may prove useful to mention those systems that are currently being implemented with GaAs ICs and those that are planned in the future. The Air Force is emphasizing space-based phased array radars, conformal arrays, and wideband EW systems. Some of the array work is in conjunction with DARPA. These programs are ongoing except for the conformal arrays which will begin in FY-83. The Navy is placing emphasis on wideband EW, expendable decoys, and phased array radar. GaAs IC programs are directed toward the ASPJ system (Advanced Self-Protection Jammer), MISS (Multibeam Integrated Solid State) Decoy, the Generic Decoy, and EW low and medium power TWT replacement. At present, the Army's GaAs IC programs are generic in nature with no specific system being addressed. These programs consist of a manufacturing technology effort and a monolithic doubly balanced mixer development. DARPA's emphasis is on phased array modules for space based radars (STRAM) in X and Ku bands. NASA's primary interest is in the 20/30 GHz satellite communications link. The success of some of these new systems is projected to depend entirely on the availability of low cost GaAs technology.

Millimeter Wave Systems Applications

In contrast to microwave monolithic GaAs ICs, monolithic millimeter wave ICs (MMWICs) are less complex. They require physically smaller and, therefore, more attractive lumped elements and distributed structures than their microwave counterparts. A typical envisioned MMWIC for operation at W band might consist of a mixer, local oscillator, and multiplexer (filter). At lower frequencies, such as Ka band and V band, traditional MMIC FET technology may be applicable but would be limited to short gate widths. A serious deficiency in the MMWIC technology is the lack of a monolithic or monolithically compatible three-terminal device above 60 GHz. This is so, even though inclusion of such a device and its fine line widths/vertical dimensions could presumably decrease circuit yield.

At present most of the services and DARPA are pursuing novel three-terminal solid state devices for millimeter wave sources. The DARPA EHF monolithic arrays program is a prime example of such

an effort. However, the conventional FET is still leading the device pack, with performance up to 60 GHz. Most millimeter wave applications that can make use of GaAs ICs fall into the 30–140 GHz frequency range. Above 110 GHz, GaAs begins to be challenged by InP technology and dielectric media employing nonlinear optics.

Millimeter wave systems applications are centered on intersatellite communications, anti-radiation missile seekers, fire and forget weapons, deep space communications, and passive imaging. The most desired IC is a receiver front end. The Navy has the only program pursuing such a receiver front end precursor at W band. The system application is generic at present. The Air Force has a similar W-band program that is looking at monolithic components for a receiver front end. Army applications, by far, outnumber those of other services. At present, the Army is pursuing a hybrid approach for a variety of front end implementations at V and W band.

Specific examples of Army systems that would benefit from low cost MMWICs are Advanced Indirect Fire Systems (AIFS), Terminally Guided Submissile Seeker (TGSM), Sense and Destroy Armor (SADARM), Smart Target Actuated Fire and Target (STAFF), NMW Command Guidance, Helicopter All Weather Fire Control Radar (HAWFCR), RPV radar, Advanced Fire Control Radar System (AFCORS), Mobile Intercept Resistant Radio (MISR), Multichannel Command Post Radio (MCPR), and the An/APR-33 Receiver.

Signal Processing Applications

Signal processing, either analog or digital, is of vital interest for future *smart* systems having GaAs front end sensors at either microwave or millimeter wave frequencies. Many of the existing and future systems will be impacted by VHSIC (all silicon) technology in the area of digital signal processing. In many cases, it will be necessary to provide an interface (referred to as fusion) between a GaAs front end sensor and VHSIC rear end processing. Such a fusion concept is shown in Fig. 2. The GaAs preprocessor has the possibility of performing digital or analog functions. The choice of GaAs over silicon is based only on the inability of silicon to provide the necessary high speed performance, low power consumption, and radiation tolerance required of the preprocessor. It is stressed, however, that certain preprocessor functions may be performed with silicon using parallel processing. In certain instances the preprocessor may employ complementary GaAs and Si technologies. A
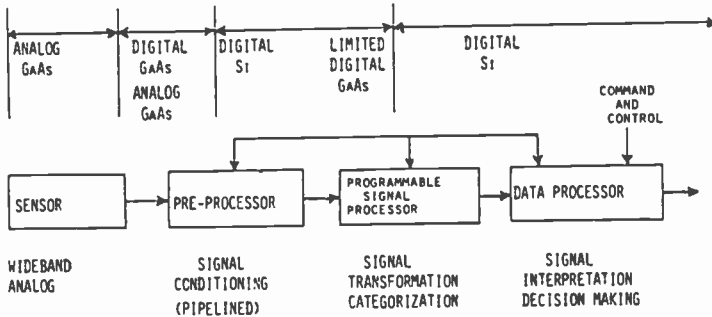
Fig. 2—Typical military "fused" system envisioned by the late 1980's and beyond.

similar situation may exist at the signal processor. However, it is believed that the use of GaAs in the processor will be more restricted than in the preprocessor. Typical preprocessor functions are digitization (A/D converter), pulse deinterleaving, channelization, data decryption, and error decoding. Typical processing functions are fast Fourier transformations, data compression, spectral filtering, and synchronization.

Unlike GaAs linear ICs, GaAs digital FET ICs have been fabricated in a variety of circuits at the MSI and LSI level of complexity with demonstrated dynamic performance and MSI yields as high as 10–20%. However, by comparison with silicon, GaAs digital ICs are still in the early stage of development and their application remains highly controversial within both the GaAs and silicon communities. This controversy stems from the uncertainty in speed advantage that GaAs may enjoy over silicon. Si NMOS circuits with submicron "effective" gate lengths have been fabricated with speed performance equivalent to one-micron gate-length GaAs FET technology. However, the contact technology of dense sub-micron silicon IC circuits is very difficult and no complex circuits have appeared on the scene.

The question of speed advantage of either GaAs or Si in the submicron regime may be moot, because in highly dense digital circuits, interline capacitance and line resistance effects may dominate and the intrinsic speed of the device will be of secondary importance. However, there are certain chip functions where GaAs may be a clear winner. One is in analog-to-digital conversion (ADC) where the level of complexity is low enough so that the full speed potential of GaAs FETs at submicron gate lengths can be utilized. The same

is true of high speed digital-to-analog converters (DAC). Digitization rates of 1–2 gigasamples per second (GSPS) with 4–6 bit accuracy are projected with GaAs ADCs. Another GaAs digital chip that is attractive for cache or scratch pad memory applications is that of a 1K–4K static RAM with access times as short as 1 nsec. This chip offers promise of low power consumption (0.25–0.5 watt for 1000-bit normally off FET) in comparison with competing silicon emitter-coupled logic (1–2 watts, 1000 bit).

Other types of digital GaAs ICs, such as gate arrays and logic functions, are more localized to specific application areas (such as the DARPA advanced on-board signal processor) and may be challenged by advanced architectural schemes involving silicon. On the other hand, where high level radiation tolerance and low power consumption is a must, GaAs may be the only choice for digital high speed circuits. Several types of GaAs digital FET ICs have shown exceptional tolerance (up to 10^7 rad) to total ionizing dose. In some cases, these circuits display upset phenomenon when subjected to transient ionizing radiation. However, this problem may be solvable through choice of undoped substrates and special processing techniques. Another potential problem which lacks a solution at present is that of single event upset in GaAs. The radiation tolerance of GaAs ICs remains an area of controversy with no immediate resolution in sight.

All services have programs in GaAs digital ICs. The Air Force has programs in memories, A/D converters, advanced EW real-time signal processors, and packaging/testing of gigabit medium-scale ICs. The Navy effort is focussed on a 1 kbit static RAM and a comparator for use in a gigabit optical ADC. The Army program is in normally-off FET gigabit logic technology, static RAMS, and an 8-bit microprocessor.

By far the driving force in exploiting digital GaAs IC technology in the U.S. is DARPA. This organization has sponsored development from substrate technology to circuit fabrication at the 1000-gate level of complexity and is currently funding a 4K static RAM effort with gate count of 16,000. DARPA also has ongoing research programs on ADCs, microprocessors and gate arrays. The driving system concept is the advanced on-board signal processor (AOSP) consisting of large networks of array computing elements (ACE). As mentioned earlier, DARPA will be initiating a substantial manufacturing technology thrust in the digital GaAs area which will have the foundry concept and cost reduction as its theme. Demonstration chips are 6K gate arrays and 64K RAMs with low power

consumption and high radiation tolerance. This program will require the solution of the yield problem for its success. Another DARPA interest is in super computers where advanced GaAs or GaAs based technology may play an important role. This thrust would challenge the super computer plan in Japan and may employ the next potential wave of GaAs FET technology, referred to as MODFET (modulation doped FET).

Analog signal processing is also an important area for GaAs. Important functions are multi-phase down converters and various active and passive filters used for multiplexing. Both CCD and SAW technology in GaAs are being examined for agile bandpass filters in such systems as ICNIA (Integrated Communication Navigational Identification Avionics) which is funded by the Air Force. In a Navy program, GaAs optical detector preprocessor arrays have already been demonstrated for use in optical spectrum analyzers for advanced-threat-warning airborne countermeasures receivers. Eventually, this system plans to make use of GaAs CCDs in the processor.

The Future

The future of GaAs ICs in military systems is dependent upon the totality of several key issues, such as performance, ultimate chip cost, chip reliability, and the impact of an as yet undefined commercial market. Table 2 clearly indicates substantial military markets. This paper has limited itself primarily to current technology thrusts, i.e., GaAs FETs embedded in a sea of passive circuits for both digital and linear functions. Although the Schottky barrier GaAs FET is a powerful tool for both digital and analog applications, it cannot serve all functions. The same may be said of GaAs. Consequently, future programs in microwave and mm wave GaAs ICs must not only emphasize reducing cost but also support the development of new devices and technologies that may or may not be GaAs or FET based.

If one extrapolates present device and circuit performance to other alloy III-V material concepts (e.g., InGaAs), to advanced circuit concepts (e.g., nodalless amplifier), to new devices (e.g., monolithic IMPATTs and hot electron emitter FETs), and to new interactive schemes (e.g., millimeter-wave/optical on-chip interactions), the possibility for even further improved performance becomes a truly exciting prospect for scientists, engineers, and systems engineers.

Acknowledgments

Some Microwave Properties of High-Speed Monolithic ICs*

K.-H. Kretschmer and H. L. Hartnagel
Institut für Hochfrequenztechnik, Technische Hochschule
Darmstadt Merckstrasse 25, 6100 Darmstadt, GFR

Abstract—In the design of high-speed logic circuits, it is essential to re-
duce electrode separation as much as possible without intro-
ducing coupling effects that cause crosstalk. Wave coupling
effects were studied using a coupled-mode analysis that in-
cludes active coupling due to transistors inserted in the lines.
Signal transfer between two parallel lines was calculated, using
a realistic TEM equivalent circuit, as a function of electrode
length normalized by the signal wavelength. It is shown that a
resonance behavior of coupling occurs that causes crosstalk
effects to be strongly dependent on conductor length.

The theoretical results are confirmed by an experimental
model consisting of LC transmission lines and transistors in-
serted at periodic intervals. The model predicts operation in
the 5–15 GHz range, but frequencies above 30 GHz are taken
into account because of harmonics of the signal pulses. It is
shown that resonance-type signal transfer between neigh-
boring conductors can be obtained by selecting certain imped-
ance-loading conditions.

1. Introduction

High-speed monolithic ICs are regularly reported now for analogue
and digital signal processing. In both cases, high packing densities
are usually required in order to reduce signal transfer delays. It is
therefore essential to approach the limits of electrode-packing den-
sities as closely as possible without crosstalk. To establish the limits
for various circuit conditions, such as the occurrence of reflections
at certain localities in the circuit, a three-line coupler analysis is
presented here. The analysis is mostly concerned with passive cou-
pling, but also includes periodic active coupling produced by tran-
sistors inserted into the circuit at regular intervals as, for example,
logic gates.

Some of the theoretical results have been modelled experimentally by using LC type transmission lines with FETs inserted at periodic intervals. The study has confirmed that resonance-type crosstalk occurs between neighbouring conductors when certain types of signal reflections exist.

Another important concern of the circuit designer is the input and output impedances of FETs, which ideally should not cause any signal reflections. So far, these impedances have been found experimentally by measuring the scattering parameters of transistors or from some semi-empirical reasoning based on the dimensional features of the transistor structures. Here, we present an extension of a previously published[1] field theoretical analysis of wave propagation on FET electrodes. With this approach, we can gain a more fundamental insight into the behaviour of various FET structures at microwave frequencies and thereby derive concepts for an optimum design.

Since digital ICs have to handle several harmonics of the signal pulses, it is important to include here frequencies well above the normal operating frequencies of MESFETs.

2. Modelling of Closely-Spaced Lines

Using the concepts outlined in Ref. [2], two parallel transmission lines are modelled by the circuit shown in Figure 1. Coupling between the lines is described by inductive and capacitive components representing the effects of magnetic and electric fields, respectively. Periodically, FETs are inserted to simulate the influence of transistors forming, for example, logic gates between the conductors. At the ends of such lines of length l, various signals are applied or extracted via loading impedances. Here the particular case is selected of feeding line 1 at one end by a signal generator with internal impedance Z_1. The other end of line 1 is terminated by an impedance Z_1, which represents a typical reflection of a wave by such features as a sharp corner in the line or a broadening of the line due, for example, to a bonding pad. Similarly, line 2 is terminated by its equivalent impedance Z_2 at both ends. Cross talk is now obtained if a signal from line 1 appears as output at either end of line 2.

Such a transfer of signal is due first to active coupling via the inserted transistors, and such transfer is likely to be intentional for a particular logic application. Unintentioned, however, is a transfer via coupling capacitors and inductors. Figure 2 gives the transfer amplitude for matched line terminations:
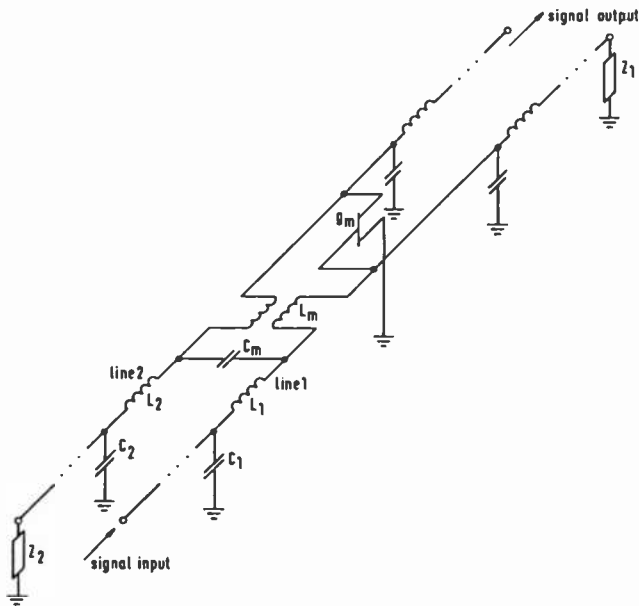
Fig. 1—Modelling of crosstalk for closely spaced conductors with reflec-
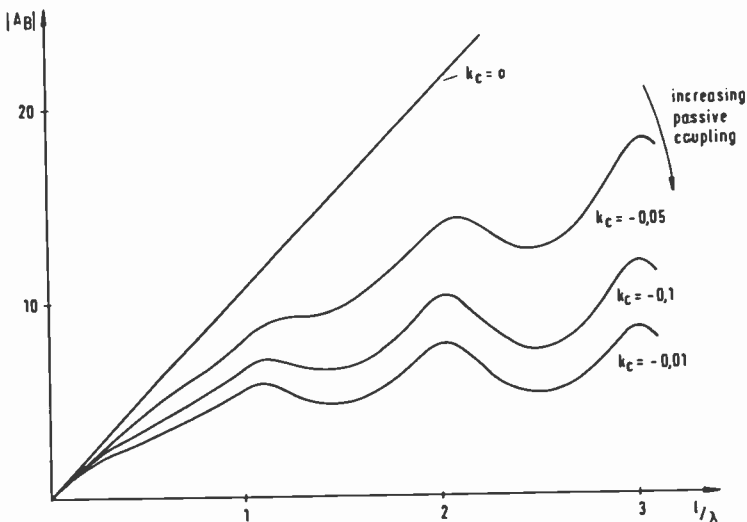tions introduced by impedances Z_1 and Z_2.

Fig. 2—The effective transmission gain of actively and passively coupled
lines as a function of the chosen line length and with passive
coupling factor k_c as parameter. Termination of the lines is by
characteristic impedances.

$$Z_1 = \sqrt{L'_1/(C'_1 + C'_m)}$$
$$Z_2 = \sqrt{L'_2/(C'_2 + C'_m)}.$$

Our results are obtained by solving these equations for coupled lines as outlined in Appendix 1. Fig. 2 shows first the signal transfer for passive completely decoupled lines, where signal transfer occurs only via the transistors. As soon as the lines are placed close to each other, however, passive coupling takes place. A modification of the intended signal transfer occurs that is periodic with l and causes a saturation of signal transfer for line lengths of several wavelengths. We can clearly see, therefore, when a distortion of the intended signal takes place, i.e., when a departure from the straight line appears.

The periodic behavior of Fig. 2 is caused by the appearance of odd- and even-mode features, as is well known for directional couplers. Each of these modes have a different characteristic impedance that is different from $\sqrt{L'_1/(C'_1 + C'_m)}$ and $\sqrt{L'_2/(C'_2 + C'_m)}$. These modes are therefore no longer matched by Z_1 and Z_2, but are partly reflected, causing a standing-wave behaviour.

It is now interesting to give Z_1 and Z_2 values different from $\sqrt{L'_1/(C'_1 + C'_m)}$ and $\sqrt{L'_2/(C'_2 + C'_m)}$, respectively. For example, Fig. 3 shows the signal transfer if the output of line 1 and the input
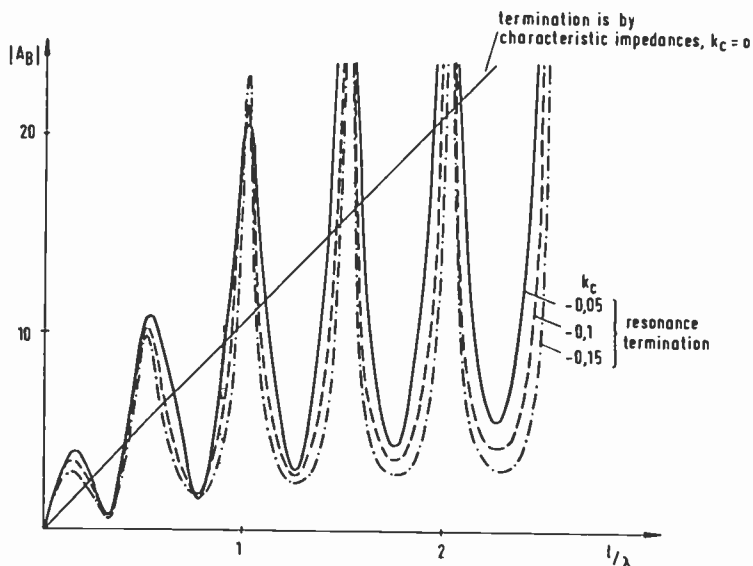

Fig. 3—The effective transmission gain of actively and passively coupled lines as a function of the chosen line length and with passive coupling factor k_c as a parameter. Resonance termination.

of line 2 are open circuits. Here one can see that severe departures from the straight line appear even for very short line lengths. This demonstrates that cross-talk can be enhanced significantly for strongly reflecting features along the transmission lines. Because of the high reflections, the transmission characteristics in this case are nearly independent of an increase in passive coupling.

3. Experimental modelling

A model of the actively and passively coupled closely spaced lines was built, operating at the frequency range 5 to 15 MHz. The dimensions of the various model elements are chosen such that the results can be applied directly to the microwave range of 5 to 15 GHz. The lines are simulated by inductors and variable capacitors and are balanced to give an equal phase velocity, since this has to be assumed for identical passive conductors on monolithic ICs. Dual-gate FETs inserted along the periodic sections exhibit the advantage that their transconductance can be adjusted by the bias voltage of the second gate. Therefore, the bias deviations of the transistors can be equalized. The mutual coupling of the inductors and the coupling capacitors model the electromagnetic field coupling. Ten sections contain the complete model; thus the effect of distributed parameters occurs. Therefore, the results of the model can be transformed to the microwave range without difficulty.

The measured transmission gain $|A_B|$ as a function of the chosen electrode length l shows good agreement with the curves presented in Fig. 2 and 3. For a length $l = 0.15 \lambda$, Figure 4 shows the fre-
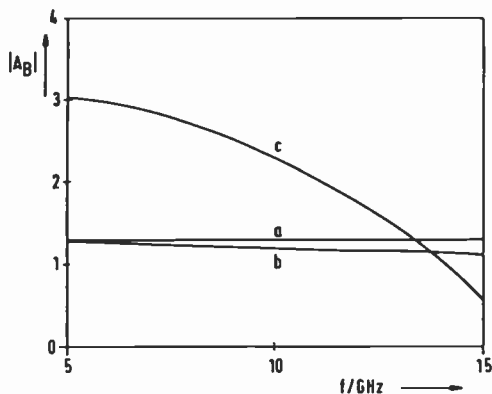

Fig. 4—Measured frequency characteristic of the transmission gain: (a) $k_c = 0$, termination is by characteristic impedances; (b) $k_c = -0.15$, termination is by characteristic impedances; and (c) $k_c = -0.15$, resonance termination.

quency characteristic of $|A_B|$. This is the length at which the first maximum of the transmission gain occurs for the case of a resonance termination. In the passively uncoupled case ($k_c = 0$, curve a in Fig. 4), no limitation in the operating bandwidth is measured, provided the ends of the structure are loaded by the characteristic impedances of the lines. If we consider passive field coupling, an attenuation towards higher frequencies is found (curve b in Fig. 4). On the other hand, for an open-circuit termination of the free electrode ends, great resonance effects take place that one can use for relatively narrow-bandwidth high amplification (curve c). This measured mutual interaction between closely-spaced lines justifies the theoretical evaluation method outlined in Sec. 2.

4. Aspects of Improved Modelling of Monolithically Integrated Transistors

For some applications of high-speed ICs, it is necessary to develop an improved high-frequency description of the inserted transistors, particularly for an analysis such as that outlined in Sec. 2. For microwave frequencies in particular, which often require a very careful design effort, a wave-theoretical derivation of the transistor properties has to be considered.

A wave theoretical analysis of signal propagation along MESFET electrodes in the direction transverse to electron drift has recently been reported[1]. The analysis is based on a passive FET model homogeneous in the direction of wave propagation. This assumption is justified for the short FET dimensions of logic gates of around 50 μm, since the transistor dimensions in the drift direction are only of the order of a few μm. Therefore, fringing fields at the electrode ends only become significant below dimensions of around 10 μm.

The wave analysis is therefore reduced to a two-dimensional one for the cross-sectional plane, which is divided into several homogeneous areas. The electric and magnetic fields in each area are synthesized by infinite sums of their eigenfunctions with unknown coefficients. Satisfying the boundary and continuity conditions at the boundaries of these areas then gives the complex propagation constant $\alpha + j\beta$. Additionally, the wave impedances can be found.

Figure 5 shows the propagation characteristic α and β as a function of frequency for two wave modes, defined as gate and drain types, respectively. While the drain mode shows a normal guided-wave characteristic, the gate type in part exhibits slow-wave behavior.[3] The equivalent circuit presented in Figure 6 gives an almost identical α and β behaviour as this wave theory, so that it can be taken to be realistic. If we assume open-ended electrodes of
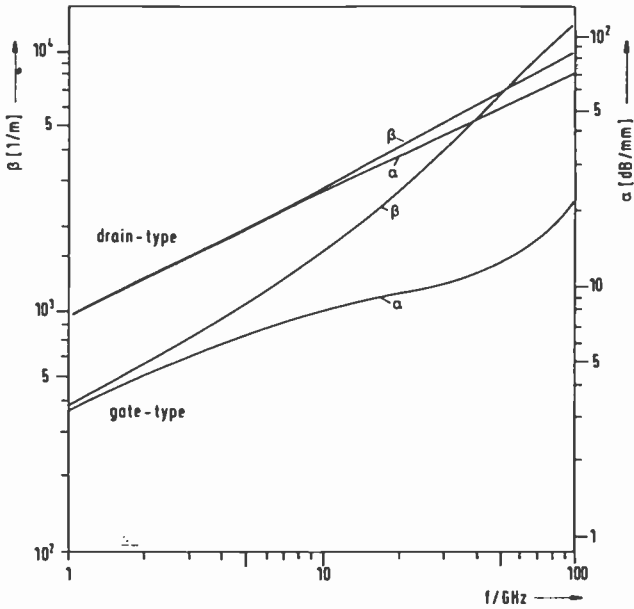
Fig. 5—The propagation constants $\alpha + j\beta$ of the two modes of a MESFET as a function of frequency (gate width is 1 μm and carrier density $n_D = 1.6 \times 10^{17}$)

length l transverse to electron drift, the total equivalent circuit of such FETs can thus be taken to be the same as Fig. 5, except that the component values have to be multiplied by l. This gives a circuit representing the inner transistor. A comparison with commonly employed FET models shows that some differences exist.[4,5] It is suggested here that these might need to be included in any improved
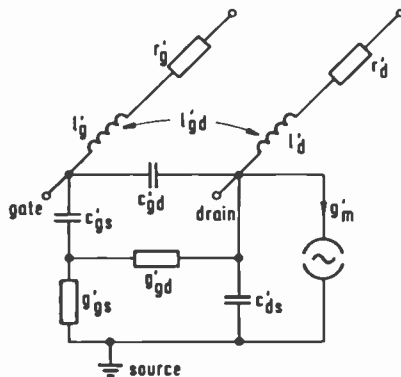
Fig. 6—Equivalent line circuit of the inner FET.

models used for the computer-aided design (CAD) of ICs. Similarly if one uses this circuit in the model of closely spaced lines outlined in Sec. 2, one has a more accurate description of the microwave properties of high speed ICs, while the method of calculation does not change.

Conclusions

The properties of closely-spaced lines on high-speed monolithic ICs operating at microwave frequencies must be considered to obtain reliable design results. In CAD, it is advantegeous to evaluate these problems with the coupled-mode theory, including active and passive coupling between the semiconductor electrodes, as is outlined in the Appendix. Termination conditions and other electrode inhomogenities are relatively easily taken into account by introducing qualified reflection coefficients. An important result of the inclusion of microwave phenomena is that a matched termination of the coupled electrodes is not possible. Only one of the two modes that appear can be matched. Therefore, the wavy nature of the signal transmission of such a device grows with increasing crosstalk. This must be considered for pulse transmission in digital ICs.

Also interesting for analog devices is that one can gain high transmission values in association with a systematic "mistermination." In this case, the electrode length can be selected by the evaluation method presented.

For an improved description of the operation of high-speed ICs at high frequencies, one has to include the parasitics of the transistors used. A field-theoretical analysis studying the waves along MESFETs shows the propagation characteristics. For CAD, an equivalent circuit of the transistor is presented that satisfactorily approximates this wave propagation behaviour.

Acknowledgements

Appendix

The equivalent circuit outlined in Fig. 1 is a simulation of crosstalk between closely spaced lines due to active coupling caused, for example, by many logic gates and passive coupling caused by closely spaced conductors. It is advantageous for such a microwave problem

to describe these circuits by distributed equivalent parameters, where the elements of the line structure of length l have to be defined per length. Figure 7 shows an equivalent circuit with distributed parameters (symbols with primes) for an infinitesimal length dz.

The voltage-current differential equations that describe the model of Fig. 7 are

$$
\begin{aligned}
dU_1/dz + Z'_1 I_1 + Z'_m I_2 &= 0 \\
dI_1/dz + Y'_1 U_1 + Y'_m U_2 &= 0 \\
dU_2/dz + Z'_2 I_2 + Z'_m I_1 &= 0 \\
dI_2/dz + Y'_2 U_2 + (Y'_m + g'_m) U_1 &= 0
\end{aligned}
\tag{1}
$$

where

$$
\begin{aligned}
Z'_1 &= j\omega L'_1;\ Z'_2 = j\omega L'_2;\ Z'_m = j\omega L'_m \\
Y'_1 &= j\omega(C'_1 + C'_m);\ Y'_2 = j\omega(C'_2 + C'_m);\ Y'_m = -j\omega C'_m
\end{aligned}
\tag{2}
$$

In the following derivation, lines where gates are connected are referred to as gate lines and lines where drains are connected as drain lines. In the microwave case it is convenient to use wave-flow concepts to reduce the description of such lines to fundamental microwave phenomena, such as propagation, reflection, mutual coupling, etc. Therefore, we introduce the transformations

$$
U_1 = \sqrt{Z_g}\,(g_+ + g_-);\ U_2 = \sqrt{Z_d}\,(d_+ + d_-)
$$
$$
I_1 = \frac{1}{\sqrt{Z_g}}(g_+ - g_-);\ I_2 = \frac{1}{\sqrt{Z_d}}(d_+ - d_-)
\tag{3}
$$
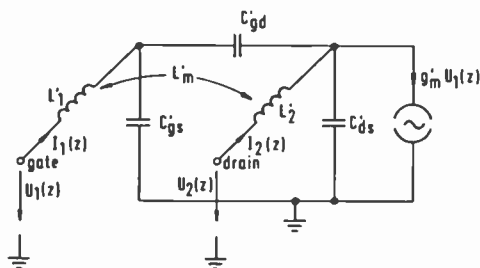
Fig. 7—Equivalent line circuit of infinitesimal length dz.

The differential equations for the waves g_+ and g_- along the gate line and d_+ and d_- on the drain line are

$$
\begin{bmatrix} \dfrac{dg_+}{dz} \\[2mm] \dfrac{dg_-}{dz} \\[2mm] \dfrac{dd_+}{dz} \\[2mm] \dfrac{dd_-}{dz} \end{bmatrix}
= j\sqrt{\beta_g \beta_g}
\begin{bmatrix}
-\sqrt{\dfrac{\beta_g}{\beta_d}} & 0 & -\dfrac{k_1 + k_c}{2} & \dfrac{k_1 - k_c}{2} \\[3mm]
0 & \sqrt{\dfrac{\beta_g}{\beta_d}} & -\dfrac{k_1 - k_c}{2} & \dfrac{k_1 + k_c}{2} \\[3mm]
-\dfrac{k_1 + k_{cm}}{2} & \dfrac{k_1 - k_{cm}}{2} & -\sqrt{\dfrac{\beta_d}{\beta_g}} & 0 \\[3mm]
-\dfrac{k_1 - k_{cm}}{2} & \dfrac{k_1 + k_{cm}}{2} & 0 & \sqrt{\dfrac{\beta_d}{\beta_g}}
\end{bmatrix}
\begin{bmatrix} g_+ \\[2mm] g_- \\[2mm] d_+ \\[2mm] d_- \end{bmatrix}
$$

[4]

where

$Z_g = \sqrt{Z_1'}/\sqrt{Y_1'}$ is the characteristic impedance of the gate-line for $U_2(z) = 0$.

$Z_d = \sqrt{Z_2'}/\sqrt{Y_2'}$ is the characteristic impedance of the drain-line for $U_1(z) = 0$.

$\beta_g = -j\sqrt{Z_1'Y_1'}$ is the phase constant of the passive gate-line for $U_2(z) = 0$.

$\beta_d = -j\sqrt{Z_2'Y_2'}$ is the phase constant of the passive drain-line for $U_1(z) = 0$.

$k_1 = Z_m'/\sqrt{Z_1'Z_2'}$ is the inductive coupling factor of the arrangement.

$k_c = Y_m'/\sqrt{Y_1'Y_2'}$ is the capacitive coupling factor of the arrangement.

$k_{cm} = (Y_m' + g_m')/\sqrt{Y_1'Y_2'} = k_c(1+jS)$ is the active coupling factor.

Because of the contradirectional passive coupling between "natural lines,"[6] we have to introduce $k_1 = -k_c$. Similar passive lines, as one has to assume in monolithic integrated networks, are taken into account by setting $\beta_g = \beta_d = \beta_0$.

Using these notations, the solution of Eq. (4) is

$$
\begin{bmatrix} g_+(z) \\[2mm] g_-(z) \\[2mm] d_+(z) \\[2mm] d_-(z) \end{bmatrix}
= c_1
\begin{bmatrix} 1 \\[2mm] -1 \\[2mm] (1 + \gamma_u/j\beta_0)/k_c \\[2mm] -(1 - \gamma_u/j\beta_0)/k_c \end{bmatrix} e^{-\gamma_u z}
+ c_2
\begin{bmatrix} 1 \\[2mm] -1 \\[2mm] (1 - \gamma_u/j\beta_0)/k_c \\[2mm] -(1 + \gamma_u/j\beta_0)/k_c \end{bmatrix} e^{\gamma_u z} +
$$

$$+ c_3 \begin{bmatrix} 1 \\ 1 \\ -(1 + \gamma_a/j\beta_0)/k_c \\ -(1 - \gamma_a/j\beta_0)/k_c \end{bmatrix} e^{-\gamma_a z} + c_4 \begin{bmatrix} 1 \\ 1 \\ -(1 - \gamma_a/j\beta_0)/k_c \\ -(1 + \gamma_a/j\beta_0)/k_c \end{bmatrix} e^{\gamma_a z}$$

[5]

with the propagation constants

$$\gamma_u = j\beta_0 \sqrt{1 - k^2_c}$$

$$\gamma_a = j\beta_0 \sqrt{1 - k^2_c \, 1(1 + jS)}.$$

[6]

The following results are obtained. Two mutually independent waves propagate along each line. They are superpositions of forward and backward parts of the two modes outlined in Eq. [6]. Because of the existance of the two modes with different characteristic impedances, an ideal termination is impossible. Only one mode can be matched with a given termination impedance. In the assumed lossless structure, γ_u is the propagation constant of a continuous mode and γ_a that of an attenuated mode.

Eqs. [5] are the result of a description of coupling between the lines within the approximation of TEM operation. The wave reflections at inhomogeneities of the chip (load resistances, line branches, line transitions, etc.) enable one then to fix the integration constants c_i. One can take them into account by reflection factors r_{gin}, r_{gout} (which refer to the gate-line-impedance Z_g) and r_{din}, r_{dout} (which refer to the gate-line-impedance Z_d).

For example if we feed the gate line at one of its ends, denoted by $z = 0$, by a signal generator with the open circuit voltage U_0, the boundary value problem to determine the constants c_i is

$$\begin{pmatrix} g_+(0) \\ g_-(l) \\ d_+(0) \\ d_-(l) \end{pmatrix} = \begin{pmatrix} G_+ + r_{gin} \ g_-(0) \\ r_{gout} \ g_+(l) \\ r_{din} \ d_-(0) \\ r_{dout} \ d_+(l) \end{pmatrix}$$

[7]

With the gate-line fed at $z = 0$, we obtain

$$G_+ = \frac{U_0}{2\sqrt{Z_g}} (1 - r_{gin}).$$

[8]

The transmission gain $|A_B|$ is defined as

$$|A_B| = \left(\frac{power\ output}{max.\ available\ power\ at\ input} \right)^{1/2}.$$

For example, if one feeds the gate line as shown above and takes the signal output at the opposite end of the drain line ($z = l$), one obtains

$$|A_B| = \left| \frac{d_+(l)}{G_+} \right| \ [(1 - |r_{g_{in}}|^2)\ (1 - |r_{d_{out}}|^2)]^{1/2}. \tag{9}$$

References:

[1] W. Heinrich and H. L. Hartnagel, "Wave-Theoretical Analysis of Wave Propagation on FET Electrodes Including Electrode and Semiconductor Losses," submitted for publication to *IEEE Trans MTT*, 1983.

[2] K.-H. Kretschmer, W. Heinrich, and H. L. Hartnagel, "Active and Passive Coupling Between Electrodes on Semiconductor Surfaces," *AEÜ*, **37,** p. 229 (1983).

[3] D. Jäger, "Slow-Wave-Propagation Along Variable Schottky-Contact Microstrip Line," *IEEE Trans. MTT*, **24,** 566 (1976).

[4] R. S. Pengelly, *Microwave Field-Effect Transistors—Theory, Design and Applications,* Research Studies Press, 1982, Chichester/New York/Brisbane/Toronto/Singapore (Fig. 2.5 on p. 23).

[5] H. Beneking, *Feldeffekttransistoren,* Springer-Verlag, 1973, Berlin/Heidelberg/New York (Fig. 79 on p. 179).

[6] P. Grivet, *Microwave Circuits and Amplifiers,* Academic Press, 1976, London/N.Y./San Francisco (pp. 623–738).

A Cooled Low-Noise GaAs FET Amplifier*

Robert E. Askew
RCA Laboratories, Princeton, NJ 08540

Abstract—This paper describes a study to determine the feasibility of replacing a 14 to 14.5 GHz parametric amplifier with a cooled GaAs FET low-noise amplifier (LNA). The LNA was designed using an automatic network analyzer and computer-aided-design techniques. The objective of 2.1-dB noise figure and 13-dB gain were achieved when the LNA was cooled to −60C. Some additional effort will be required to improve the performance of the cooler. The study showed that it is feasible to replace a parametric amplifier with a cooled LNA in satellite communications system.

Introduction

In spaceborne communications transponders, the uplink (ground to spacecraft) signal requires amplification before it can be down-converted to the downlink (spacecraft to ground) frequency. It is important that the noise figure of the front-end (up-link frequency) amplifier be as low as possible in order to maximize the sensitivity of the receiver, and for that reason parametric amplifiers are used in the systems designed for operation in the 14 to 14.5 GHz band. However, parametric amplifiers are complex and expensive components, and it is generally difficult to maintain their frequency stability.

This paper describes a study to determine the feasibility of replacing the 14 to 14.5 GHz parametric amplifier with a cooled GaAs FET low-noise amplifier (LNA). The study was based on a previously described similar program for a lower frequency band.[1] The initial specifications established for this LNA were

---

- Frequency—14.0 to 14.5 GHz
- Noise Figure—2.1 dB max.
- Gain—13 dB
- Gain Flatness—±0.3 dB

Design Approach

The objective was to develop an amplifier that does not have the parametric amplifier's basic instability and bandwidth problems and that could be competitive on the basis of low noise figure and simplicity. At the inception of the program, there were no low-noise transistors available that could achieve the required performance at satellite ambient temperatures. Our approach was to design an LNA and cool it using a thermoelectric (Peltier effect) cooler to a temperature that would reduce it's noise figure to the specified value. A block diagram of the proposed LNA is shown in Fig. 1.

The initial assumption was that a two-stage amplifier would meet gain requirements, and any available transistor with a reasonably low noise figure at room temperature could be cooled to meet the requirements of this program. If too low a temperature were required, however, there would be a major problem with the power needed for cooling. The goal therefore was to get the best available low-noise device and cool it to a temperature at which it would just meet the specifications, thus minimizing power consumption.

A search for the best available low-noise transistor resulted in the data shown in Table 1, which is based on information from manufacturers' data sheets. From the data shown under "Noise
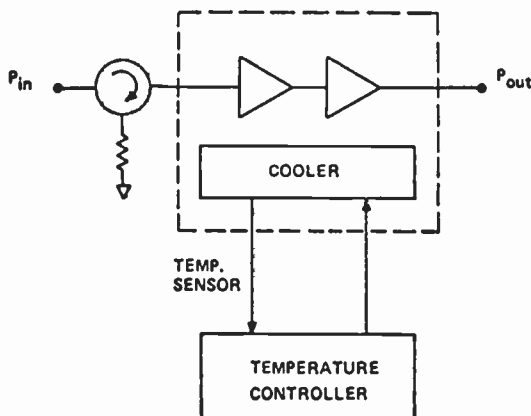
Fig. 1—Proposed Peltier-cooled low-noise amplifier.

Table 1—Comparison of Low-Noise Transistors (Based on Manufacturer's Data Sheets, Dec. 1981)

Manufacturer	Type No.	Noise Figure F (dB)				Assoc. Gain G (B)				Noise Measure M (dB)*			
		4 GHz	8 GHz	12 GHz	18 GHz	4 GHz	8 GHz	12 GHz	18 GHz	4 GHz	8 GHz	12 GHz	18 GHz
Alpha	ALF-3000(C)	0.9	1.5	2.1		13.0	11.0	8.5		0.94	1.61	2.36	
	ALF-3000(P)	0.9	1.5	2.1		13.0	10.5	8.0		0.94	1.62	2.40	
Avantek	AT-8040(P)		1.7+	2.4			13.0+	9.0			1.77+	2.67	
	AT-8041(C)		1.7+	2.0	2.8		13.0+	10.0	7.0		1.77+	2.17	3.29
	AT-8060(P)		1.9+	2.8			11.0+	8.0			2.03+	3.11	
	AT-8061(C)		1.9+	2.5	3.3		11.0+	9.0	5.0		2.03+	2.76	4.26
Dexcel	DXL-2503A(C)		1.9	2.8	4.0		10.0	8.0	5.5		2.07	3.17	4.92
Mitsubishi	MGF-1400(P)	2.0	3.2	4.5		9.0	7	6.0		2.22	3.73	5.35	
	MGF-1402(P)	1.1	2.0	3.0		13.0	10.0	8.0		1.15	2.17	3.39	
	MGF-1403(P)	0.8	1.3	1.8	2.8	14.0	12.0	10.5	7.0	0.83	1.38	1.94	3.29
	MGF-1412(P)	0.8				13.0				0.84			
NEC	NE13700(C)	0.8	1.2	1.9	2.5	14.0	11.0	9.5	7.5	0.83	1.29	2.09	2.89
	NE13783(P)	0.8	1.2	1.9		14.0	11.0	9.0		0.83	1.29	2.12	
	NE13783S(P)	0.8	1.2	1.6		14.0	11.0	9.5		0.83	1.29	1.76	
	NE38800(C)	1.2	2.0	2.8	4.0	13.5	11.5	8.5	6.0	1.25	2.12	3.13	4.80
	NE38883(P)	1.2	2.3	3.2		13.0	11.0	7.5		1.25	2.45	3.66	
	NE70000(C)	1.0	1.5	2.3		13.0	11.0	9.0		1.05	1.61	2.55	
	NE70083(P)	1.0	1.5	2.3		13.0	11.0	9.0		1.05	1.61	2.55	
Plessey	GAT-6/P100(C)	1.0	1.5	2.2	3.5	15.0	11.5	9.5	7.0	1.03	1.60	2.41	4.06
	GAT-6/P104(P)	1.0	2.0	2.5		14.0	9.5	8.5		1.04	2.20	2.80	

(C) indicates chip, (P) indicates packaged.
* $M = 10 \log \{1 + (F - 1)/[1 - (1/G)]\}$.

Measure"* in Table 1, it is obvious that the best low-noise device at 12 GHz was the Nippon Electric Company's (NEC) NE13783S. The "S" suffix indicates that this part was selected by the manufacturer for low-noise performance at 12 GHz. As can be seen, the noise measure for the "S" selection was better than the standard NE13783 by 0.36 dB.

The decision to use either a packaged transistor or a chip device was based more on thermal requirements than rf performance, since package parasitics have a minimal effect on noise performance. The thermal resistance, channel-to-ambient, of the packaged transistor was 450°C per watt compared to 190°C per watt for the chip device. Calculations had shown that cooling the packaged transistor required 70% more power than the chip transistor to maintain a transistor channel temperature of −50°C. Since cooling power is limited, the more power-efficient approach had to be used, and the chip transistor was selected.

The chip transistor is mounted on a small, gold-plated copper carrier which greatly facilitates handling, testing, and interchangability of these small chips from one circuit to another. A sketch of this carrier is shown in Fig. 2.†

A computer program, "LNA", was written to aid in determining design trade-offs in multi-stage, cooled LNA's. This program, when
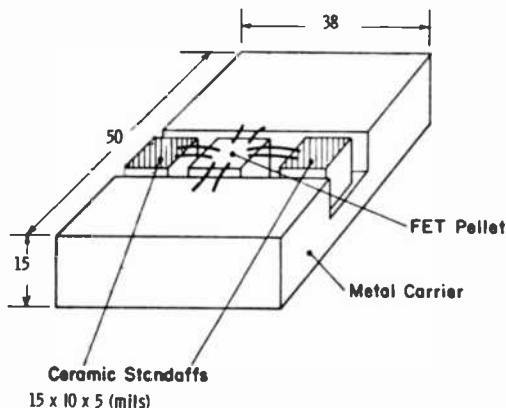
Fig. 2—Carrier used to hold chip transistor during testing.

---

* Noise measure is the noise figure one would obtain from an infinite cascade of identical stages. It is given by $M = 10 \log \{1 + (F − 1)/[1 − (1/G)]\}$ where F = noise figure and G = gain (both in ratios).
† This carrier was developed by F. N. Sechi of RCA Laboratories.

```
:LNA
FOR 'NEXT' LIST TYPE '1', '2' TO START PROGRAM
NEXT = ?1
NEXT =
0...STOP
1...NEXT LIST
2...START OVER
3...CHG INPUT LOSS
4...CHG RM TEMP PERF OF IN FETs
5...CHG # OF AMP STAGES
6...HOW MANY COOLED?
7...WHAT    TEMP?
8...CHG RM TEMP PERF OF UNCOOLED FETs
9...CHG AMBIENT TEMP
10..CHG POST AMP NF
11..CHG INTER-  AMP LOSS.(NOT YET)
NEXT = ?2
ANY INPUT CIRCUIT LOSSES?(Y/N) Y
HOW MUCH INPUT CIRCUIT LOSS?(DB) .2
ROOM TEMP PERF.OF LN(COOLED) STAGES,NF,G (DB) 2.5,7.2
HOW MANY AMP STAGES(LN+HT G=?)? 2
HOW MANY LOW NOISE (COOLED)? 2
TO WHAT TEMP(C)? -60
POST AMP OR MIXER NOISE FIGURE (DB) = 4.5


NOISE FIGURE =    2.11 dB
NOISE TEMPERATURE=   181.3 K
TOTAL GAIN =   16.75 dB
COOLED TO:  -60.0 C
```

Fig. 3—Sample printout from computer program "LNA".

given the noise figure and gain of a transistor at room temperature, will calculate the noise figure, noise temperature, and gain of an amplifier chain with any number of stages cooled to a given temperature. A sample printout from "LNA" is shown in Fig. 3 where the user inputs are underlined. The example shows an amplifier chain with the following characteristics:

Input Circuit Loss = 0.2 dB (input isolator)
Transistor Specifications ($+25°C$) = NF = 2.5 dB, Gain = 7.2 dB
Amplifier stages (LN + Hi Gain) = 2
Number of LN, cooled = 2
Cooled to $-60°C$
Post amp/mixer = NF = 4.5 dB

The computer printout shows that the noise figure of this amplifier will be 2.11 dB with a gain of 16.75 dB when cooled to $-60°C$.

One of the basic equations of the "LNA" program gives the change in noise temperature as a function of a change in device temperature; another is the classic cascaded-amplifier noise-figure equation. Given the room-temperature noise figure F (as a ratio), the effective noise temperature, T_e, in degrees Kelvin is

$$T_e = 290 (F - 1).$$

The effective noise temperature at any temperature is

$$T_{e2} = T_{e1}\left(\frac{T_2}{290}\right)^{1.5}$$

where T_2 is the new temperature and T_{e1} is the effective noise temperature at room ambient.

The noise figure of four amplifier stages followed by a post-amplifier, or a mixer, with a noise figure F_p is

$$F = F_c + \frac{F_c - 1}{G_c} + \frac{F_u - 1}{G_c^2} + \frac{F_u - 1}{G_c^2 G_u} + \frac{F_p - 1}{G_c^2 G_u^2},$$

where the subscript c refers to the cooled stages, the subscript u refers to the uncooled stages, F is noise figure, and G is gain. The factors of this equation were modified by coefficients determined by the number of required cooled and uncooled stages. For example, in a two-stage LNA where both stages are cooled, the third and fourth terms are zero and G_u equals one.

The chip transistor, in its test fixture was characterized on a computer controlled network analyzer using a relatively new calibration procedure.[2] This procedure, TSD (Thru-Short-Delay), did not require high quality components for good calibration results and it provides the S-parameters of the device under test (DUT) by automatic de-embedding techniques. TSD required three test fixtures, all of which have connector interfaces that are identical to the ones used on the transistor test fixture. The "thru" fixture has a transmission line equal to the total length of the input and output transmission lines on the transistor fixture. The "short" has lines that are shorted at a position equal to the location of the transistor under test. The "delay" is slightly longer than the "thru" but not an integral multiple of a half wavelength in the frequency band of interest.

The transistor data obtained as a result of this procedure were used to plot gain and stability circles on a Smith Chart (Fig. 4). While this presentation gave the data required to design matching networks for achieving good broadband gain, additional information was required for low-noise design. This additional information was arrived at with the test setup shown in Fig. 5. The key component of this test set is the Hewlett-Packard, Model 8970A, noise-figure meter. This instrument provides outputs for an oscilloscope display of noise figure and gain in real time that greatly facilitates the tuning adjustments of the device under test.

After adjusting the output tuner for maximum gain, the input
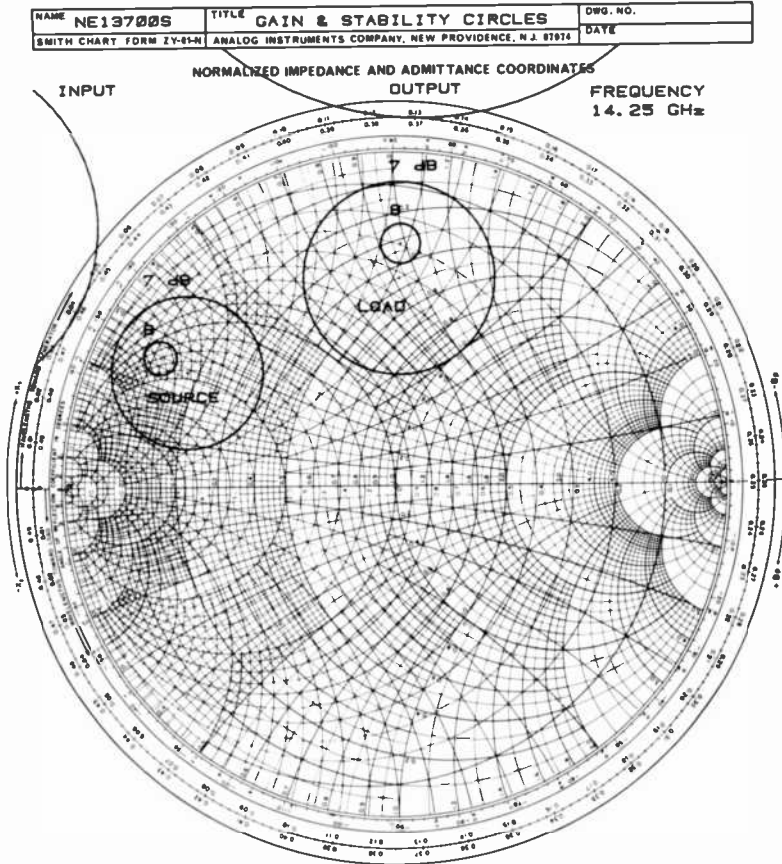
Fig. 4—Gain and stability data on NE13700S obtained using TSD (Thru-Short-Delay) procedure.

tuner is adjusted for noise-figure values near the minimum value, and the tuner probe position and depth are recorded. This procedure was followed for at least seven noise-figure points at three frequencies in the band. The impedance of the tuners was measured on the automatic network analyzer at each of the abovementioned points, and these points were translated to impedance at the transistor carrier. The resulting reflection coefficient of the source (input) impedance and noise figure were put into a computer program[3] that calculates from four data points at each frequency the noise parameters: noise resistance, minimum noise figure, and optimum source reflection coefficient at minimum noise figure.

The program solves the noise figure equation[4]
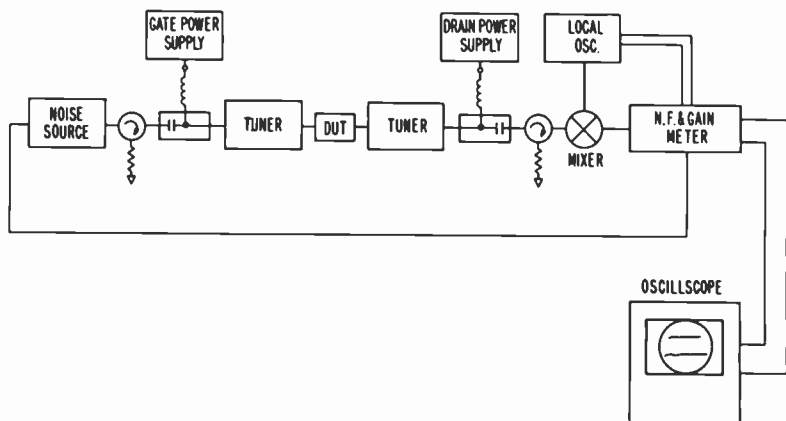
Fig. 5—Test setup used for low-noise design.

$$F = F_{min} + \frac{R_n}{G_s} |Y_s - Y_{opt}|^2.$$

Here $Y_{opt} = G_{opt} + jB_{opt}$ is the source admittance that gives F_{min} and $Y_s = G_s + jB_s$ is the source admittance.

Points that showed the range of input impedances that tune the transistor for a given noise figure were added to the previously mentioned Smith chart. Fig. 6 shows the Smith chart plot of constant-noise-figure circles for the NE13700S. From this plot, the best compromise between gain and noise figure was determined and, therefore, the matching network that results in the lowest input loss while meeting the amplifier bandwidth requirements.

After the initial matching network topology was selected, the design was optimized using the CAD program SUPER-COMPACT. Fig. 7 shows a photograph of the input, interstage, and output matching networks and the transistor carriers, all mounted on the gold-plated Kovar circuit carrier. The size of the circuit carrier is 0.450 × 0.500 inch (1.14 × 1.27 cm).

While the study was in progress, a new low-noise transistor was announced by NEC, the NE67300. This device has an 0.3-μm gate and is designed for low-noise performance up to 26.5 GHz. At 12 GHz the noise measure of the NE67300 is 1.53 dB compared to the NE13700S figure of 1.77 dB.

The S-parameters of the new device are close enough to those of the NE13700S that we used it in the same circuit and obtained slightly improved performance. Fig. 8 shows a Smith chart plot of S_{11} and S_{22} for the NE13700S and the NE67300.
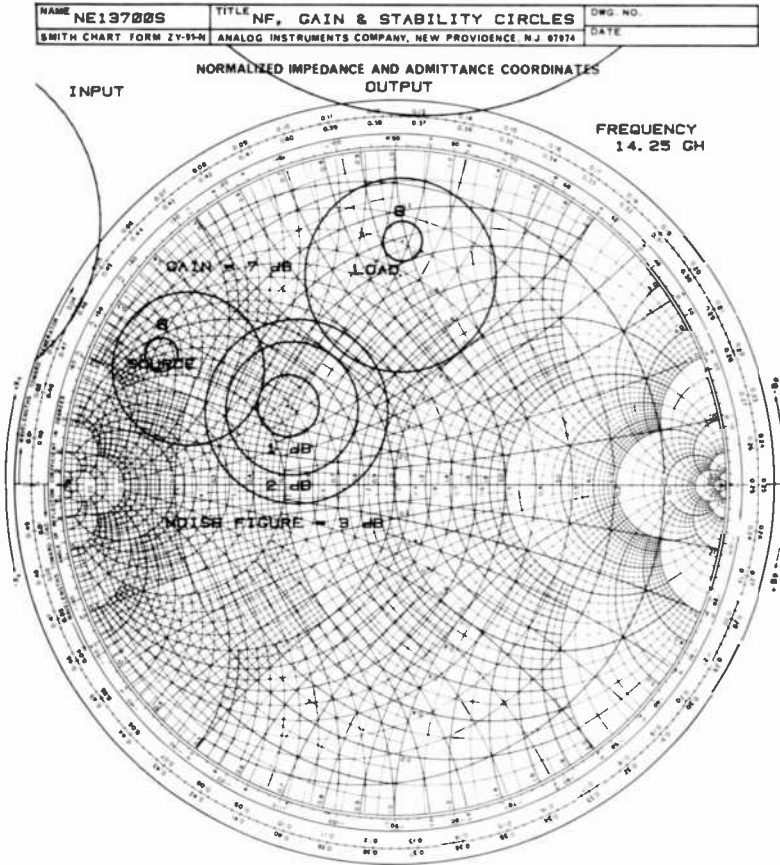
Fig. 6—Smith chart plot of constant-noise-figure circles for NE13700S.

Packaging

The LNA matching networks are soldered to a gold plated Kovar carrier. The carrier contains a copper insert that thermally couples the copper transistor carriers to the cold plate of the cooler. The copper insert reduces the thermal resistance between the transistors and the cooler to about one-twentieth the resistance of the surrounding Kovar. Fig. 9 is a cross-sectional drawing showing the location of the transistors with respect to the cooler.

The final temperature required for the LNA was −60°C. At this temperature, condensation would become a problem during earthbound testing; therefore, some form of hermetic packaging was re-
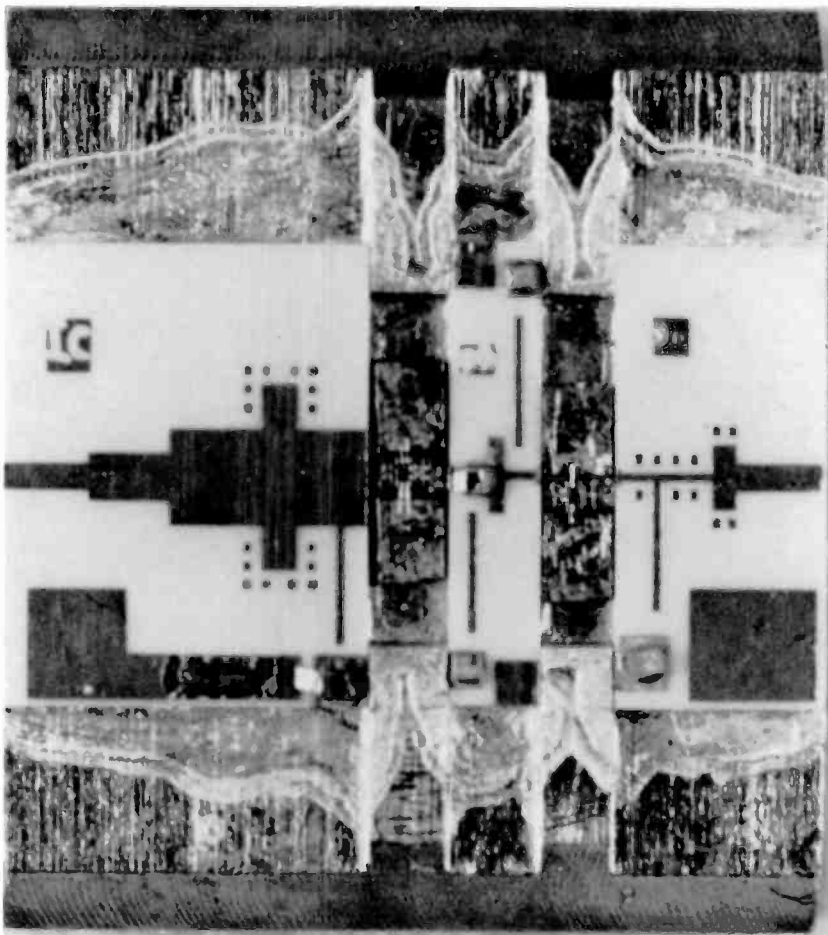
Fig. 7—Input, interstage, and output matching networks mounted on gold-plated Kovar circuit carrier.

quired. More importantly, very good insulation and thermal isolation were required to keep power consumption to a minimum.

The LNA is mounted on the thermoelectric cooler and held in position by pressure contact to avoid any undue mechanical stresses between the Kovar circuit carrier and the cooler's beryllia substrate. The cooler is soldered to a copper heat spreader that forms the bottom of the housing that encloses the amplifier and the cooler. The housing is made of stainless steel as are the input waveguide section and the output coaxial transmission line. Stainless steel was chosen for it's low thermal conductivity.
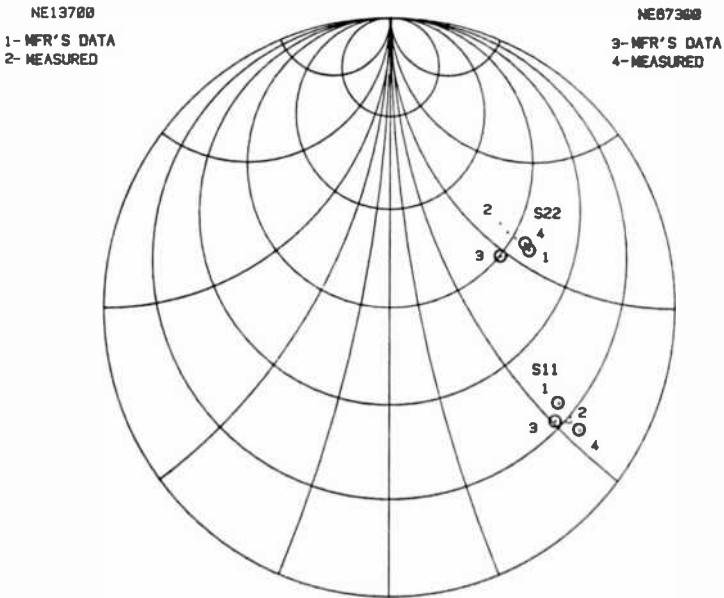
Fig. 8—Smith plot of S_{11} and S_{22} for NE13700 (points 1 and 2) and for NE67300 (points 3 and 4).
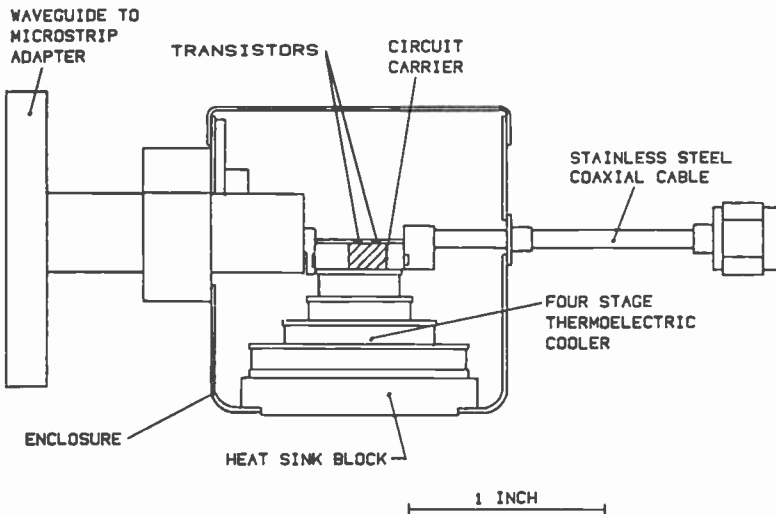
Fig. 9—Cross section of cooled low-noise amplifier.

A mica window was placed at the open end of the waveguide-to-microstrip transition to prevent condensation from forming at the very cold portion of the assembly. Fig. 10 shows the major parts used in the final assembly of the LNA, and Fig. 11 shows the assembled unit on the test fixture. The housing containing the amplifier and cooler are filled with styrofoam insulation. Prior to sealing, the housing was evacuated and back-filled with dry nitrogen.

Fig. 12 is a schematic of the cooler control circuit. It consisted of a resistance bridge that includes a thermistor epoxied into the copper insert in the circuit carrier.

Results

The final data of the cooled LNA is shown in Fig. 13. These results were obtained using external cooling to assist the thermoelectric cooler to reach −60°C. This was required due to the leakage path through the waveguide into the housing and through the housing itself from the copper heatsink at the bottom of the housing. The cooler power required was approximately 13 watts. Recommended methods to improve the cooler performance include placing baffles
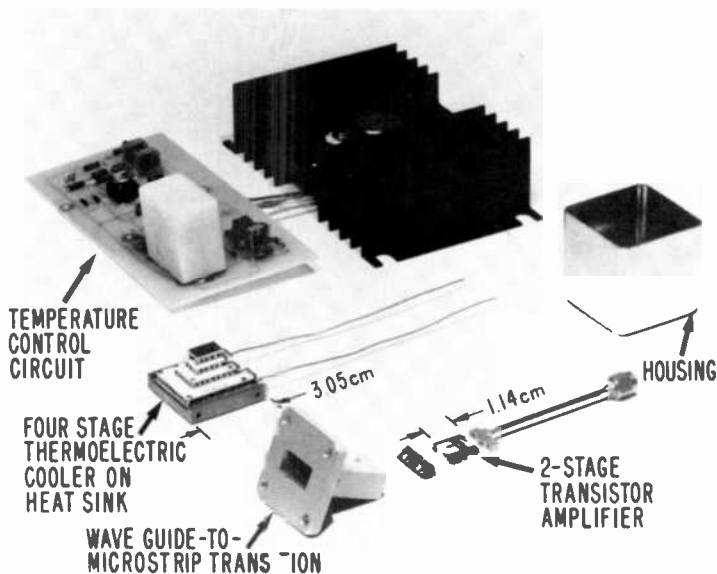
Fig. 10—Major parts of the LNA.
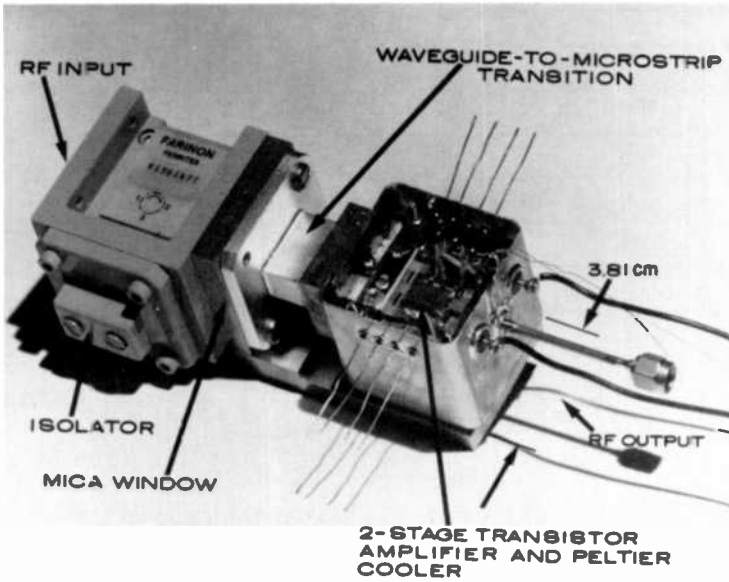
Fig. 11—Assembled LNA on test fixture.

TH = THERMISTOR
R = TBD BY THERMISTOR CHARACTERISTICS
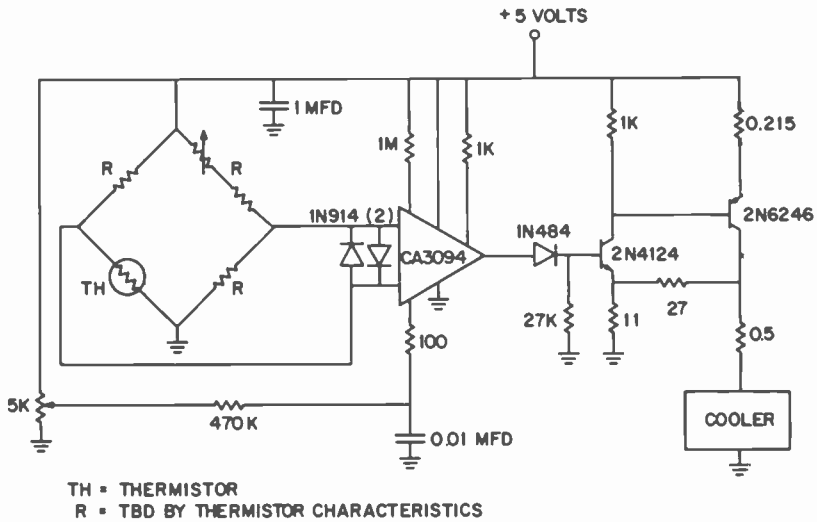
Fig. 12—Cooler control circuit for LNA.
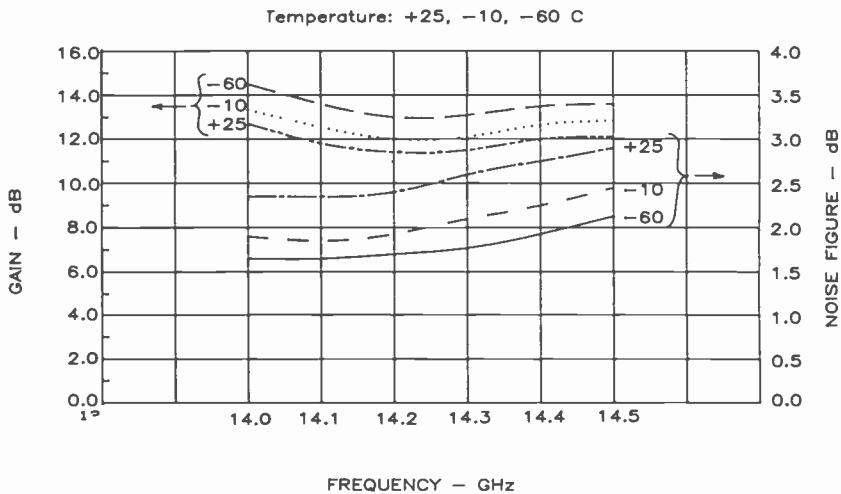
Fig. 13—Gain and noise figure versus frequency for cooled LNA.

at the different stages of the cooler and replacing the stainless steel waveguide section with one of a higher thermal resistance. The data clearly shows, however, that it is feasible to replace a parametric amplifier with a cooled LNA.

Acknowledgments

The author wishes to thank F. Sterzer for his support of this program, H. J. Wolkstein for his guidance and encouragement, H. Goldberg for defining system requirements, and S. P. Grober for his amplifier assembly work.

References:

[1] R. E. Askew and H. J. Wolkstein, "A Low-Noise Peltier-Cooled FET Amplifier," *RCA Rev.*, **42**, p. 661, Dec. 1981.
[2] R. A. Special, "A Generalization of the TSD Network Analyzer Calibration Procedure Covering *n*-Port Scattering Parameter Measurements Affected by Leakage Errors," *IEEE Trans. MTT*, **MTT-25**(12), 1977.
[3] R. L. Camisa, private communication.
[4] R. Q. Lane, "A Microwave Noise and Gain Parameter Test Set," *IEEE Int. Solid-State Circuits Conf.*, pp. 172, 173, 274 (1978).

A Dynamic CAD Technique for Designing Broadband Microwave Amplifiers†

B. S. Yarman*
RCA Laboratories, Princeton, NJ 08540

Abstract—A new "dynamic" CAD procedure for designing microwave am-
plifiers with the simplified real frequency technique is pre-
sented. The new technique takes less computation time and
yields superior amplifier gain performance over the other avail-
able CAD techniques. We demonstrate that the technique is
suitable for designing linear power amplifiers. Application of
the technique is shown by several examples. An X-band power
amplifier was designed and built with the element values ob-
tained using the new procedure. Laboratory measurements ex-
hibit good agreement with the theoretical calculations.

1. Introduction

In previous publications[1,2] a new computer-aided design (CAD) tech-
nique, a "simplified real-frequency" technique for designing broad-
band equalizers or matching networks, was introduced by Yarman
and Carlin. Unlike the analytic and conventional CAD techniques,
the new method utilizes the measured data obtained from the phys-
ical devices to be matched and requires no knowledge of an alge-
braic form of the transfer function or circuit topology. This tech-
nique was also extended to design microwave amplifiers using a
sequential procedure.[2]

In this paper, we present a new dynamic procedure to design
microwave amplifiers; the simplified real-frequency technique has
been successfully incorporated to realize the matching networks.

The next two sections of this paper discuss the simplified real-frequency technique and the sequential design procedure to provide the necessary background to the reader. Then, the new amplifier design procedure is introduced.

The new technique requires less computation time and yields superior amplifier performance over other available CAD techniques[3,4] and the sequential procedure.[2] We demonstrate that the new procedure is suitable for designing linear power amplifiers. Several examples are presented to show the application of the technique. A power amplifier using the Raytheon FET RPX-6036 was designed and built in X-band employing the new technique. Laboratory results are in good agreement with the theoretical predictions.

2. Simplified Real-Frequency Technique

A classical broadband matching problem (see Fig. 1) is to realize a lossless network or equalizer E between the given complex generator and an arbitrary load so that transfer of power from generator to load is maximized over a prescribed frequency band. In the simplified real-frequency technique, lossless, reciprocal E is described in terms of its unit-normalized, bounded-real scattering parameters $\{e_{ij}\}$, $i,j = 1,2$. It can be shown that the scattering parameters of E can be completely determined from the numerator polynomial $h(s)$ of the input reflection coefficient $e_{11}(s) = h/s$.

For the sake of practical simplicity, E is assumed to be a ladder network with transmission zeros at $\omega = \infty$ and/or $\omega = 0$. Then, the scattering parameters $\{e_{ij}\}$ of E are given as

$$e_{11}(s) = \frac{h(s)}{g(s)}$$

$$e_{12}(s) = e_{21}(s) = \mp \frac{s^k}{g(s)} \qquad [1]$$

$$e_{22}(s) = -(-1)\frac{k\ h(-s)}{g(s)}$$
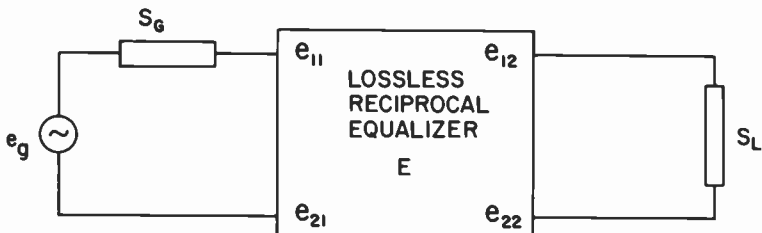
Fig. 1—Classical broadband matching problem.

where $h(s) = h_0 + h_1 s + \ldots + h_n s^n$ is an arbitrary polynomial with real coefficients, $g(s) = g_0 + \ldots + g_n s^n$ is a Hurwitz polynomial which is given in terms of $h(s)$ by the losslessness of E:

$$g(s)\, g(-s) = h(s)\, h(s) + (-1)^k w^{2k} \qquad [2]$$

where, $k \geqslant 0$ is an integer, contributes to the complexity of the matching network together with $n \geqslant 0$ which is the degree of the numerator polynomial $h(s)$.

With Eqs. [1] and [2], the transduced power gain $T(\omega)$ of Fig. 1 can be generated as an implicit function of $h(s)$:

$$T(\omega) = T_g \frac{|e_{21}|^2 |\ell_{21}|^2}{|1 - e_{11}S_G|^2 |1 - \hat{e}_{22}S_L|^2}$$

where $T_g = 1 - |S_G|^2$

$$|\ell_{21}|^2 = 1 - |S_L|^2$$

$$\hat{e}_{22} = e_{22} + \frac{e_{21}^2 S_G}{1 - e_{11} S_G}$$

and $S_G(jw)$ and $S_L(jw)$ are the reflection coefficients of generator and load networks, respectively.

In the simplified real-frequency technique, the polynomial $h(s)$ is chosen as unknown. A numerical nonlinear optimization problem is set up to determine the unknown coefficients h_i, $i = 1$, n of $h(s)$ $= h_0 + h_1 s + \ldots + h_n s^n$ and thereby to optimize the gain over the frequency band. In this process, the complexity of the matching network is chosen in advance by fixing the integers k, $n \geqslant 0$.

Once $h(s)$ is known and $g(s)$ is generated from it by explicit factorization of Eq. [2], $e_{11}(s)$ is generated as a bound-real (BR) realizable function. Then the input impedance $Z_{in} = (1 + e_{11})/(1 - e_{11})$ looking into the equalizer E is realized as a lossless network with resistive termination using the Darlington method. Removal of this resistive termination yields the desired equalizer E.

3. A Sequential Procedure For Designing Microwave Amplifiers[2]

With the simplified real-frequency technique outlined above, a microwave amplifier may be designed using the following sequential technique:

Refer to Fig. 2a. First the input matching network E_F is developed while the back-end of the active device F (possibly an FET) is resistively terminated (1 Ω). At this step the transducer gain $T_1(\omega)$ of $E_F - F$ is optimized. Then moving the resistive termination, output
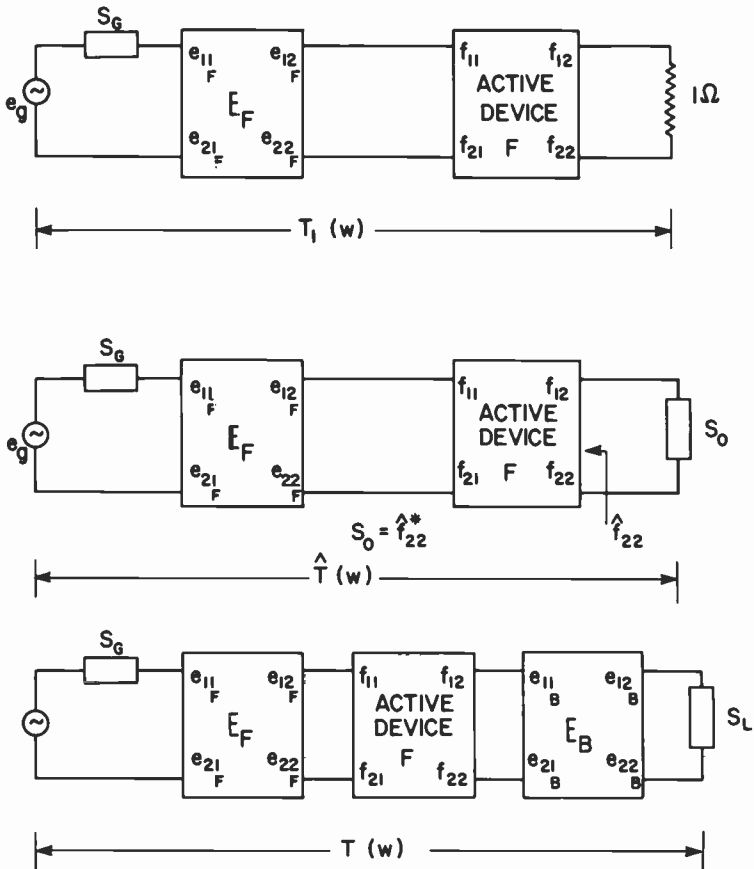
Fig. 2—(a) First step of the sequential amplifier design procedure (development of the front-end matching network E_F). (b) First step of the new dynamic amplifier design procedure. (c) Development of the back-end matching network E_B.

matching network E_B is developed (Fig. 2c). At this step overall gain $T(\omega)$ of the amplifier is optimized. Once E_F and E_B are computed, a final step may be carried out by iterating the above procedure. That is, one recomputes E_F when E_B is in place; then E_B is recomputed with E_F in place to improve $T(\omega)$, etc. It should be noted that this additional step may be costly and convergence is not guaranteed. However, the new "dynamic" design procedure overcomes the disadvantages of the sequential technique. In the new method the final iteration scheme is omitted. Thus, computation time is reduced. Furthermore, resulting amplifiers yield superior gain per-

formances over the other available CAD techniques and the sequential design procedure.

4. A Dynamic CAD Technique For Designing Microwave Amplifiers

The new technique is the improved version of the sequential procedure summarized above; it consists of two steps. As in the sequential technique, in the first step, front-end matching network E_F is developed while the output of the active device F is terminated with perfect match S_0 (Fig. 2b). Clearly, the hypothetical termination S_0 is a function of E_F as well as F and given by

$$S_0 = \hat{f}_{22}{}^* \qquad [4]$$

where * designates the complex conjugate of a complex function,

$$\hat{f}_{22} = f_{22} + \frac{f_{12} f_{21}}{1 - f_{11} \hat{e}_{22F}} \hat{e}_{22F} \qquad [5]$$

and

$$\hat{e}_{22F} = e_{22F} + \frac{e_{21F}^2}{(1 - e_{11F})S_G} S_G \qquad [6]$$

In Eqs. [4] through [6] $F = \{f_{ij}\}$ and $E_F = \{e_{ijF}\}, i,j = 1,2$ denote the real normalized scattering parameters of the active 2-port device F and the front-end equalizer E_F, respectively, and S_G is the real normalized reflection coefficient of the generator network.

At this step the hypothetical gain function $T(\omega)$ which is given as

$$T(\omega) = T_G \frac{|e_{21F}|^2 |f_{21}|^2}{|1 - e_{11F} S_G|^2 |1 - \hat{e}_{22F} f_{11}|^2 \, [1 - |\hat{f}_{22}|^2]} \qquad [7]$$

is optimized.

In the second step, S_0 is removed and the back-end matching network E_B is developed to maximize the actual transducer gain $T(\omega)$:

$$T(\omega) = T_1 \frac{|e_{21B}|^2 |\mathfrak{c}_{21}|^2}{|1 - e_{11B} \hat{f}_{22}|^2 |1 - \hat{e}_{22B} S_L|^2} \qquad [8]$$

where

$$T_1 = T_G \frac{|e_{21F}|^2 |f_{21}|^2}{|1 - e_{11F} S_G|^2 |1 - \hat{e}_{22F} f_{11}|^2} \qquad [9]$$

$$\hat{e}_{22B} = e_{22B} + \frac{e_{21B}^2}{1 - e_{11B}\,\hat{f}_{22}} \qquad [10]$$

$$T_G = 1 - |S_G|^2 \qquad [11]$$

$$|\ell_{21}|^2 = 1 - |S_L|^2 \qquad [12]$$

and $E_B = \{e_{ijB}\}i,j = 1,2$ is the real normalized scattering matrix of the back-end matching network E_B, and $S_L(j\omega)$ is the real normalized reflection coefficient of the load network.

At the end of this step, one wishes to approach $T(\omega)$ which is the gain under perfect match. It is interesting to note that during the design process, the gain taper of the active device is distributed between E_F and E_B in such a way that overall gain and gain flatness of the amplifier are maximized as much as possible.

Furthermore, since the output matching network E_B is constructed to approximate the perfect match $\hat{f}_{22}^* = S_0$, the amount of power delivered to the load is also maximized. Thus, the dynamic procedure presented above is suitable to design power amplifiers, provided the active device is reasonably linear within the dynamic range of the operation.

The gain performance of the resulting amplifier may still be improved as in the sequential technique or by optimizing the element values of the circuit topologies of E_F and E_B which are the results of the simplified real-frequency technique. However, our practical experience showed that there is no significant improvement achieved by further computations. The technique described here can also be extended to design multistage amplifiers developing the matching networks one stage at a time and terminating the output of the active devices with the perfect match in a manner similar to that described in Ref. [2].

5. Numerical Work

Based upon the design procedure described above, an interactive computer program called SEMA has been developed at RCA. The algorithmic structure of SEMA is very similar to that of CARMAN-03 given in Ref. [2]. Basically, SEMA constructs the matching networks, for fixed complexity, to optimize the transducer power gain of the amplifier. The measured FET scattering parameters and generator and load data are externally supplied to the program. In the optimization scheme, an ideal flat form of the gain is approximated using the method of least squares. In general, any interactive non-

linear optimization algorithm can be employed in the program. In this work, it was found that the modified Levenberg Marquard technique, which minimizes the least square error functions, provides satisfactory results.[5] Initialization of the program is very similar to that of CARMAN-03. Therefore we omit the details here. The interested reader should see Refs. [1] and [2]. However, it is useful to point out that for many practical cases, it is sufficient to initialize the unknown coefficients h_i as $+1$ or -1.

6. Design Examples

In this section three design examples are presented to show the application of the new dynamic amplifier design procedure. The first two examples particularly call for wideband designs (6 GHz–16 GHz). In the second example we show the extension of the technique to the design of multistage amplifiers. There, a two-stage amplifer is designed. Finally, the last example shows the suitability of the technique for designing power amplifiers. Comparison with the other available CAD techniques is also included.

Throughout the examples, the flat gain level T_0, which is approximated in the least square sense, is chosen as the minimum of the maximum available gain of the FETs over the passband.

$$T_0 = \min_{\substack{\text{over} \\ \text{passband}}} \left\{ \frac{|f_{21}|^2}{[1 - lf_{11}l^2][1 - lf_{22}l^2]} \right\}$$

Example 1

In this example, we design a single-stage amplifier for 50-Ω terminations using the HP-HFET-2001 device. Inputs to the SEMA program and the performance of the amplifier are summarized as follows:

Generator: $S_G = 0$ ($Z_G = 50\ \Omega$)
Load   : $S_L = 0$ ($Z_L = 50\ \Omega$)
Passband : 6 GHz $\leq f \leq$ 16 GHz

Complexity of the matching networks:

Step 1: E_F (front-end matching network)
      $n = 2, k = 0$
(Two-element low pass ladder)

Step 2: E_B (back-end matching network)

$\qquad n = 3, k = 0$

(Three-element low pass ladder)

Flat gain level to be approximated in the least square sense 7.5 dB.

Scattering parameters: f_{ij} are given in Table 1.[6]

Table 1—Scattering Parameters of HFET-2001 (Hewlett Packard)[6]

Frequency (GHz)	f_{11}		f_{21}		f_{12}		f_{22}	
6	0.88	−65	2	125	0.05	60	0.71	−22
8	0.83	−85	1.81	109	0.06	53	0.68	−30
10	0.79	−101	1.64	95	0.06	51	0.66	−37
12	0.76	−113	1.48	84	0.06	52	0.66	−43
14	0.73	−126	1.39	73	0.06	54	0.64	−48
16	0.71	−141	1.32	61	0.07	55	0.63	−56

Linear Power Bias $V_{DS} = 4.0$ V, $I_{DS} = 50\% I_{DSS}$

Initialization of the Program:

Step 1: $e_{11F}(s) = \dfrac{h(s)}{g(s)}$ (front end)

$\qquad h_0 = 0$ (design without transformer)

$\qquad h_1 = -1, h_2 = -1$

Step 2: $e_{11B}(s) = \dfrac{h(s)}{g(s)}$ (back end)

$\qquad h_0 = 0, h_1 = 1, h_2 = 1, h_3 = 1$

Result of Optimization:

$$e_{11F}(s) = \frac{0 - .216S - .681S^2}{1 + 1.187S + .681S^2} \qquad \text{(Step 1)}$$

$$e_{11B}(s) = \frac{0 + 1.884S + .718S^2 + 2.317S^3}{1 + 2.821S + 2.204S^2 + 2.317S^3} \qquad \text{(Step 2)}$$

The gain performance of the overall amplifier is:

$T(\omega) = 7.35 \mp 0.33 \; dB$

and it is shown in Fig. 4.

Synthesis of the matching networks is carried out along with the numerical work by continuous fraction expansion of the input impedances.

$$Z_i = \frac{1 + e_{11i}(s)}{1 - e_{11i}(s)} \; ; i = \text{F or B.}$$

Final design of the amplifier is shown in Fig. 3.

Discussion: The same example is also solved by varying the element values of the amplifier topology shown in Fig. 4 to optimize the gain. In this work, computer package Supercompact was employed with the following initializations:

(a) Element values are set to 1 nH for inductors and 1 pF for capacitors.

We think that this independent initialization is reasonable for comparative purposes since the unknown coefficients of the simplified real-frequency technique were set to $h_i = \mp 1$. The goal for Supercompact optimization was to approximate the flat gain level 7.5 dB over the passband. Despite the use of both gradient and random search options simultaneously, the best Supercompact can offer for this problem, under the conditions given above, was

$$T(\omega) = 6.81 \mp 0.57 \text{ dB}$$

(Fig. 4, curve b) whereas the new technique presented in this paper yields higher gain with smaller ripple.

(b) When the element values obtained via the new procedure were used to initialize Supercompact for the gain optimization, improvement in the performance was negligible.

A similar experiment was also carried out using the in-house package Cosmic; we ended up with performance similar to that obtained from Supercompact.
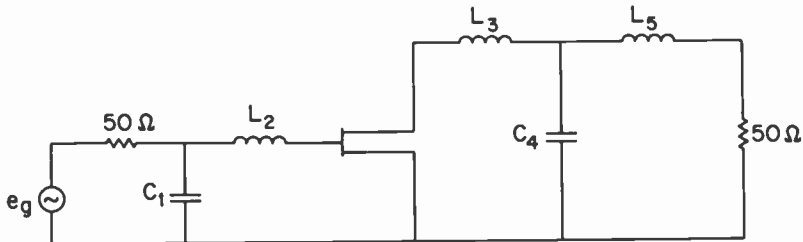
Fig. 3—Design of the amplifier of example 1. C_1 = 0.279 pF, L_2 = 0.482 nH, L_3 = 1.55 nH, C_4 = 0.186 pF, L_5 = 0.788 nH
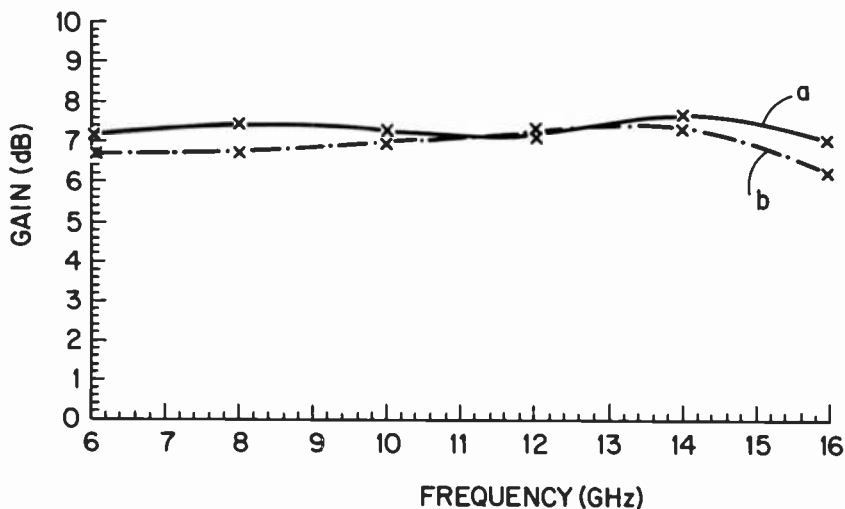
Fig. 4—Curve a: performance of the amplifier shown in Fig. 3. Curve b: performance obtained using Supercompact.

Example 2

In this example we show the extension of the technique to the design of multistage amplifiers in a manner similar to that discussed in Ref. [2].

It is desired to design a two-stage amplifier using the HFET-2001 over the frequency band (6 GHz–16 GHz). The complete design consists of three steps. In the first step, the front-end matching network E_F is developed as in the previous example. In the second step the interstage matching network E_I is constructed when the FET-2 is terminated in perfect match S_0 (Fig. 5). At this step, the gain formula can easily be generated using Eq. [7], provided T_g is replaced by the gain of the previous stage. Finally, the back-end matching network E_B is developed to optimize the overall gain of the amplifier. Inputs to the SEMA program and the performance of the amplifier are summarized as follows:

Generator: $S_G = 0$ ($Z_G = 50\ \Omega$)
Load   : $S_L = 0$ ($Z_L = 50\ \Omega$)

Complexity of the matching networks:

$n = 3$, $k = 0$ are chosen for all the matching networks.

Devices: FET-1 and FET-2 are identical as in the previous example. Initialization: At each step unknown coefficients are initialized as $h_i = \mp 1$, $i = 1, 2, 3$.
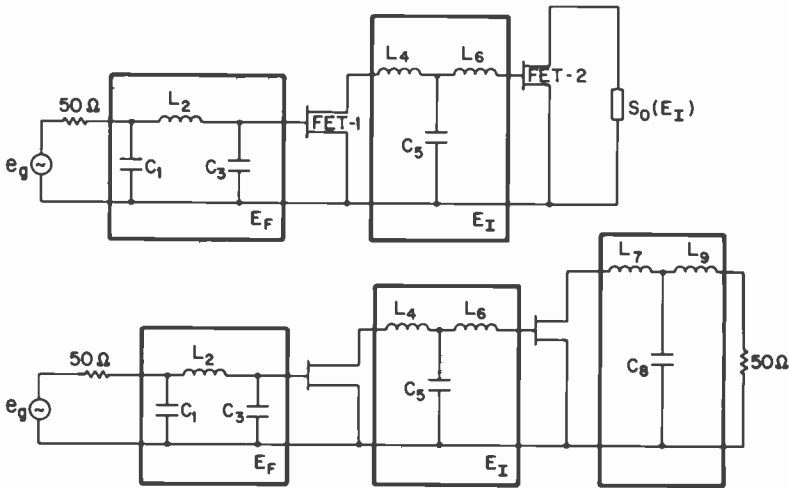
Fig. 5—Top: design of 2-stage amplifier of example 2: steps 1 and 2. Bottom: completed design (step 3). $C_1 = 0.278$ pF, $L_2 = 0.442$ nH, $C_3 = 0.127$ nH, (Step 1); $L_4 = 1.88$ nH, $C_5 = 0.234$ pF, $L_6 = 0.869$ nH, (Step 2); $L_7 = 1.767$ nH, $C_8 = 0.18$ pF, $L_9 = 0.974$ nH, (Step 3).

Flat gain levels:

$$T_{01} = 6.8 \text{ dB} \hspace{4cm} \text{(step 1)}$$

$$T_{02} = 13.6 \text{ dB} \hspace{4cm} \text{(step 2/3)}$$

Results of the optimization at each step are given as follows:

$$e_{11F}(s) = \frac{0 - 0.57S + 0.336S^2 - 0.397S^3}{1 + 1.462S + 0.904S^2 + 0.397S^3} \hspace{2cm} \text{(step 1)}$$

$$e_{11I}(s) = \frac{0 + 2.179S + 1.198S^2 + 3.88S^3}{1 + 3.35S + 3.25S^2 + 3.885S^3} \hspace{2cm} \text{(step 2)}$$

$$e_{11B}(s) = \frac{0 + 2.202S + 0.723S^2 + 3.158S^3}{1 + 3.21S + 2.501S^2 + 3.158S^3} \hspace{2cm} \text{(step 3)}$$

The overall gain performance of the amplifier is (Fig. 6)

$$T(\omega) = 13.234 \mp 1.14 \text{ dB}$$

Synthesis of the reflection coefficients is carried out along with the computations as in example 1 and the complete amplifier is shown in Fig. 5.

Discussion: The same example may also be solved by computing the element values of the chosen circuit topologies for the matching

networks to optimize the overall gain. But this process would be difficult since the gain function of the amplifier is a highly non-linear combination of the element values of the matching networks. However, once the design values are obtained using the new technique discussed above, they may be corrected to reduce the ripples of the gain function. Using our in-house program Cosmic,[3] element values of Fig. 5 were recomputed to reduce the gain variations in the passband. This optimization yields $T(\omega) = 12.25 \mp 0.28$.

As can be seen from Fig. 6, gain variation over the passband is significantly reduced and there is the lower gain, which is also expected.

Example 3

Employing the dynamic design procedure together with the simplified real-frequency technique, we evaluated the gain capability of a 4-cell Raytheon chip RPX-6036. For this purpose, several amplifier designs were studied with different bandwidths in X-band. Finally, an amplifier was built for the 10.9- to 11.2-GHz frequency band (Fig. 7). The performance of the actual amplifier is summarized as follows (Fig. 8):

Gain: 4.5 ± 0.215 dB
Efficiency: $20.5 \pm 2\%$
Output Power: 4 ± 0.02 W (Fig. 9)
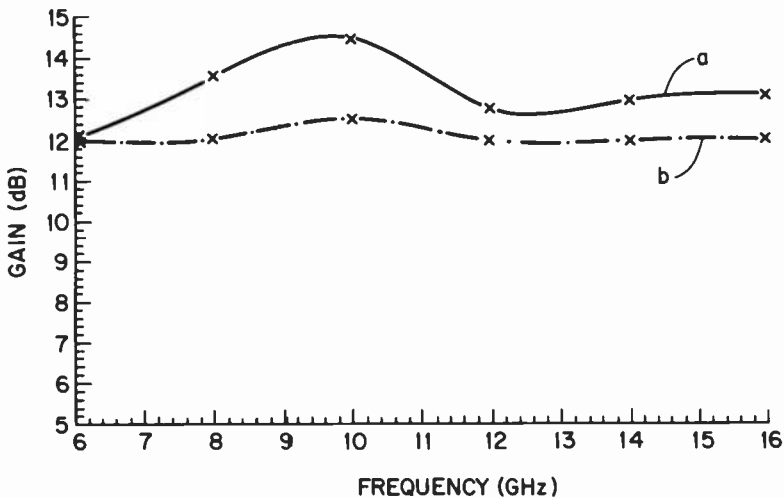
Fig. 6—Curve a: performance of the amplifier shown in Fig. 5 (bottom) Curve b: performance obtained using Cosmic.
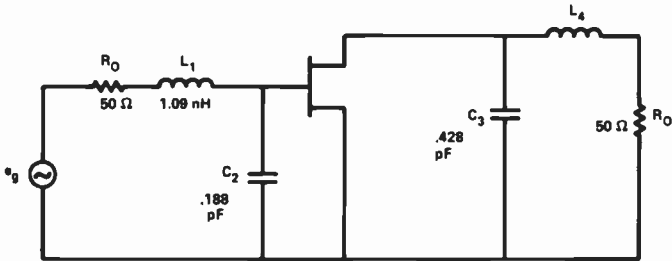
Fig. 7—Design of the power amplifier of example 3.

Since the computational steps in this example are the same as those of example 1, details are omitted here. However, for comparison, our theoretical computations based upon the measured scattering parameters yield the transducer power gain $T(\omega) = 4.3 \pm 0.12$ dB (Fig. 8). The difference between the results may be explained by the inaccuracy in the measurements of the scattering parameters and the implementation of the circuit elements. However, actual and predicted gains are in reasonable agreement.

It should be noted that during the initial design stage, optimizations of gain performance of the amplifiers with different bandwidths were attempted for an improvement utilizing the other available CAD procedures.[3,4] However, there was no significant change in the performance.
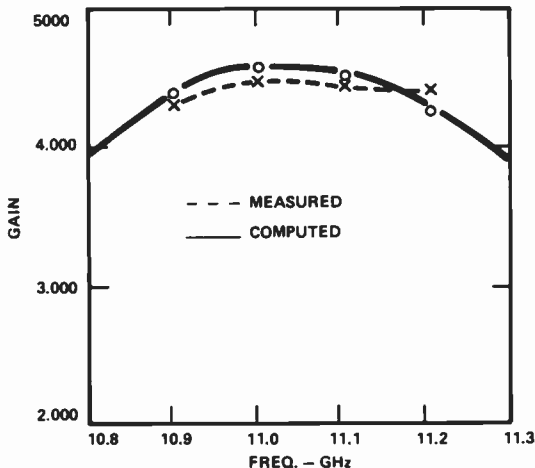
Fig. 8—Computed and measured performances of the amplifier shown in Fig. 7.
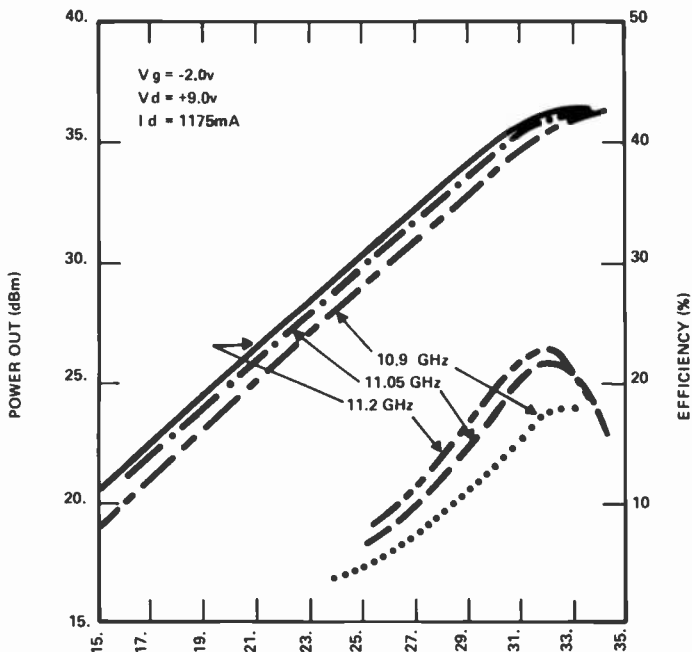
Fig. 9— Pin vs. Pout and efficiency plots of the actual amplifier shown in Fig. 7.

7. Conclusion

A new dynamic CAD procedure for designing broadband microwave amplifiers is presented. The new method takes less computation time and yields superior amplifier gain performance over the other commercially available CAD procedures. Examples are presented to show the application of the new method. It is also demonstrated that the new procedure is suitable for designing linear power amplifiers. An X-band power amplifier was designed and built employing the technique. The laboratory tests exhibit reasonable agreement with theoretical computations.

Acknowledgment

The author wishes to thank Dr. H. Huang for his encouragement of this work.

References:

[1] B. S. Yarman, "A Simplified Real Frequency Technique for Broadband Matching a Complex Generator to a Complex Load," *RCA Rev.* **43**, pp. 529–541, September 1982.

[2] B. S. Yarman and H. J. Carlin, "A Simplified Real Frequency Technique Applied to Broadband Multistage Microwave Amplifiers," *IEEE Trans MTT*, December 1982.
[3] B. Perlman, private communication.
[4] Compact Engineering, "Super Compact User Manual," Compact Engineering 1131 San Antonio Rd, Palo Alto, CA, 94303.
[5] K. M. Brown and J. E. Dennis, "Derivative Free analogues of the Levenberg-Marquard and Gauss Algorithms for Nonlinear Least Square Approximations," *Numerische Mathemetic* **18**, p. 289, 1972.
[6] Hewlett Packard, Inc. "Microwave Semiconductor Diode and Transistor Designer's Catalog 1982–1983," p. 172, Hewlett Packard Components, 350 West Trimble Rd., San Jose, CA, 95131.

A Computer-Controlled Microwave Tuner for Automated Load Pull

F. Sechi, R. Paglione, B. Perlman, and J. Brown
RCA Laboratories, Princeton, NJ 08540

Abstract—A computer-controlled tuner, useful for large-signal character-
ization of power devices, was implemented around a mechan-
ical tuner driven by stepping motors. An important part of this
automated system is the algorithm that guides the search. The
algorithm is based on a novel simplified tuner model and gra-
dient search technique that is accurate and efficient.

1. Introduction

One of the important parameters in the design of a microwave cir-
cuit is the rf impedance presented at specified ports in the circuit.
In those cases where one is designing circuits incorporating active
devices and simple S parameter characterization is insufficient, it
is necessary to empirically determine the performance of the active
device as a function of the impedance of the load or of the generator.
This information is particularly important when one is designing
for optimum performance with respect to power, efficiency, or noise.
In practice, it is often difficult to obtain this data, however, since
calibrated tuners that provide the wanted values of impedance at
the test port are not readily available. The difficulty is a conse-
quence (1) of the complexity of the relationship between the position
of tuning elements and the impedance at the test port at a specific
frequency and (2) of the difficulty in achieving sufficient precision
and repeatability in the mechanism driving the tuning elements.

One technique to achieve the effect of a variable tuner while mon-
itoring load impedance in real-time is described in Ref. [1]. Variable
output loading is obtained by utilizing the interference between two
separate rf signals, one of which is adjustable in amplitude and
phase. Other systems have been developed that are based on active

tuners.[2,3] Since a regular network analyzer is used to measure the load impedance dynamically, these systems typically cannot be readily used for pulse operation or with multiple rf signals. In addition, these techniques are not suitable to provide a variable source impedance for applications such as noise-figure measurements.

An alternative technique has been described that uses an electrically settable low-loss slug tuner. The load-pull system described in this paper is representative of a second generation of this concept.[4]

The original tuner, which used a servomotor-controlled configuration was characterized by inaccuracies resulting from hardware as well as software. Specifically, the position of the tuning elements could drift during the time of the experiment and repeatability of results was poor. The algorithm used for controlling the tuner in an automatic search mode would often bog down in idle loops with a consequent waste of computer time. These problems have been solved by (1) a substantially improved mechanical construction, (2) the use of a digitally-controlled stepper-motor positioning system (instead of servomotors), (3) the use of optical position sensors, (4) improved instrumentation, and (5) improved search algorithms. These algorithms, based on a new method for characterizing and modeling the tuner line, are precise and efficient.

2. Description of the Instrument

2.1 System Configuration

Fig. 1 is the block diagram of a load-pull system. The automatic tuner is connected at the input of the device under test (DUT). Typically, the device is mounted in a test fixture that includes matching networks whose effects are accounted for in the computer program. An rf signal source is connected to the input through a low-pass filter to remove harmonic signals that affect the search algorithms. The input and output rf power levels are measured by meters interfaced to the computer through a general purpose interface bus (IEEE std 488). Bias voltages and currents are measured by an A/D converter through a simple scanning circuit. The instruments are controlled by a dedicated minicomputer (Hewlett Packard 1000F) and a multiprogrammer (Hewlett Packard Model 6942A) that includes hardware interfacing to the analog instruments. Stepping-motor cards provide trains of pulses to the motor control unit. The input data are entered on a video terminal and the results are drawn on Smith charts by a plotter.
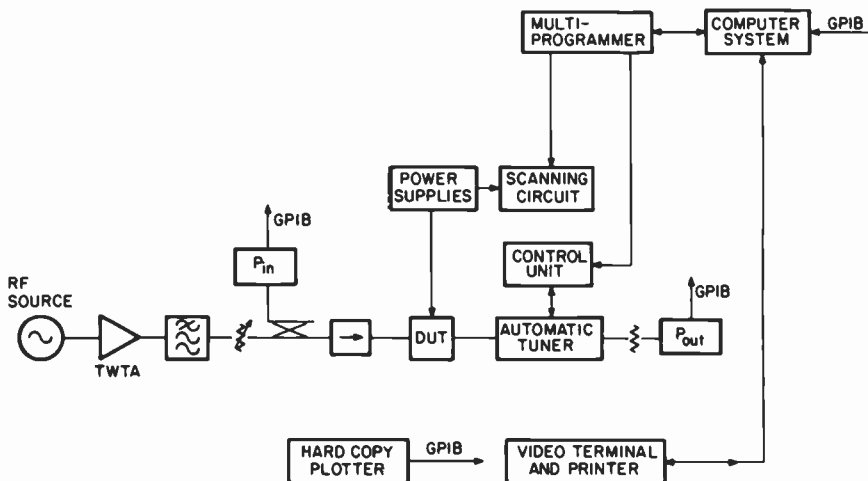
Fig. 1—Load-pull system for computer-controlled microwave tuner.

2.2 Tuner Design

Fig. 2 is a photograph of the tuner designed for operation at X and Ku band. A similar unit, designed for operation from UHF to C band, is shown in Fig. 3. Each tuner consists of a 50 Ω line equipped with short low-impedance elements (slugs) riding on the center conductor. These slugs provide a maximum VSWR of approximately 5:1 over the operating bandwidth and are driven by high-precision stepping motors. The mechanical resolution, one step of the motors, is 1/2 mil and 1 mil for the first and second unit, respectively. Photosensors at the center of the line reset the slugs at a well-defined starting point. Two photosensors at the ends of the line protect the slugs from colliding with the end stops in the event of a system malfunction or an operator error. A third sensor detects if the two slugs are about to collide with one another.

3. Theory of Operation
3.1 Line Characterization

The tuner with its two slugs can be electrically described by the circuit of Fig. 4, where L_1, L_2, and L_3 are lengths of 50 Ω line. These lengths are variable with the condition that

$L_1 + L_2 + L_3 = L_0$.

L_0, a constant for a given tuner, represents the maximum available
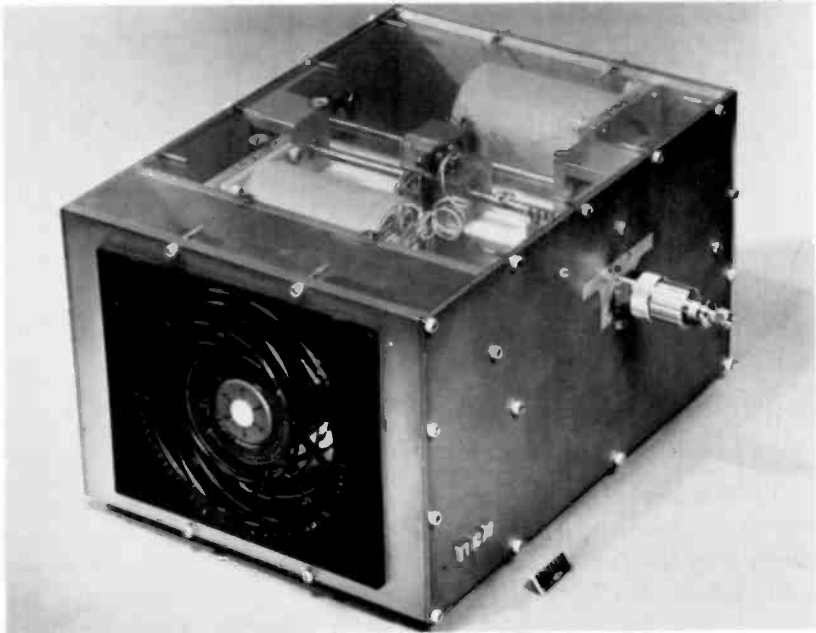
Fig. 2—Ku-band tuner.

travel for the slugs. T_1 and T_2 are networks representing the transition elements required to connect the tuner to the outside circuit. Port 2 is the test port and is connected to the device under test. The impedance and, consequently, the reflection coefficient at the test port are computed at any frequency from the exact equivalent circuit of the tuner and known data describing the impedance used to
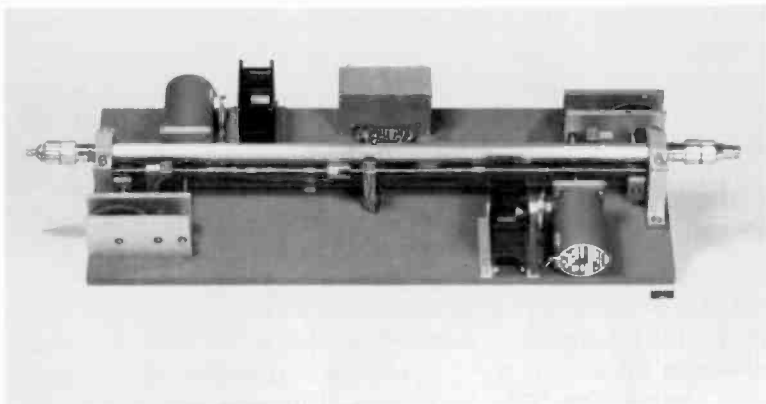
Fig. 3—C-band tuner.
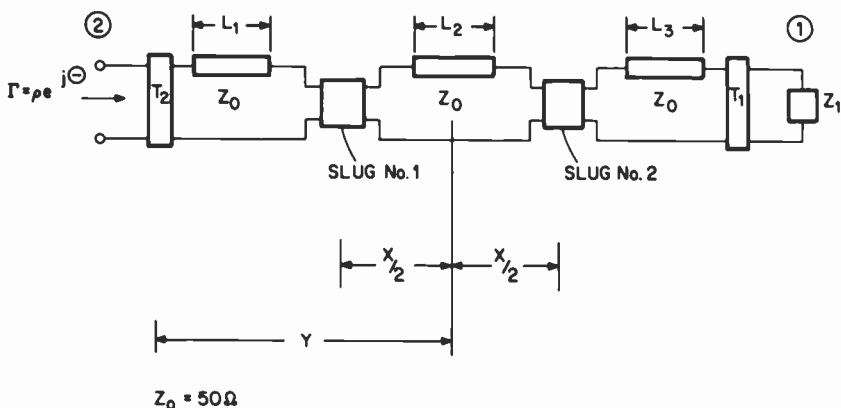
Fig. 4—Tuner equivalent circuit.

terminate Port 1. The accurate equivalent circuit, including the effects of discontinuities and losses in the lines, was obtained by measuring the impedance at the test port at known values of slug positions L_1, L_2, L_3, and at known frequencies. A computer optimization program was used to slightly vary the design values of lengths and characteristic impedances of the tuning slugs in order to best fit the measured data.

3.2 Reflection Coefficient as a Function of Slug Positions

An efficient search algorithm requires that the position of the tuning slugs be determined for any prescribed reflection coefficient. This would require the inversion of complicated equations derived from multiple cascaded transmission lines. Attempting to achieve the result by iteration is very time consuming and is intolerable when the process has to be repeated thousands of times, as is the case when using an automatic search routine. Therefore, it is useful to develop a simplified model of the line to guide the automatic search process. When the specified point is reached with this approach, a very accurate value of the reflection coefficient can be computed from the equivalent circuit of the line. The basis for a simplified model is shown in Fig. 5 where the reflection coefficient $\Gamma = \rho e^{j\theta}$ is drawn as a function of the slug separation x. For simplicity, an impedance Z_1 equal to 50 Ω is assumed in this case. Any value of ρ between zero and a maximum value, ρ_M, can be obtained with a slug separation x between x_o and $x_o + (\lambda/4)$. A further increase of x up to $x = x_o + \lambda$ causes Γ to follow the figure-eight shaped dotted line. The maximum difference between θ and the
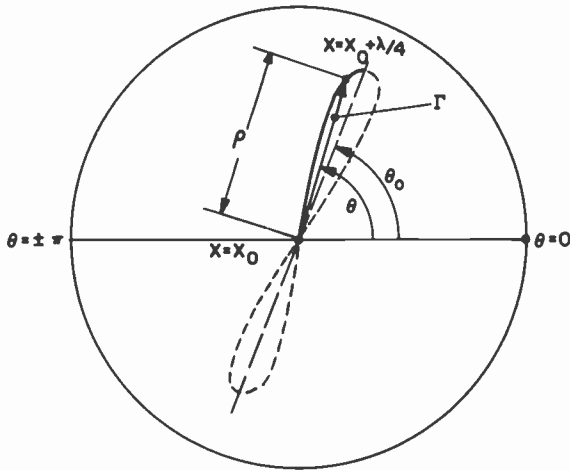
Fig. 5—Reflection coefficient versus slug separation.

average θ_0 is a function of the electrical length and characteristic impedance of the lines that make up the slugs and typically has been contained to approximately 10°.

A plot of ρ as a function of the slug separation x is shown in Fig. 6. It is interesting to see that a simple sinusoid can approximate the actual function $\rho(x)$. Thus, accepting a small error, we can write

$$\rho(x) \; = \; \rho_M \sin \; \left(\frac{\pi}{2} \, \frac{x \; - \; x_0}{\lambda} \right) \tag{1}$$

$$x(\rho) \; = \; x_0 \, \frac{2\lambda}{\pi} \sin^{-1} \left(\frac{\rho}{\rho_M} \right) \tag{2}$$

Eq. [2] allows the approximate computation of the slug separation for a specified value of ρ.
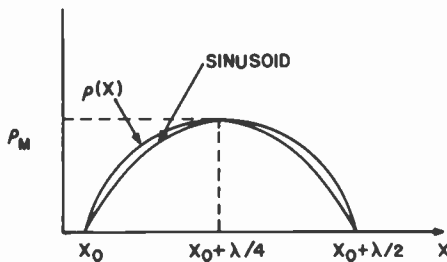
Fig. 6—Magnitude of reflection coefficient versus slug separation.

It can easily be seen that the phase of the reflection coefficient, θ, is a linear function of the length y, which defines the position of the center of symmetry between the slugs. Also, the phase varies by 2π for multiples of $\pi/2$. Thus, θ can be expressed as

$$\theta = 4\pi \frac{y - y_0}{\lambda}, \tag{3}$$

where y_0 is defined by

$\theta(y_0) = 0$.

Thus, y is expressed as a function of θ by

$$y(\theta) = y_0 + \frac{\lambda\theta}{4\pi}. \tag{4}$$

Therefore, Eqs. [2] and [4] allow us to define the position of the slugs for any specified value of Γ. These equations are simple and only require a small computation time; therefore, they are well-suited for efficient automatic search routines operating at high speed. It is also useful to express them in their incremental form:

$$\Delta x = \frac{\Delta\rho}{\rho_M} \cdot \frac{2\lambda}{\pi} \frac{1}{\cos\left(\dfrac{\pi}{2} \cdot \dfrac{x - xo}{\lambda}\right)} \tag{5}$$

$$\Delta y = \Delta\theta \frac{\lambda}{4\pi} \tag{6}$$

Eqs. [4] and [5] define the variation of the slug position, Δx and Δy, for a specified variation of the reflection coefficient expressed by $\Delta\rho$ and $\Delta\theta$.

3.3 Gradient of *W*

A tuner is generally used in a circuit to measure the effect of an impedance variation on such quantities as power, efficiency, gain, and noise-figure. Any such quantity, either directly measured or computed from measurements, is a scalar and will be represented by $W(\Gamma)$, where W is power, efficiency, gain, NF, etc. and Γ is the reflection coefficient.

If we assume that the derivative of W with respect to Γ is independent of the direction of approach; then $dW/d\Gamma$ is defined. Math-

ematically, this condition is expressed by saying that W is analytical. It is safe to assume that this condition is satisfied if the system is memoryless (no hysteresis). To devise efficient search algorithms, it is useful to compute the gradient of the function W at any value of Γ, since the direction of the gradient gives the direction of the maximum variation of W. In polar coordinates the gradient is expressed by:

$$\nabla W = \mathbf{a}_\rho \frac{\partial W}{\partial \rho} + \mathbf{a}_\theta \frac{1}{\rho} \frac{\partial W}{\partial \theta}, \qquad [7]$$

where $\mathbf{a}_\rho$ and $\mathbf{a}$ are unity vectors in the radial and in the tangential direction, respectively. Fig. 7(a) is a graphical representation of ∇W in the reflection coefficient plane (Smith Chart).

Although one variation in the radial direction and one in the tangential direction would be sufficient to numerically determine the partial derivatives of W, the accuracy is improved by computing the gradient at point 0, as shown in Fig. (7b).

(a)

(b)
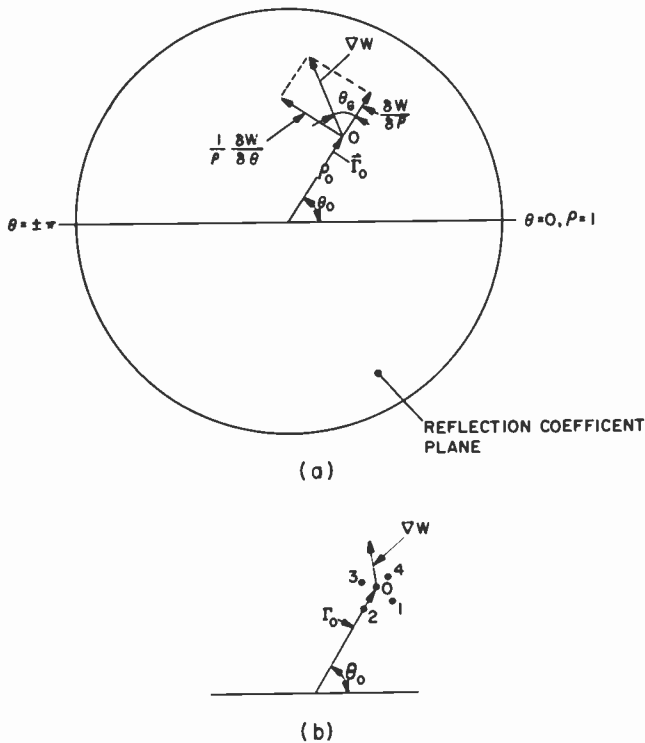
Fig. 7—Gradient of W: (a) W in the reflection coefficient plane and (b) gradient at point 0.

At point 0, the direction for maximum variation of W is defined in polar coordinates by the angle:

$$\theta_M = \theta_0 + \theta_G = \theta_0 + \tan^{-1} \frac{\dfrac{\partial W}{\partial \theta}}{\rho \dfrac{\partial W}{\partial \rho}}. \qquad [8]$$

This angle, θ_M, is of particular importance for the search algorithm.

3.4 Search for Maxima or Minima of W

Let's consider the search for the maximum value of W, assuming that only one maximum is present in the range of interest for Γ. The function $W(\Gamma)$ can be visualized as a surface subtending a Smith Chart, as shown in Fig. 8. The search starts at point 1 by computing ∇W. Eq. [8] defines the angle θ_M on the Γ plane, which is the direction along which the change of W is a maximum. Now, an auxiliary scalar search variable, s, is defined to provide steps along the direction of ∇W. s_1 and Γ_1 are the values of s and Γ at point 1. The reflection coefficient at point 2 is given by

$$\Gamma_2 = \Gamma_1 + (s_2 - s_1)e^{j\theta_M}, \qquad [9]$$

where $(s_2 - s_1)$ is the magnitude of the reflection-coefficient step. A projection of the search on the Γ plane is shown in Fig. 9(a). Having defined Γ_2, Eqs. [2] and [4] allow us to move the slugs and
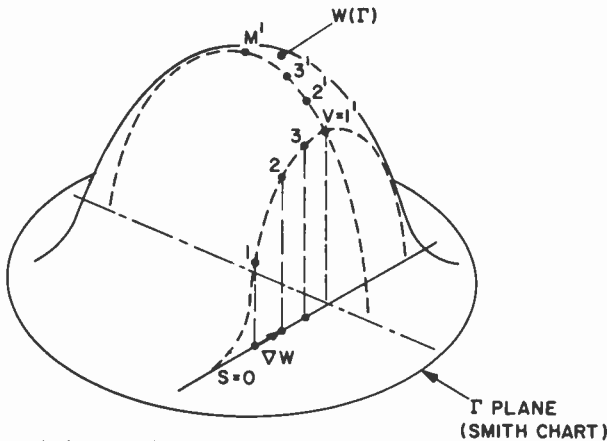
Fig. 8—Search for maximum W.

(a)

(b)
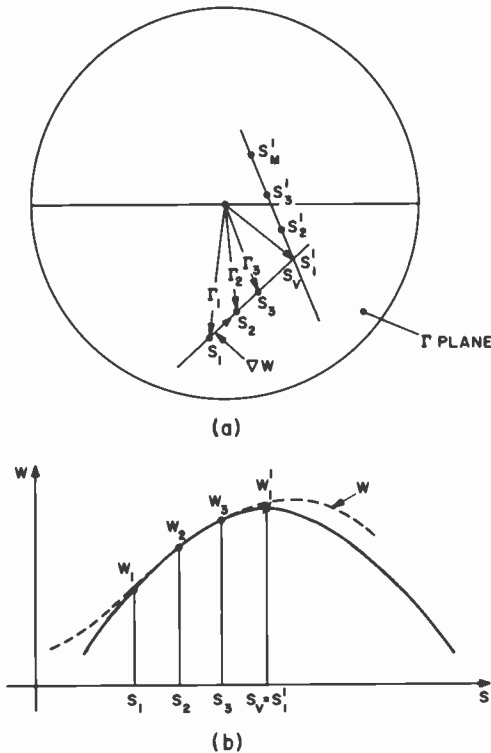
Fig. 9—Projection of W_{max} search: (a) search for Γ_2 point and (b) parabola fitted through three points to estimate maxima.

measure W at point 2. This same procedure is repeated and W is measured at point 3. To estimate the position of the maximum of the function W, a parabola is fitted through the three measured points as shown in Fig. 9(b). The position s_v of the vertex v is given by

$$s_v = \frac{1}{2} \cdot \frac{W_1\,(s_2^2 - s_3^2) - W_2\,(s_1^2 - s_3^2) + W_3\,(s_1^2 - s_2^2)}{W_1(s_2 - s_3) - W_2\,(s_1 - s_3) + W_3\,(s_1 - s_2)}. \quad [10]$$

The corresponding reflection coefficient is

$$\Gamma_v = \Gamma_1 + (s_v - s_1)\,e^{j\theta M}. \quad [11]$$

The slugs are then set to a position corresponding to Γ_v, W is measured, and this point becomes the start for a new search cycle. For s_v to be accepted as a proper value, certain conditions have to be satisfied:

(1) s_v must correspond to a maximum and not a minimum; therefore, the parabola must have a negative curvature. This can be expressed by

$$W_1(s_2 - s_3) - W_2(s_1 - s_3) + W_3 (s_1 - s_2) < 0. \qquad [12]$$

(2) To avoid the pitfalls resulting from an extrapolation too far from the starting point, it is required that

$$|s_v - s_3| < K |s_3 - s_2|. \qquad [13]$$

In words, Eq. [13] requires the vertex to be within K step lengths from the previous point. If either [12] or [13] are not satisfied, the new starting point is chosen to be the one of the three measured points corresponding to the highest value of W. The iterative procedure is continued until a test on successive values of W_v shows that the maximum has been reached.

The above procedure assumes the existence of only one maximum of W. In the event of local maxima, this procedure would locate a maximum close to the starting point. Other maxima can then be located by starting the search at different points.

The problem of searching for a minimum of W can be immediately solved by noting that a minimum of W is a maximum of $-W$. Thus, a simple change in sign allows us to use the algorithm just described to search for a minimum of W.

3.5 Search for Target Values

It is useful to be able to set the tuner so that the function W assumes a specified value within its range of existence. In particular, this is a prerequisite for the search of contours of constant W that is described in Sec. 3.6. Defining W_t as the specified target value for W, the search can be reduced to a search for a zero of the function

$$F = W - W_t. \qquad [14]$$

The algorithm starts similarly to the one described in Sec. 3.4 and depicted in Fig. 9(a). At point 1 (starting point), W and ∇W are measured. An arbitrary step in the direction of ∇W is then taken, the corresponding reflection coefficient is computed, and the tuner slugs are moved accordingly. The function W is read at this point (point 2), and the third point is computed with the following iteration formula:

$$s_3 = s_2 + (s_2 - s_1) \frac{F_2}{F_1 - F_2}. \qquad [15]$$

This formula is derived from the secant method outlined in Fig. 10. Should the series not converge to zero, which is the case when the path on the reflection coefficient plane is tangent to or does not intercept the constant W_t contour, then the search starts anew by measuring W and resetting a new direction of search from the point of minimum F. Also, the new-start procedure is followed when

$$|s_3 - s_2| < K |s_2 - s_1|, \tag{16}$$

that is, when s_3 is farther than K steps from s_2.

3.6 Search for Contours of Constant W

The purpose of this search is to define the locus of the reflection coefficients that produce a constant value of W. The first step is the measurement of ∇W at the starting point, where $\Gamma = \Gamma_o$. As depicted in Fig. 11, the gradient ∇W is orthogonal to the line of constant W; thus, the first search vector is extended in a direction orthogonal to W, and the tuner is set for a reflection coefficient:

$$\Gamma_1 = \Gamma_o + \rho_s e^{j(\theta_M \pm \pi/2)} = \Gamma_o + \rho_s e^{j\theta_{s1}}, \tag{17}$$

where ρ_s and θ_{s1} are the amplitude and phase of the search vector. The $+$ or $-$ sign defines the direction of the search. Having measured $W_1 = W(\Gamma_1)$, the algorithm rotates the search vector by an angle $\Delta\theta$

$$\Gamma_2 = \Gamma_0 + \rho_s e^{j\theta_{s2}},$$

where

$$\theta_{s2} = \theta_M \pm \frac{\pi}{2} + \Delta\theta, \tag{18}$$
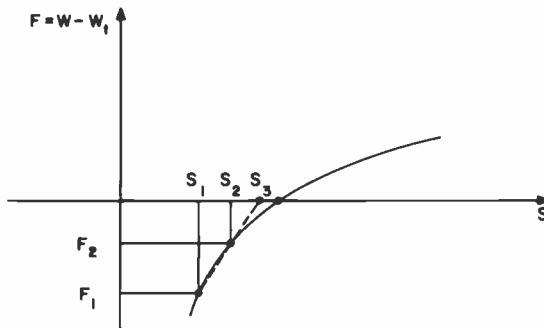
Fig. 10—Search for W_t (iterative search).
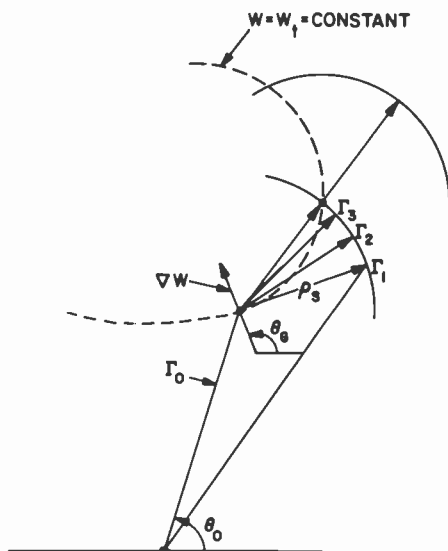
Fig. 11—Search for contour of constant W.

and W is measured at this second point $W_2 = W(\Gamma_2)$. The recurrence formula, derived again from a secant method, is expressed by

$$\theta_{s3} = \theta_{s2} \left(1 + \frac{W - W_t}{W_1 - W_2} \right). \tag{19}$$

The slugs move to a position corresponding to

$$\Gamma_3 = \Gamma_0 + \rho_s e^{j\theta_{s3}}, \tag{20}$$

which defines a point closer to the target. When a point on the contour $W = W_t$ is found, the search restarts by extending from this point a vector equal to the one defining the last successful point. The second point is obtained, as before, by sweeping the search vector for an angle of $\Delta\theta$. The iteration procedure is then repeated. The relatively time-consuming measurement of ∇W is performed only at the beginning of the search or when no successful point is found in the prescribed search radius. In either case, the tuner is reset to the last successful point, the gradient is measured, and the search routine starts from the beginning.

To avoid a backtrack of the search on the same contour, it is useful to set

$$|\theta_{sn} - \theta_{si}| < \theta_{max}; \; i, n = 1, 2, 3 \tag{21}$$

where θ is the angle of the search vector and θ_{max} is an angle typically equal to $\pi/2$.

3.7 Impedance Setting

An important feature of this computer-controlled system is the capability of setting the tuner to any prescribed impedance specified within its range of maximum VSWR. Often this impedance setting is the starting point of an automatic search. The target reflection coefficient Γ_{t0} corresponding to the prescribed impedance and the first estimate Γ_1 (from the simplified model) are shown schematically in Fig. 12. The resultant error is

$$E_1 = \Gamma_{t0} - \Gamma_1. \tag{22}$$

The iterative procedure is based in essence on "adjusting the aim", in a manner reminiscent of target shooting, by choosing a virtual target Γ_{t1} defined as

$$\Gamma_{t1} = \Gamma_{t0} + E_1 = \rho_{t1}e^{j\theta_{t1}}. \tag{23}$$

The new slug positions, x_2 and y_2 derived from ρ_{t1} in Eq. [2] and [4] define Γ_2, computed with the exact model. For convergency,

$$|E_2| = |\Gamma_{t0} - \Gamma_2| < |E_1|. \tag{24}$$

Thus the nth iteration is as follows:

$$\Gamma_{tn} = \Gamma_{t0} + E_n = \rho_{tn}e^{j\theta_{tn}} \tag{25}$$

$$x_{n+1} = x_0 + \frac{2\lambda}{\pi}\sin^{-1}\left(\frac{\rho_{tn}}{\rho_M}\right) \tag{26}$$

$$y_{n+1} = y_0 + \frac{\lambda\theta_{tn}}{4\pi} \tag{27}$$

$\Gamma_{n+1}(x_{n+1}, y_{n+1})$ computed from the exact model
$$E_{n+1} = \Gamma_{t0} - \Gamma_{n+1} \tag{28}$$

Under most conditions the series of Γ_n converges rapidly toward Γ_{t0}. For instance, only 3 to 4 iterations are typically required for $|E_n| <$ 0.05. However, if E_1 (the initial error between the simplified and the exact model) is large, the algorithm might not find a path of convergency. An alternate iteration procedure, based on the incremental Eqs. [5] and [6], may be used. This is considered more resistant to the static error of the simplified model. The iteration in the incremental form is
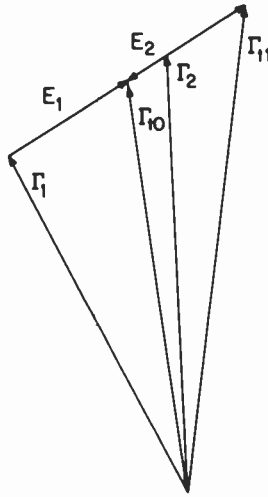
Fig. 12—Search for impedance setting.

$$E_n = \Gamma_{t0} - \Gamma_n = \rho_n e^{j\theta_n} \tag{29}$$

$$\left.\begin{array}{l} \Delta x = \left(\dfrac{\rho_n}{\rho_M}\right)\dfrac{2\lambda}{\pi}\,\dfrac{1}{\cos\left(\dfrac{\pi}{2}\dfrac{x - x_0}{\lambda}\right)} \\[4ex] \Delta y = \theta_n \dfrac{\lambda}{4\pi} \end{array}\right\} \tag{30}$$

$$\left.\begin{array}{l} x_{n+1} = x_n + \Delta x \\ y_{n+1} = y_n + \Delta y \end{array}\right\} \tag{31}$$

$$\left.\begin{array}{l} \Gamma_{n+1}\,(x_{n+1}, y_{n+1}) \text{ computed from exact model} \\ E_{n+1} = \Gamma_{t0} - \Gamma_{n+1} \end{array}\right\} \tag{32}$$

3.8 Tuner Losses

Estimating the internal loss of the tuner is important, particularly when losses are substantial, which is common at high frequencies. However, losses vary with frequency and with the position of the slugs in a manner that is not predictable with simple models.

The approach that led to a convenient formulation of tuner loss is based on the general representation of active power in a two-port device. Following the nomenclature of Fig. 13, the power entering port 1 (P_1) and the power exiting port 2 (P_2) are expressed by:

Fig. 13—Tuner loss.

$$P_1 = \text{Re}\,(V_1 \cdot I_1) \atop P_2 = \text{Re}\,(V_2 \cdot I_2^*) \Bigg\} \tag{33}$$

The tuner loss, as the ratio between input to output power in terms of the ABCD parameters of the complete tuner, can then be expressed by:

$$\frac{P_1}{P_2} = \text{Re}\,\left\{ (AZ + B)\,\left(C + \frac{D}{Z_2} \right)^{*} \right\}. \tag{34}$$

Although simple, this equation includes all losses, and no additional terms are needed to describe, for instance, the power lost by reflection at the input and output ports.

4. Examples

Mismatch circles, obtained with the low-frequency tuner at the low end of the band, are shown in Fig. 14. The tuner can be set at any impedance within a maximum VSWR of 5:1. Similar data, obtained with the high-frequency tuner at 15 GHz, are shown in Fig. 15. This tuner can be set at any impedance within a maximum VSWR of 7:1. The maximum VSWR for any particular tuner is a function of the characteristics of the tuning elements (characteristic impedance and physical length of the slugs) and of the frequency. The higher the maximum VSWR, the more critical the positioning of the slugs becomes for the required impedance and the less accurate is the modelling of the line. As a compromise, these tuners were designed for a maximum VSWR of at least 5:1 over their operating frequency range.

The accuracy of the system is affected by the operating frequency, which is reflected in the results of Figs. 14 and 15. Smoother impedance contours are obtained typically at lower frequencies where the mechanical resolution and reproducibility of the system as well as the limitations of the electrical modelling have a lesser effect. The mechanical resolution of these tuners (one single step of the motors) is 1/2 mil for the high frequency unit and 1 mil for the lower fre-
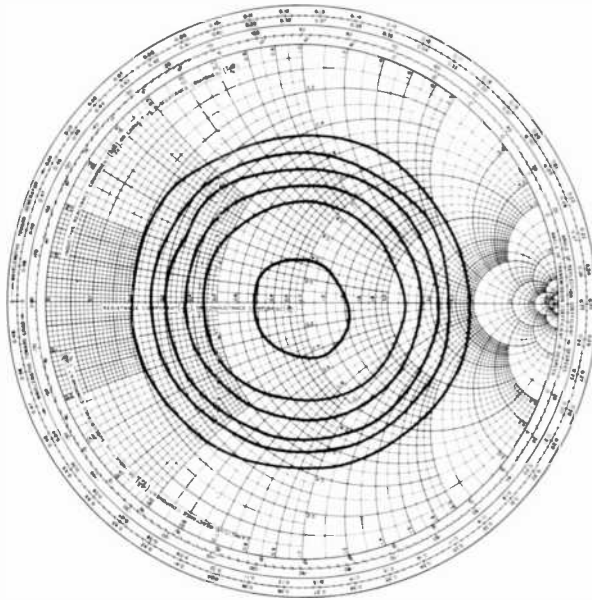
Fig. 14—Mismatch circles at 0.5 GHz (low-frequency tuner).

IMPEDANCE OR ADMITTANCE COORDINATES
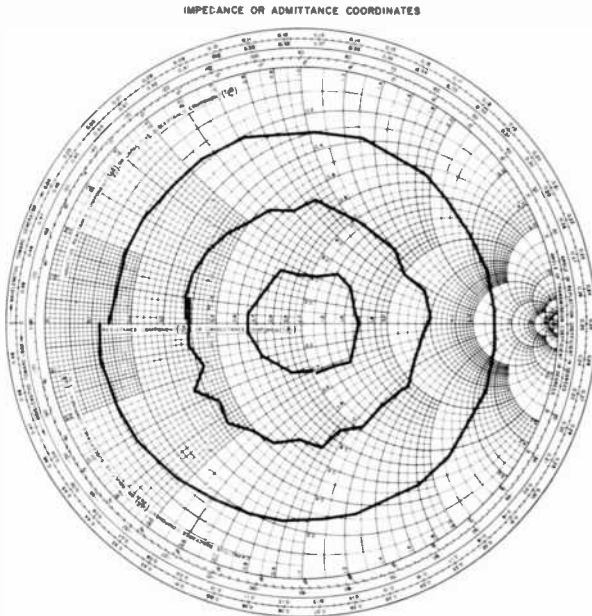
Fig. 15—Mismatch circles at 15 GHz (high-frequency tuner).

quency unit. The reproducibility is typically ± 2 steps for both tuners. The modelling accuracy is a function of the bandwidth over which the electrical model of the line is optimized. The reflection coefficient over the full bandwidth of the tuners was found to be accurate typically within ± 0.05. Higher accuracy, e.g., within ± 0.02, can be achieved by optimizing the line model over a narrower band at the expense of operational convenience.

5. Conclusions

A computer-controlled tuner is a useful instrument, particularly for large-signal characterization of power devices. A convenient implementation of the instrument includes a double-slug tuner controlled by stepping motors. An important part of the system is the automatic search algorithm. The key factor is to predict, in a simple form, the movement of the motors for a required impedance at the test port without resorting to the inversion of the complex equations derived from the transmission line model, a brute-force procedure that is time-consuming and not well suited for automatic searching. Selecting search variables that are orthogonal is also important in order to accurately derive the gradient of the function and to develop an efficient search algorithm. The problem is solved by introducing the concept of a simplified model of the tuner. Simple equations, which can be written to express the position of the tuning element as a function of impedance, guide the search. When a point satisfying the required conditions is found, the exact impedance is determined, without loss of accuracy, from an accurate transmission-line model of the tuner. The resultant search routines are well directed and therefore efficient.

Acknowledgment

References:

[1] Y. Takayama, "A New Load-Pull Characterization Method for Microwave Power Transistors," *Digest 1976 IEEE MTT-S International Microwave Symp.*, pp. 218–220, 1976.
[2] G. Bava, U. Pisani, and V. Pozzolo, "Active Load Technique for Load-Pull Characterization of Microwave frequencies," Electronic Lett., **18**, p. 178, 1982.
[3] R. B. Stancliff and D. D. Pauling, "Harmonic Load-pull," *Digest 1979 IEEE MTT-S International Microwave Symp.*, pp. 185–187.
[4] J. M. Cusack, S. M. Perlow, and B. S. Perlman, "Automatic Load Contour Mapping for Microwave Power Transistors," *IEEE Trans. on Microwave Theory and Tech.*, Part II, **12**, p. 1146, (1974).

Broadband Balun

Oakley M. Woodward
RCA Laboratories, Princeton, NJ 08540

Abstract—This paper describes a balun for converting an unbalanced impedance, Z, to a balanced impedance, $4Z$, with ideal balance efficiency and very low VSWR over a 7.5:1 frequency band.

Balun Geometry

The balun may be made with coaxial transmission line sections, as shown in Fig. 1. The unbalanced coaxial-line input, A, extends from one end of a large diameter cavity, B, which is one-quarter wavelength long at the mid-band frequency f_o. Two smaller coaxial lines, C and D, extend from the opposite end of the cavity to the balanced load.

Each of these three coaxial lines contain a coaxial metal tube supported by insulators inside of their inner conductors. These tubes are one-quarter wavelength long at f_o, and are open-circuited at one end to form a reactance in series with the input to each of the coaxial lines.

Coaxial line C is positioned within the cavity, B, so that the characteristic impedance of the line, formed by the cavity tube and coaxial outer conductor, is as high as possible. Coaxial line D is parallel to line C and positioned against the inner wall of the cavity.

The series reactance tube of line C is joined to the cavity short at E. The series reactance tube of line D is joined to the outer conductor end of line C and also to the series reactance tube of line A at F. Hence, lines C and D, each with its series reactance, are joined in parallel within the cavity. The quarter-wave cavity is in shunt with the paralleled loads. The unbalanced input line is connected through its series reactance across the paralleled outputs.

With this arrangement, the currents to the two halves of the balanced load are equal in magnitude and flowing in opposite di-
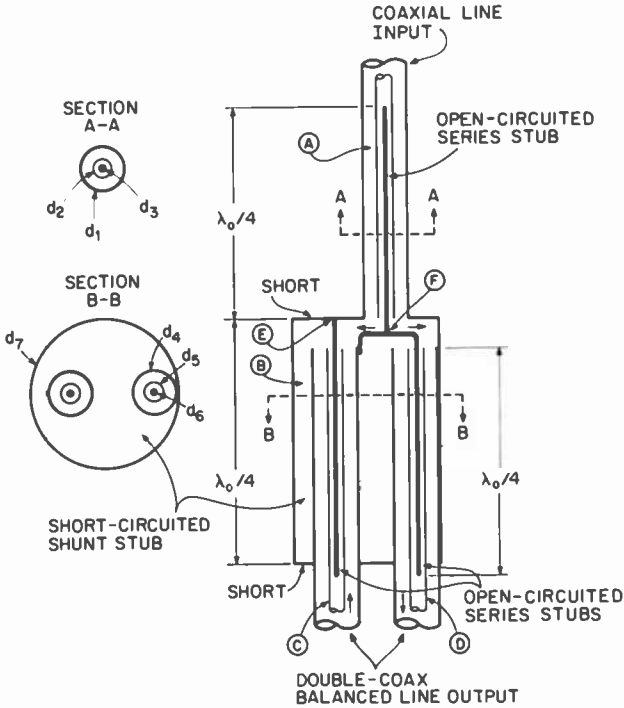
Fig. 1—Balun geometry.

rections, as indicated by the arrows in Fig. 1. This action is required for a perfect balun, and holds independent of frequency change.

Broadband Operation

The equivalent circuit for the balun of Fig. 1 is given in Fig. 2. The characteristic impedance of the various lines indicated here were
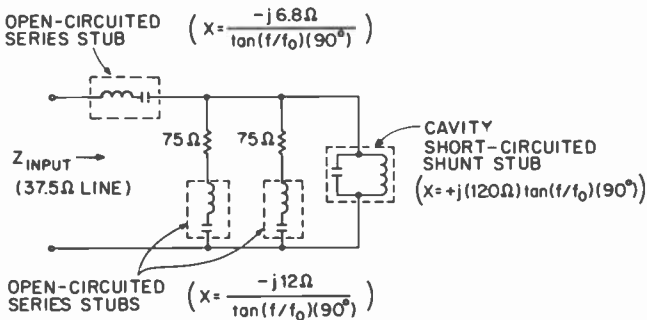
Fig. 2—Equivalent circuit of balun.

arrived at in an earlier balun development requiring a balanced load of 150 ohms. Hence, the characteristic impedances of line C and D are 75 ohms, half the balanced load impedance. Since these lines are in parallel across the unbalanced input, the input impedance is 37.5 ohms. This value of impedance may be converted to a standard 50-ohm line by a number of cascaded quarter-wave transformers in a conventional fashion.

Although not necessarily an optimized design, the following parameters and the data in Table 1 are given to illustrate broadband operation:

$$f_{LO} = 0.4 \text{ GHz}$$
$$f_{HI} = 3.0 \text{ GHz}$$
$$f_0 = \frac{f_{HI} + f_{LO}}{2} = 1.7 \text{ GHz}$$

Balanced Load Impedance $= 150$ ohms

Unbalanced Input Impedance $= 37.5$ ohms

The calculated input impedance characteristic normalized to 37.5 ohms is plotted on the Smith Chart of Fig. 3, and the corresponding VSWR characteristic is on the graph of Fig. 4. It is seen that the VSWR is equal to or less than 1.10 over the 7.5:1 band of 0.4 GHz to 3.0 GHz.

Other values of input impedances may be used by scaling. For example, to obtain a balun to transform from 50 ohms unbalanced to 200 ohms balanced, all impedances given in Fig. 2 are multiplied by the factor, 50/37.5 or 1.333. The highest input impedance achievable may be limited by the tradeoff between the high diameter ratio

Table 1—Diameter Ratios (see Fig. 1) for Various Characteristic Impedances

Characteristic Impedance (ohms)	Diameter Ratio
6.8	$\dfrac{d_2}{d_3} = 1.12$
12.0	$\dfrac{d_5}{d_6} = 1.22$
75.0	$\dfrac{d_4}{d_5} = 3.5$
37.5	$\dfrac{d_1}{d_2} = 1.87$
120.0	$\dfrac{d_7}{d_4} = 7.4$
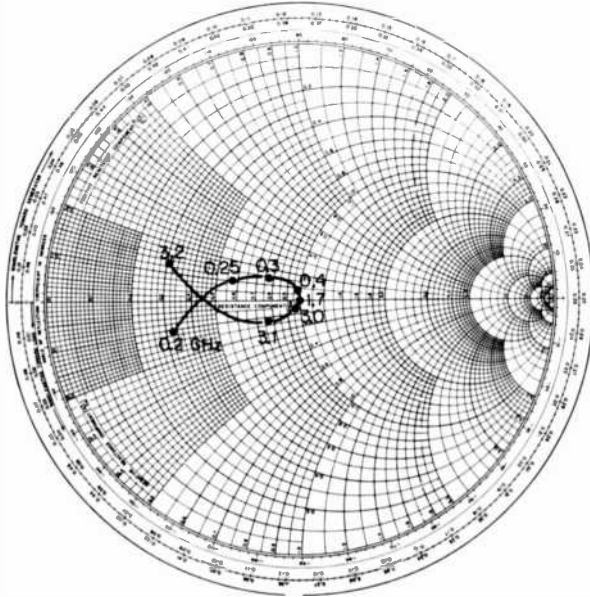
Fig. 3—Balun impedance characteristics.
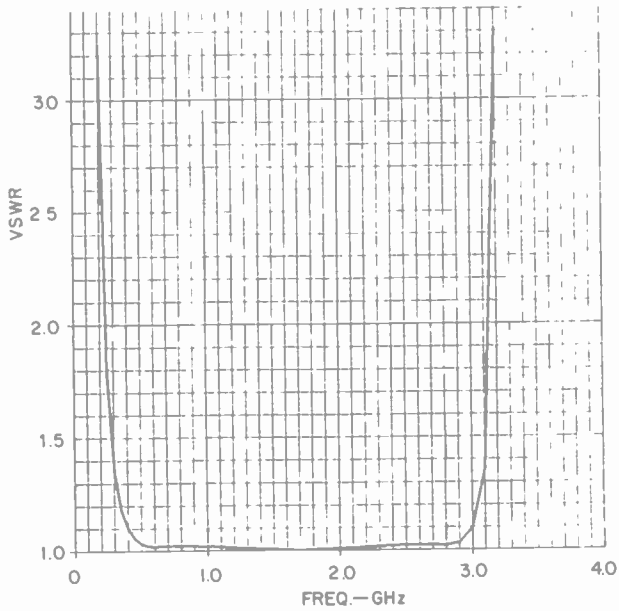
Fig. 4—VSWR characteristic of balun on 37.5-ohm line.

needed for the shunt stub and the greater length of the connecting leads at F in Fig. 1.

Paticularly at lower frequencies (e.g., the HF band), this balun can be designed to handle very high peak powers. This is accomplished by employing sufficiently large coaxial line elements and by installing corona rings at the coaxial line ends.

The small spacing between the inner and outer conductors of the series reactances does not necessarily represent a low-power-handling situation.

From transmission line equations, the voltage V at the open-circuited ends of the series stubs is

$$V = \frac{I\,Z_c}{\sin(f/f_0)90°}$$

where I is the essentially constant input current and Z_c is the characteristic impedance of the stub. Therefore, V is low since Z_c is low for the series stubs.

Alternative Geometries

For the geometric form shown in Section B-B of Fig. 1, both lines C and D are inside of the shunt cavity's outer conductor. Other arrangements are suggested in Fig. 5. Line D is placed outside of the cavity's outer conductor in Fig. 5(a). In Fig. 5(b), the cavity outer conductor is rectangular instead of circular. All of the coaxial line sections of Fig. 1 are made in the form of strip line sections in Fig. 5(c).
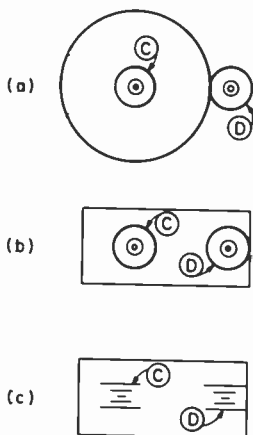
Fig. 5—Alternative balun geometries.

Microwave Tag Identification Systems

Daniel D. Mawhinney
RCA Laboratories, Princeton, NJ 08540

Abstract—This paper reviews the use of microwave devices in security and identification systems. After discussing reasons for the use of a microwave identification system (as opposed, e.g., to optical reader systems), the types of systems available are categorized on the basis of the tag (transponder) power supply as passive, driven, or battery operated. Various code-generation and modulation or conversion techniques used in these systems are also described. Some examples of microwave identification systems currently in use are discussed briefly.

1. Introduction

The use of microwave devices in security and identification systems is growing rapidly as evidenced by increases in available hardware and published articles on the subject. Potential customers are interested in microwave intrusion alarms, motion detectors, speed sensors, distance monitors, and tag readers for integrated security or industrial control systems. The nationwide interests in security because of the crime problem, in automation because of foreign competition, and in environment and worker protection required by OSHA legislation have provided the impetus for this growth, but the capability of relatively inexpensive digital devices and systems to reduce the operating complexities of microwave systems and to account for and correct system deficiencies (such as high false alarm rates) has also been a factor in this expanding interest in microwave techniques for monitoring and measuring tasks.

One specific area of growth for simple microwave systems is that of identification of objects or personnel by some noncontacting technique. In most cases, such identification can be and often is accomplished with bar coded labels and optical readers, such as the uni-

versal product code labels and scanners widely used at supermarket checkouts. Numerous systems for inventory control and part identification in assembly plants are in use, and new applications are probably found every day for these optical or similar magnetic reader systems.

There are, however, certain conditions where optical or magnetic identification systems do not work reliably. Generally, the reasons for the optical system not being usable involve the relative alignment and proximity of the tag and reader or use in a hostile environment where fumes or dirt significantly obscure the readability of the tag. A prime example is the widely publicized use of an optical color bar reader system for identification of railroad freight cars. In addition to the need for all of the readers and the color bar codes to be accurately positioned, the buildup of dirt and grease over the coded labels severely limits the usefulness of the system and has caused several private companies and railroad agencies to investigate other approaches, including the use of microwave systems.[1] The advantages of microwave based systems are the ability to penetrate considerable amounts of smoke or dirt and not to require such precise alignment because they have wide beamwidths compared to optical systems. Wide beamwidth, or observation angle, does however make it impractical to resolve tag patterns anywhere near as small as typical bar code labels.

Some of the interesting applications for microwave systems using coded tags that have come to our attention, in addition to the above mentioned freightcare identification system, include:
- Chassis identification in auto assembly plants.
- Random access location in warehouses.
- Chemical mound volume measurement by radar survey.
- Monitoring of docked tanker movement.
- Personnel identification and access control.
- Automatic vehicle identification at toll booths.
- Identification of military vehicles/armaments.
- Implantation in living tissue to sense vitals.
- Sensing and locating localized fires, floods, etc.
- Vehicle location and tracking systems.

2. Types of Systems

The general form of any microwave identification system consists of an interrogator that transmits from a central location and a number of transponders or tags, ranging in complexity from air

traffic control transponders to anti-shoplifting labels, which return an identifying signal to a central interrogator. The more complex systems require considerable supply power, include sensitive receivers, and generally transmit a high power response at a different frequency than the interrogator. This paper is concerned only with the less complex identification systems using inexpensive low power tags that can be affixed to the object to be located or identified.

These simple microwave tags are categorized as either active or passive, depending upon their need for batteries or other power source. Some of the passive tags do require external power, but the power is obtained by rectifying rf or microwave power from the interrogator or by using the output of an illuminated solar cell. These tags, therefore, are equivalent to a truly passive tag in that no apparent power connection or battery replacement is required. Such tags may be better described as "driven", leading to the classification of tags by the type of power source as passive, driven, or battery operated.

The tags may also be categorized by the type of signal returned to the interrogator. The signal may be a reflection or retransmission of the interrogator frequency with added modulation, it may be a harmonic or converted output from a mixer, or it may be a transmission at an entirely different frequency. Whether the difference is produced by a frequency change or by superimposed modulation of the interrogator frequency, the signal returned by the tag must be clearly distinguishable from the normal signals reflected back to the interrogator by all surfaces and objects within the effective beamwidth of the interrogator antenna pattern. In each case, the output may or may not be coded, depending upon whether the nature of the requirement is identification or only detection. If the return signal is uncoded, the only information returned is that a tagged item is in the interrogator antenna beam; if the return signal is coded, the tag can be identified and, with suitable sensors, can provide other simple telemetry data.

2.1 Passive Tag Systems

The anti-theft label attached to merchandise in stores or books in libraries is an example of an uncoded passive tag.[2] Many of these are inexpensive diode frequency doublers that radiate a very low level second harmonic of the signal from the interrogator. Reception of the doubled frequency alerts the reader to the presence of the tag, and an alarm can be sounded. The tag can be rendered inoper-

ative at the salescounter by burning it open by exposing the merchandise to a short burst of high level rf power. A considerable amount of work was done at RCA Labs several years ago using uncoded tags mounted on license plates for experimental automobile anti-collision systems.[3] The work was later expanded to include driven and battery powered coded harmonic frequency tags for improved target discrimination and data transfer (e.g., license number).[4]

Other coded systems are in use that employ swept frequency interrogators and passive tags.[5] These tags contain various types of resonators, such as LC circuits, cavities, or crystals, which perturb, notch, or enhance the returned signal as the interrogator sweeps through the resonant frequency. By using a wide sweep bandwidth and a number of resonators in each tag, coded data can be transferred to the interrogator by timing the returns against the sweep waveform. If it is known that the tag will be in motion relative to the position of the interrogator, the movement can augment or replace the frequency sweep requirement by arranging a focused microwave beam to physically scan across tags consisting of either alternating strips of reflective and absorptive materials, a bank of resonator elements, or an array of directive antenna elements.[6] The relative positions and spacings of these various elements, analogous to a bar code label, will modulate the reflected signal returned to the interrogator. To be effective, passive tag systems using such swept frequency or scanning techniques must concentrate most of the interrogator output power on the target tag to assure that the amplitude of the returned signal perturbations carrying the code will be detectable in the presence of the normal reflections, which can vary considerably with frequency and position.

2.2 Driven Tag System

To lessen the constraints on coding, sensitivity, and positioning presented by the use of completely passive tags in microwave identification systems, without resorting to the use of batteries, techniques have been proposed and used that transmit to the tag by various means the energy needed to respond to lower-power less-well-directed interrogations with more code flexibility. The most obvious transfer mechanism is the microwave signal itself, and this technique is commonly used, particularly in short range applications, although operation of a tag in a driven mode has been reported with a range of more than one mile.[7]

Several variations of a basic driven microwave tag are shown by the block diagrams of Fig. 1. The interrogator power received at the tag antenna is converted to the dc power needed to operate the code generation, modulation, and (where used) transmitter circuitry of the tag; it may also be used to trigger a tag control function, such as turn-on. For reflection type systems, a significant part of the received power must be reradiated after coding, so the tag may have to switch between collecting and reflecting the incoming energy or be constructed with two antenna elements. Numerous variations are possible depending upon the antenna size, permissable power levels, time duration of exposure, complexity of code, and the span of operating range required by the particular application. The first two of these factors determine how much microwave power could be collected by the tag. Time duration determines how much energy might be stored to provide sufficient power for a code burst where there is insufficient microwave signal for direct real-time powering of the tag circuits. Code complexity and circuit requirements will affect the power used by the tag. The last item, the minimum and maximum ranges, requires consideration of the safe levels of tag and personnel near-field exposure to power densities sufficient for adequate power collection at maximum range.
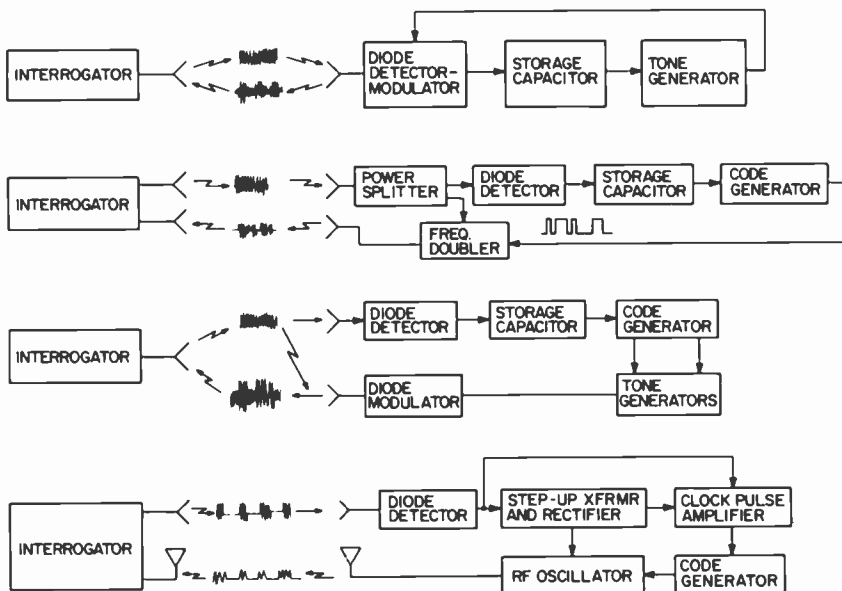
Fig. 1—Four variations of basic driven microwave tag system.

With two specific and several potential requirements for microwave identification systems being considered, several experiments were performed to aid in deciding whether to use driven or battery powered tags. In both cases, it would be impractical to prevent personnel from coming in close proximity to the transceiver antenna, thereby limiting the power density to a safe level of under 1-mW/ cm^2. For tags sized for the specific applications, receiving aperture areas of 10 to 100 cm^2 are reasonable assumptions and, if all the radiated power could be collected, total microwave power levels of 10 to 100 mW would be received. Even a highly inefficient microwave-to-dc conversion process would provide enough power for a complex tag with this much power, but constraints on power density and antenna alignment will severely limit power collection efficiency. Although feasibility studies on an unrelated power transmission program have demonstrated antenna-detector efficiencies as high as 64%, the collection of from 1 to 10% of the transmitted microwave power is a more probable best-case condition for a typical driven tag identification system.[8]

To determine what levels of microwave-to-dc conversion levels may be obtainable with simple tag-compatible detector designs and available diodes, a microstrip mounted HP 5082-2217 Schottky barrier diode was driven at several power levels at 10.5 GHz with various load resistors. Efficiencies varied widely with both drive and load, but 40% was measured at the best combination which is somewhat lower than manufacturer typical data for large signal detectors at 2 GHz. The tests were essentially repeated with the microwave power coupled from the source to the same detector assembly through 15-dB gain horn antennas spaced 11 inches apart. By comparing the output voltages obtained at the several drive and load conditions, it appeared that a 15-dB overall loss occurred, which is about 5-dB more than might be expected from transmission losses using these horns which have 64 × 86 mm apertures. Some of these results are shown by the data plots of Figs. 2 and 3, which also point out the rather low voltage the detector produces at low power levels even into light loads.

Since the load resistance for optimum efficiency is much lower than the expected tag loads, the use of step-up transformers was considered as a means of increasing the generated supply voltage to a level that is more compatible with the tag electronics. Some CMOS devices operate adequately with supply voltages as low as 1 volt if the temperature is not too low, but more circuit flexibility and ambient tolerance is provided at 1.5 to 3.0 volts. To evaluate
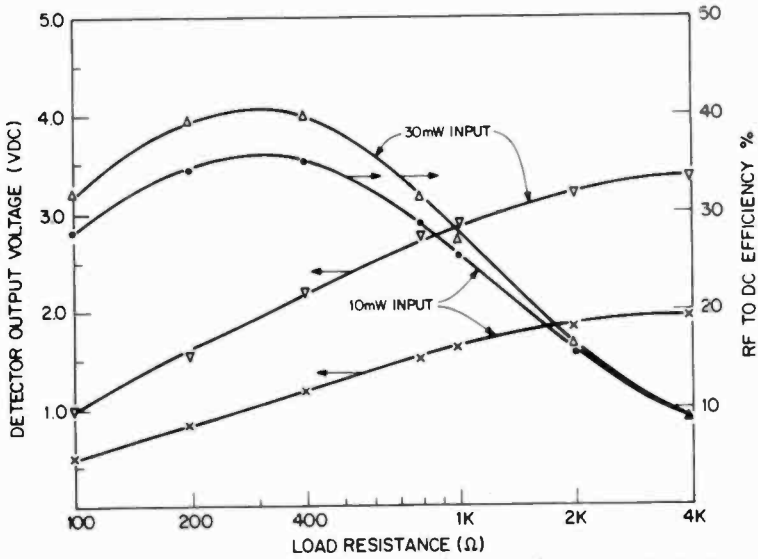
Fig. 2—Detector output for direct connection to microwave power source.
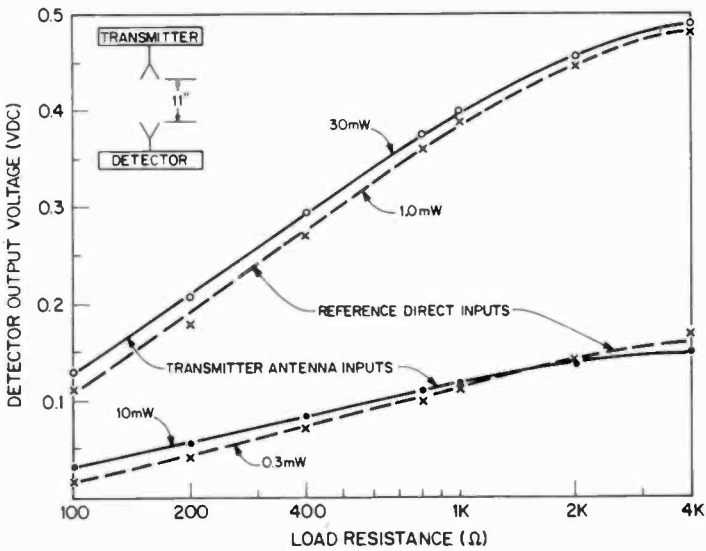
Fig. 3—Detector output with antenna coupling to microwave power source.

the use of transformers, the output of the same microstrip detector assembly was connected to an audio frequency step-up transformer and a bridge rectifier. The detector was driven at a 50% duty cycle from a switched on-off microwave generator both directly and antenna coupled as before. The resulting higher output voltage and a comparison of the direct and horn-antenna drive conditions are shown in Fig. 4. Maximum efficiency occurred at about 300 kilohms which is consistent with a light CMOS tag load.

Oscilloscope photographs (Fig. 5) of the output of a Pico A1580 miniature transformer into 10 kilohm and 1 megohm loads were taken with the microwave power chopped at a 3.5 kHz rate and a peak power level of 30 mW. With the microwave input signal chopped or pulsed, the same average transmitter power is received at higher peak levels where the detector is more efficient without increasing personnel exposure levels. The use of switched microwave power from the interrogator provides the further advantage of a synchronous clock input for the tag, simplifying the code generator. With a pulsed and coded interrogator, the tag need only respond when the interrogator steps through some sequence of pulse rates or widths to which the tag had been uniquely preset.

In addition to the microwave-to-dc converter, the tag could consist of little more than an amplifier to drive a comparator stage followed by a tone-generator phase modulator or direct transmitter. Although pulsed systems would be subject to more extensive FCC limits because of the higher peak power levels and increased frequency spectrum usage, they offer the best overall set of operating conditions for a driven-tag identification system.

2.3 Battery Powered Tag Systems

Simple low-speed CMOS circuitry, such as that used in small digital timekeeping circuits, can operate for long periods with miniature batteries, such as those suitable for use in wristwatches, which have capacities in the order of 10 to 25 microampere-years. Typical wristwatch electronics consist of a 32-kHz crystal oscillator, dividers, latches, and LCD drivers that require about 10 to 25 microamperes, providing about a year of operation before battery replacement. Similar current drains can be maintained in simple tags, such as a single-tone, phase-modulated, reflected-signal type. More complex coding, high frequency modulation, or direct transmission types will require more power.

If the size is not a limitation, larger battery configurations can be used to provide almost whatever capacity is desired. Conflicting
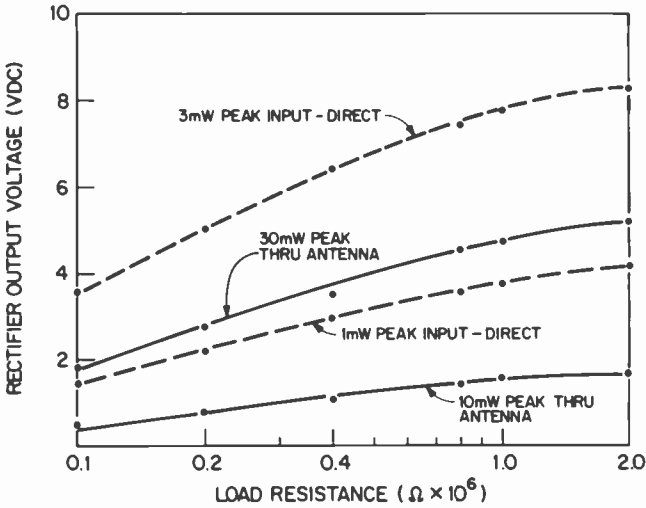
Fig. 4—Microwave-to-dc conversion using step-up transformer and rectifier.

size and power requirements can be satisfied in low-duty-cycle or slow-speed applications by other techniques, such as idling the circuit until an interrogation signal is sensed. With a circuit using a CA3078AT micropower operational amplifier as a level sensor and a CMOS switch driver, a 300-μA load could be turned on in a few milliseconds with an idling current of about 10 μA. A battery powered frequency-doubler-type microwave identification system using
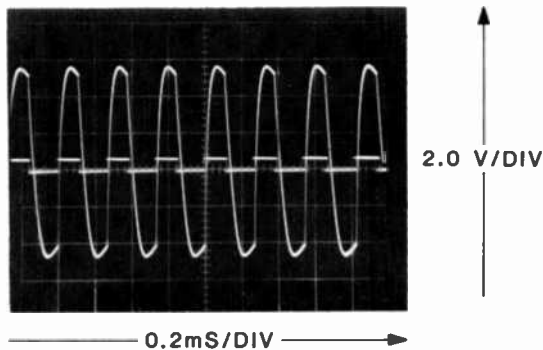
Fig. 5—Output of Pico A1580 step-up transformer into 10 kilohm and 1 megohm loads. Input square wave 3.55 kHz with 30 mW peak power into horn antenna.

approximately 1 mW for code generation and modulation of the diode doubler has been shown to have an operating range of 10 feet and the capacity to respond with more than 100 million codes.[9]

3. Battery Powered System for Coke Ovens

A small developmental program was established with a major steel manufacturing concern to fabricate and evaluate a microwave identification system for use in a large coke oven battery. The process of making coke involves heating bituminous coal in a confined oven to drive out volatile gasses and impurities, leaving a relatively pure fuel for use in blast furnaces. Each of the two active coke oven batteries at their steel mill consists of approximately 80 narrow, refractory-lined ovens arranged side by side. These individual ovens are approximately 30 feet high, 50 feet long, and 18 inches wide with a 32-inch width of refractory brick between each slot-like oven chamber. The overall battery is about 350 feet long. Railroad tracks run the full length on each side providing the means for locomotive driven pusher and catcher cars to be positioned so as to unload each oven at the right time by removing massive doors at each end of the oven and "pushing" the white hot coke into the catcher car with a ram. Each oven position is marked with a number visable to the operators of the pusher and catcher cars who are out of sight of each other but in radio contact. With a computer generated unloading schedule, the operators run the cars back and forth unloading ovens at the prescribed time. The pusher car is also used to level the coal after it is poured into each oven from a movable car that runs along the top of the battery. The time between loading the oven and pushing the coke is about 18 hours.

The eventual goals of the manufacturer are to control the timing more precisely to maximize the productivity of the battery and to prevent the near catastrophic occurrence of misalignment of the pusher and catcher during unloading. For the evaluation phase, the identification system was to be limited to one interrogator positioned relative to the pusher car and ten tags mounted relative to 10 specific oven chambers. At the initiation of each pushing cycle, a printed record of the time and oven number was to be the only readout of the system.

The initial design approach was to use driven tags, since the nominal spacing was to be about 12 inches and the relative positioning would be repeatable within an inch or two. After a preliminary design review meeting, it became apparent that there were other

applications for the system that would involve use at greater separations and less precise positioning. Since there was no objection to the use of batteries needing infrequent replacement, a battery powered design was chosen for the greater versatility it would provide for an evaluation system.

The final configuration of the microwave identification system for the coke oven battery evaluation testing consisted of ten battery-powered tags, one microwave homodyne transceiver, a remote control module, and a commercial 20/40 column printer. The microwave tags, shown in Figs. 6A and 6B, were mounted in a rugged cast aluminum housing along with the same type of printed circuit antenna previously employed in the fabrication of a quantity of locomotive mounted radar speed sensors. This mechanical design has a proven ability to withstand rough handling and severe environmental conditions.[10] A block diagram of the tag circuit is shown in Fig. 7. One of two crystal controlled frequencies, in a preset sequence, is applied to a modulator diode connected to the antenna. The impedance of the diode changes with the applied tone and phase modulates the microwave signal incident upon the antenna. The effect is similar to the generation of a Doppler frequency return from an object in oscillatory motion in the field of a cw transmitting source. Modulation tones of 1000 and 1228 kHz were selected be-
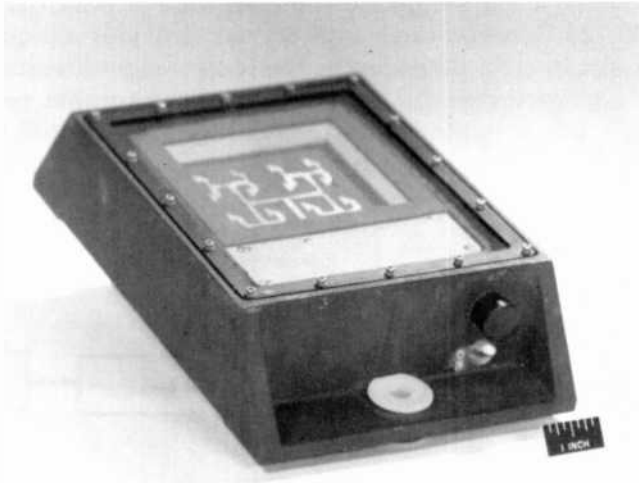
Fig. 6(a)—Microwave tag antenna face.
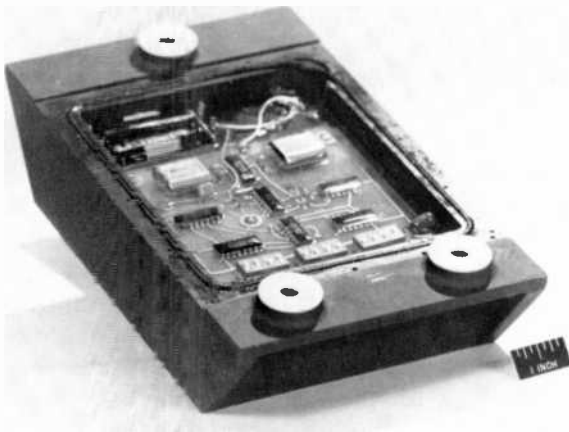
Fig. 6(b)—Microwave tag code-generator board.

cause of availability of inexpensive receivers in the AM band and of specific crystals. The sequence of modulation tone selection can be coded in any desired format; a simple three digit BCD code was chosen which is adequate to identify all of the ovens in the batteries by their actual serial numbers. The clock rate of 1024 Hz, derived from a 32,728-Hz wristwatch type crystal, provides a precise code rate to assist in error detection by the control logic circuits. CMOS circuitry was used because of the low power drain, but no special effort was made to minimize the overall tag current which was 320
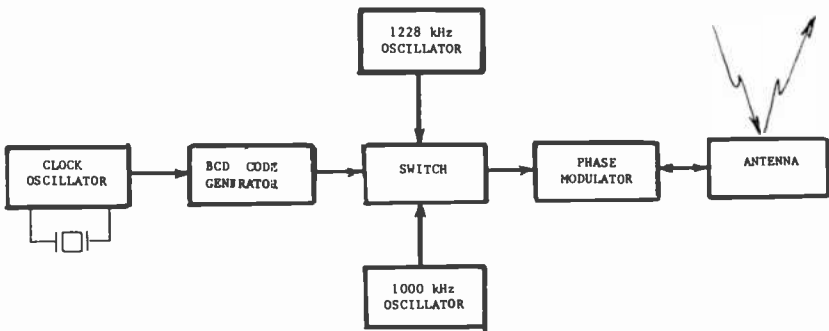
Fig. 7—Block diagram of coded microwave tag.

microamperes. The estimated life of the 3.6-V lithium battery included in the tag is approximately six months.

The microwave transceiver (Fig. 8) also uses the locomotive speed sensor housing and antenna structure because of the hostile environment. Using an X-band TE diode in a coaxial cavity oscillator, the transceiver radiates a cw output power of about 15 mW at 10,525 MHz when the pusher is stopped in position to interrogate the tag. The area of the antenna aperture at the window is about 50 cm^2, and the maximum power density is 0.3 mW/cm^2, which is well within personnel exposure limits. With a transceiver antenna beamwidth of approximately 20°, there is sufficient directivity to separate tags spaced 3 feet apart, with adequate margin for typical pusher/oven misalignment. The reflected signal received by the transceiver antenna consists of the tone-modulated microwave signal from the tag, as well as strong unmodulated reflections from surrounding surfaces. To lessen the effect of the large direct reflections, a balanced mixer driven by a high level LO signal is used to derive the modulation code from the composite return.

The control module contains the modulation receivers, decoding logic, timing circuits, and control logic to operate the system and drive the printer. Two phase-locked automobile AM receivers were used at the front end of provide the needed amplification and filtering to separate the two tones into logic level signals. The excellent shielding, frequency stability, availability, low cost, and quality of phase-locked automobile receivers was the reason for selection of modulation tones within the AM band. There is no transmission of the AM frequencies used in the tag to modulate the in-
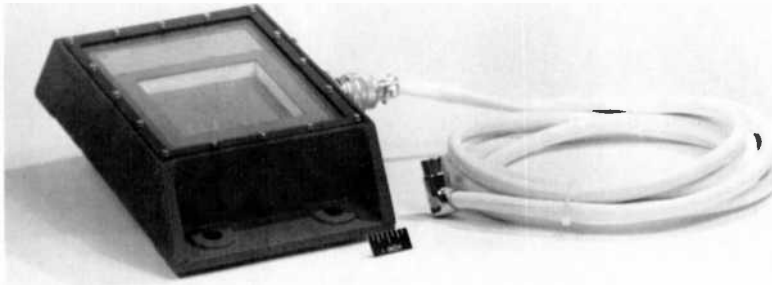
Fig. 8—Transciever for microwave identification system.

cident microwave signal; the mixer output is cabled directly to the antenna jacks of the radios. The oscilloscope picture in Fig. 9 shows the complementary nature of the two receiver outputs for a typical code pattern received by the transceiver from a tag. The remaining circuitry of the control module, shown by the block diagram of Fig. 10, is conventional CMOS digital circuitry to check the validity of the received code, decode the oven number, display the number and the day and time of actuation on the control panel, and transmit the same data in parallel format to a commercial printer. To eliminate any unnecessary microwave signal radiation, the TE-diode bias voltage is maintained below oscillation threshold until the pusher mechanism is in position. The several seconds between the "in position" signal and the actuation of the pusher mechanism is sufficient to read the tag and latch the decoded number, so that when the actuator is operated, the display and printer are also triggered. A sample of typical printouts is shown in Fig. 11.

For the code generated by the tag and expected by the control module, the sequence is a 32-bit word at a rate of 1024 Hz, with the first 12 bits used for three BCD numbers and the remainder as a marker with excess for later extension of the identification system for longer numbers or simple telemetry. To check the legitimacy of the received word, the input to the control logic is stored in a series of shift registers, and several data tests are performed. Three exact words in sequence are required, the time spacing between bits must be within the expected tolerance, and there may be no missing bits, i.e., a signal from either the 1000 or 1228 kHz channel must be received but not both. With these checks, the probability of an er-

1000KHz CHANNEL

1228KHz CHANNEL

————— 5mS/DIV —————▶
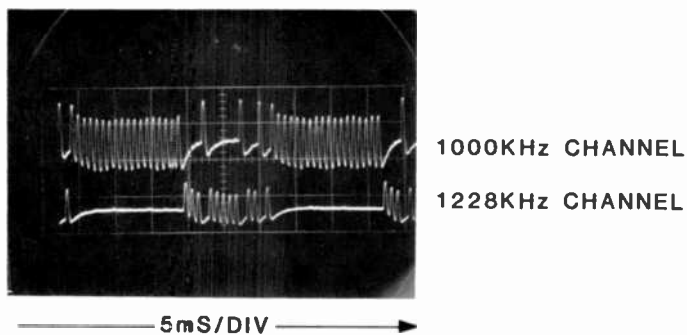
Fig. 9—Output of AM receivers for a typical response code from tag "209".
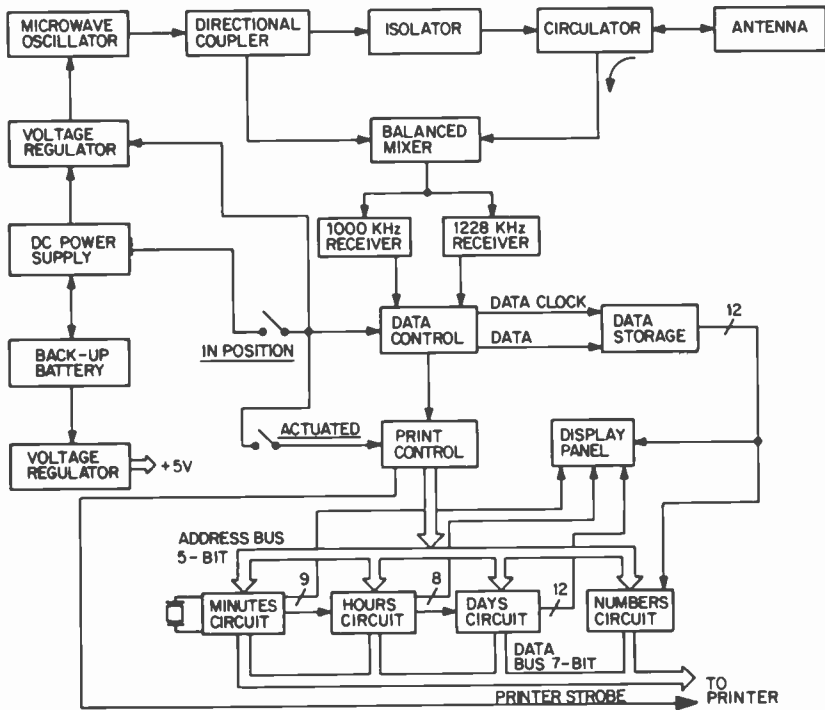
Fig. 10—Block diagram of transmitter/interrogator.

roneous reading is negligible. In case of an improper reading or no tag in place when the actuator is operated, the printer output so indicates by a series of question marks in place of the number.

The overall system is shown by Fig. 12 with the various parts identified. To implement installation in the harsh environment of the coke-oven battery, provisions were included for the transceiver to be operated remotely from the control module. Successful tests were run at spacings from 6 inches to 20 feet, with the gain of the receivers set for optimum performance at each distance. For the intended installation with 12 to 18 inches of spacing, the gain was reduced to prevent overloading of the receiver because of the action of the delayed AVC circuits, which were too fast for some of the longer code gaps. Although the system has not yet been installed on the battery, a number of tests have been run at the steel mill maintenance facility demonstrating basic operation of the system and such peripheral capabilities as identifying moving objects and "looking around corners" using sheet metal reflectors. The latter

```
D243    11:58    #153
D243    11:58    #321
D243    11:59    #272
D243    11:59    #272
D243    11:59    #272
```

Fig. 11—Typical data printout for microwave identification system for use in coke ovens. Shows day, time, and oven number.

capability may be used for interlocking the positioning of the pusher and catcher cars; the former will help keep track of the torpedo railroad cars as they load, transport, and pour molten pig iron around the steel mill.

4. Personnel Tracking System

A different example of a microwave identification system is the Personnel Tracking System developed by the RCA Advanced Communications Laboratory in Somerville, NJ for a complex security application.[11] Most of the earlier discussed applications were limited to observation of one tag at a time with some control over the relative positioning and spacing of the interrogator and tag. This requirement differs in that 8000 different tags, worn by personnel as identification credentials, must be unambiguously identified
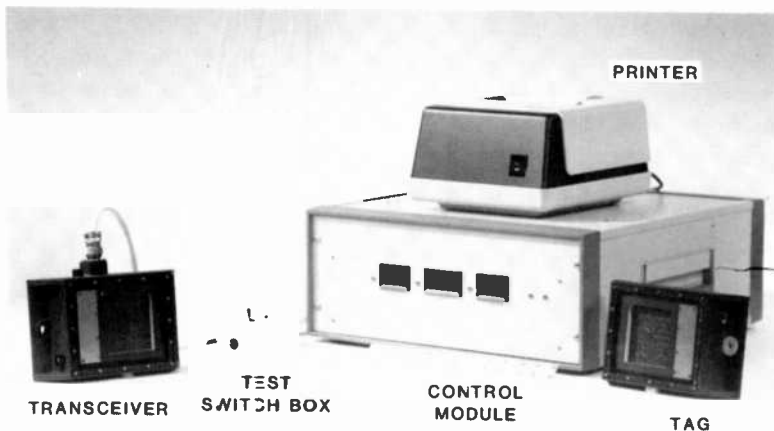
Fig. 12—Components of coke oven microwave identification system.

when any number of them are concurrently in the area under observation by the interrogator. Identification of credentials as far as 15 to 20 feet away is required, but some personnel may pass very close to the interrogator transmitter. The wide dynamic range requirement, lack of predictable location or orientation, and personnel safety considerations make it impractical to use a driven tag for this application. The simultaneous presence of numerous potential credentials favors the use of a transmitter type return signal for more flexibility in coding.

The system developed uses a 1-of-16 tone-modulated pulsed X-band transmitter as the interrogator. Each credential is responsive to only one of these tones and, when triggered by the correct tone, transmits a return pulse at one of eight VHF preassigned frequencies during one specific preset time out of 64 alloted slots. The overall decoding of these three parameters (the interrogator tone and the frequency and time of the response signal) results in a capability to uniquely identify 8192 different credentials with no two of them transmitting the same frequency at the same time. The complete system is described in detail in the referenced article, but some details of the credential microwave and VHF circuits will be presented here.

Ideally the credential was to be worn as an identification badge and the size and weight were of major interest. To minimize the depth of the credential, the use of a microstrip patch antenna was selected for the microwave receiving element. To provide for the uncertainty of orientation, two cross-polarized elements were used, with the detector diode of each connected in series so as to produce an output signal independent of orientation with respect to the interrogator. The orientation of the two rectangular patches is shown by the photographs of the antenna (Figs. 13A and B) which also show the meander line used for the transmit antenna and the VHF oscillator circuitry built on the back surface of the flexible microstrip material. There is a cut in the ground plane on the back surface to facilitate connecting the detector diodes in series; this is obscured in the photograph because of the low-dielectric material used to encapsulate and protect the diodes, chip capacitors, and chokes making up the detector assembly. The overall size of the microstrip antenna structure, built on reinforced teflon-dielectric circuit board material, is about 2.0 × 3.5 inches.

The output of the composite detector is the envelope of the pulse modulated interrogator transmitter. Fig. 14 shows the detected signal levels obtainable from the credential detector when it is
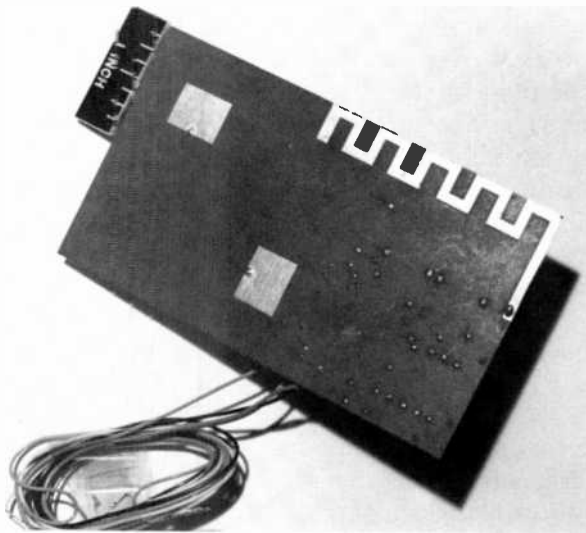
Fig. 13a—Front of antenna for personal identification system showing dual microwave patch receiving and VHF transmitting antennas.

driven by the 10.5 GHz transmitter set for 10-mW peak output power pulses at a 50-kHz rate for both vertical and horizontal orientations of the credential relative to a fixed transmitter. Initially, tuned transformers were used to step-up the detected modulation voltage, providing a relatively large signal for the credential logic. With a 10:1 turns ratio transformer wound on a ferrite core, an output signal of more than 10-mV peak was obtained with any antenna orientation facing the transmitter at the specified maximum range of 15 feet. This arrangement had to be replaced by a low-current transistor amplifier stage because the tuned transformer degraded the rise and fall times of the modulation reducing the timing accuracy necessary to the coding scheme.

The VHF oscillator, operating at approximately 300 MHz, was designed to provide a frequency stability compatible with the SAW filters used in the interrogator receiver with a rapid turn-on capability to assure that the returned signal burst would occur during the allocated interval. Use of crystal controlled oscillators was evaluated but the several milliseconds of turn-on delay was incompatible with the coding technique, which requires that the returned burst of VHF signal be precisely within one of the sixty-four 125-
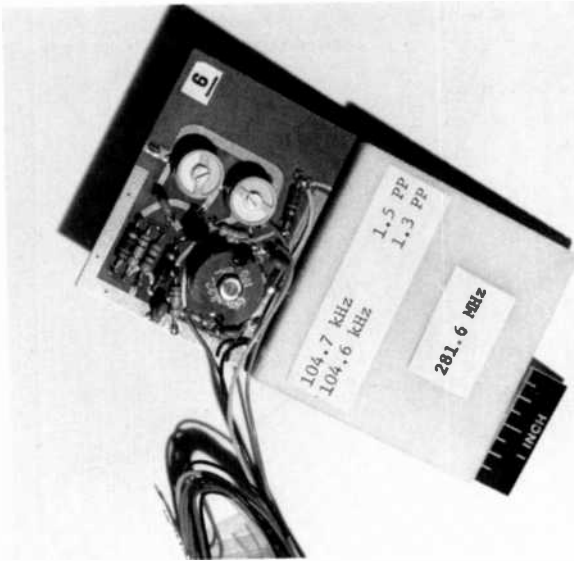
Fig. 13b—Rear of personnel identification antenna showing VHF oscillator and protective encapsulation of detector assembly.

μs-long allocated time slots. Using one-half of the back of the printed circuit antenna board, a simple Colpitts oscillator was built with printed rf lines and variable capacitors allowing each credential to be tuned to any of the 8 predetermined acknowledgement frequencies between 200 and 300 MHz. Consistent start-up delays of less than 25 μs were obtained and the measured change of frequency with expected variations in supply voltage and ambient temperature was less than 2-MHz.

A transferred-electron-effect diode mounted in a temperature compensated coaxial cavity generated the 10.5-GHz power for the interrogator. To avoid the use of a PIN-diode switch, it was decided to directly modulate the oscillator diode. The tendency of TE-diodes to produce switching transients and bias line oscillations when driven through threshold voltage dictated a design that involved pulsing the bias voltage from a level just above threshold, at which voltage no power was generated, to the operating voltage level of 10 V. Such an arrangement provided for rapid turn-on with no dependency on modulation rate. The power was radiated from a printed-circuit dipole array which had been used in several other applications in this frequency band. Any specific coverage require-
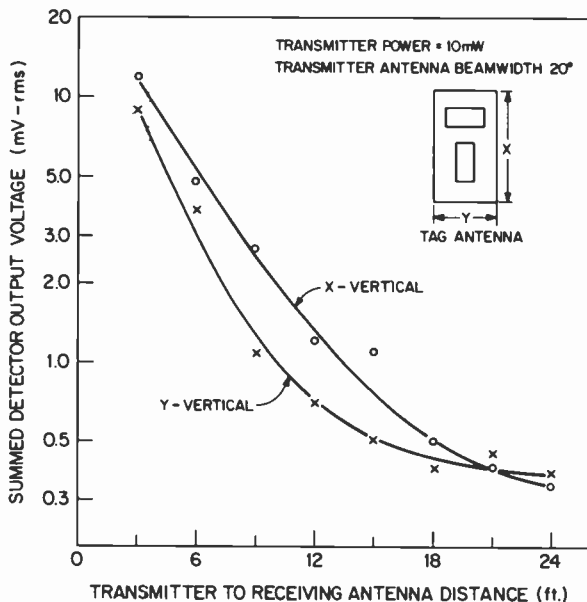
Fig. 14—Sensitivity of dual-polarized tag antenna at two orientations.

ments would involve designing an antenna system suitable for the application; in this case, the 20° beamwidth was considered reasonable for monitoring a typical corridor for control access.

The overall arrangement of the rf circuits used in the personnel tracking system is shown in the block diagram of Fig. 15. A retransmitting battery-operated tag, such as this, approaches a self-responding paging system. In addition to transmitting an identification code, the system could readily be extended to respond with simple messages set in by the wearer or automatically coded by various sensors.

Summary

Microwave identification systems have considerable potential for use in specialized applications where there are positioning and alignment restrictions and in environmentally hostile locations where other systems prove inadequate. These systems are made up of a centrally located microwave interrogating transceiver and a number of small inexpensive tags (which may be passive, driven, or battery-powered), and distinguishable responses may be obtained

RF SYSTEM – BLOCK DIAGRAM
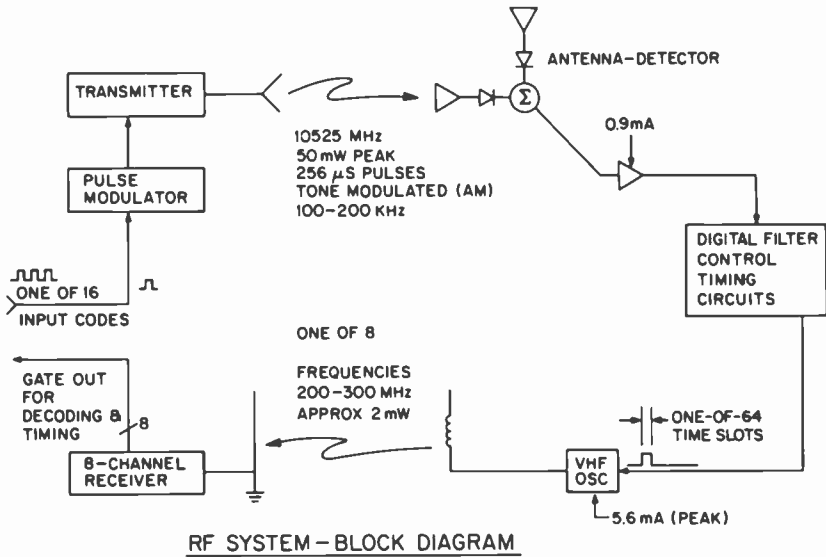
Fig. 15—Arrangement of rf circuits used in personnel tracking system.

by alteration and reflection of the interrogator signal or transmission of a different frequency. Various code generation and modulation or conversion techniques may be used to return identifying data to the interrogator. Examples of the use of microwave identification systems in an industrial area and for a security system have been described.

Acknowledgments

terest and support and R. Kipp for his assistance with customer contacts and discussions.

References:

[1] "Self-Powered Chip Identifies Railcars," *Electronics,* March 24, 1982.

[2] "Electronic Tags Catch Shoplifters," *Design News,* July 20, 1983.

[3] J. Shefer and R. J. Klensch, "Harmonic Radar Helps Autos Avoid Collisions," *IEEE Spectrum,* **10,** p. 38, May 1973.

[4] F. Sterzer, "An Electronic License Plate for Motor Vehicles," *RCA Review,* **35,** No. 2, June 1974.

[5] "SICARD (R) A Device for the Automation of Transport Operations," Siemens publication, Siemens AG-GB ES, Nov. 1978.

[6] R. J. Barber, "21 Ways to Pick Data Off Moving Objects," *Control Engineering,* **11,** No. 1, Jan. 1964.

[7] "Electronic Dogtags Can Pinpoint Position," *Defense Electroncs,* p. 86, Aug., 1981.

[8] W. C. Brown, "The Technology and Application of Free-Space Transmission by Microwave Beam," *Proc. IEEE,* **62,** Jan. 1974.

[9] R. J. Klensch, J. Rosen, and H. Staras, "A Microwave Automatic Vehicle Identification System," *RCA Review,* **34,** No. 4, Dec. 1973.

[10] M. Nowogrodzki, et al., "Radar Instruments: Sensors for Industrial Applications," *RCA Engineer,* **27,** No. 5, Sept/Oct 1982, p. 26–97.

[11] R. H. McEnchern, et al., "Personal Tracking System," *RCA Engineer,* **28,** No. 6, Nov./Dec. 1983.

Miniature Microwave Antennas for Inducing Localized Hyperthermia in Human Malignancies

Robert W. Paglione
RCA Laboratories, Princeton, NJ 08540

Abstract—Three miniature microwave antennas that are each capable of inducing localized hyperthermia in malignant tissues are described. These applicators are used primarily for the interstitial treatment of malignant tumors and for the treatment of choroidal melanoma. The applicators operate at frequencies of 2450 and 5800 MHz with power levels ranging from 1 to 3 watts. Temperature profiles produced by these applicators in a tissue-equivalent material and in animals are presented along with some clinical results.

Introduction

Hyperthermia (the sustained heating of tissues to temperatures of about 42–43.5°C) is now recognized as an experimental therapeutic modality for cancer. Its application to various malignancies at various anatomical sites is presently being explored by many research and clinical centers. One method of producing local hyperthermia is with microwaves. An excellent review of the subject and a description of many RCA-designed applicators was presented in an article by Dr. Fred Sterzer (*RCA Review,* Vol. 42, Dec. '81, p 727). Since then, several new applicators have been designed for heating tumors that are being treated with radioactive implants (these same applicators are also being used to treat brain tumors), for heating brain-stem tumors, and for heating melanoma of the eye.

The applicators to be described are shown in Fig. 1. The probe shown in Fig. 1(a) is used for interstitial heating, that is, the probe (or an array of probes) is inserted directly into a tumor using a plastic or rubber tube as a guide. This applicator has been used for
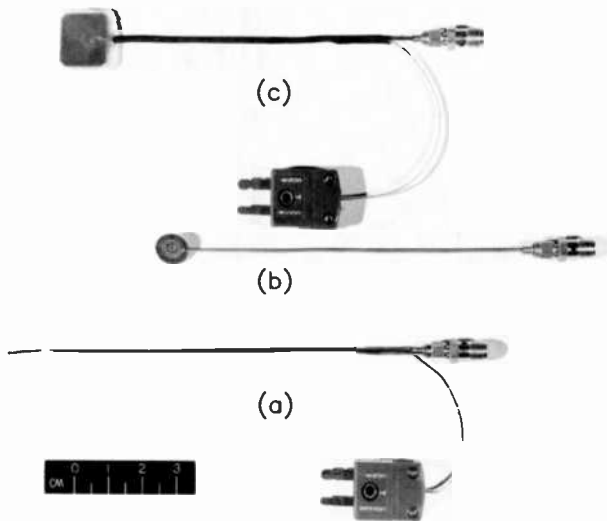
Fig. 1—(a) Miniature coaxial applicator; (b) eye applicator; (c) and patch antenna.

treating brain tumors,[1] breast cancer, head and neck tumors, and tumors in the colo-rectal and vaginal areas. Fig. 1(c) shows a probe designed specifically to treat tumors located on the brain stem. This probe may also prove to be useful at other anatomical sites. The probe shown in Fig. 1(b) is used to treat melanoma of the eye.[2]

Miniature Coaxial Applicator

The probe shown in Fig. 1(a) is constructed from a 12-cm length of 0.86-mm semirigid coaxial line.* The radiating end is formed by removing a length of the outer conductor that corresponds to a quarter-wavelength in the tissues at a frequency of 2450 MHz. A copper-constantan thermocouple junction is epoxied to the shaft of the applicator at the radiating end, and the entire shaft plus the 0.08-mm thermocouple wires are coated with a baked-on medical-grade epoxy.** The diameter of the shaft in the completed assembly is small enough to fit into a 16-gauge guide.

A typical use for these applicators is in the treatment of breast cancer, especially when the tumors are to be treated with radioac-

---

* UT-34, Uniform Tubes Inc., Collegeville, PA.
** #6001-M, Epoxylite Corp., Anaheim, CA.

tive implants. The procedure, known as brachytherapy, consists of inserting plastic tubes through the anesthetized breast using stainless-steel needles (see the sketch in Fig. 2). The needles are then removed, leaving the plastic guides in place. A prescribed number of radioactive pellets are positioned in each tube, and the assemblies remain implanted for aproximately 72 hours. At the end of this period the radioactive pellets are removed from the guides and the microwave probes such as the one shown in Fig. 1(a) are inserted. The microwave power at a frequency of 2450 MHz is adjusted to maintain an indicated temperature of 45°C for one hour. The microwave treatment is only given once as an adjuvant treatment for this protocol to destroy the malignant cells that have only been sublethally damaged by the ionizing radiation. If not heated, these cells would in time recover and again propagate the malignancy.

Another application for these probes, as sketched in Fig. 3, is in the treatment of brain tumors. This effort is being pursued by Dr. Arthur Winter at the Hospital Center at Orange. In this procedure a plastic or rubber guide is inserted into the brain through an incision in the scalp and a burr hole in the skull. The guide is located
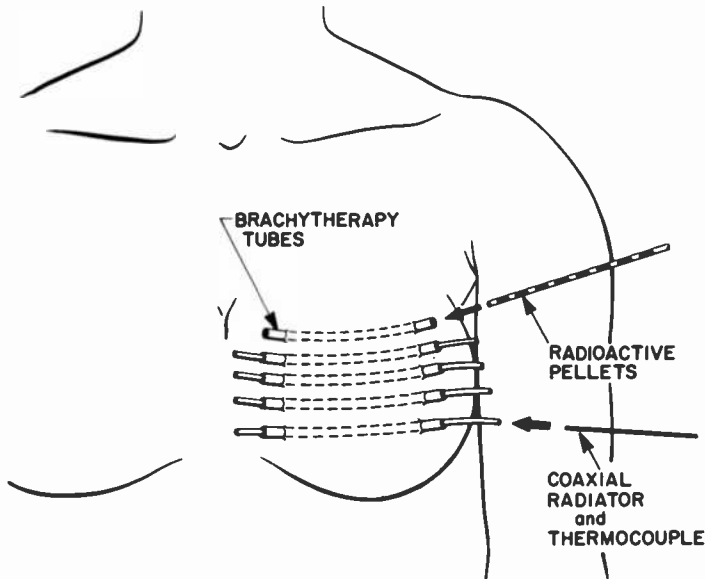
Fig. 2—A typical placement of brachytherapy guides for treating breast cancer. The microwave applicators are inserted into these same guides after the ionizing radiation treatment.
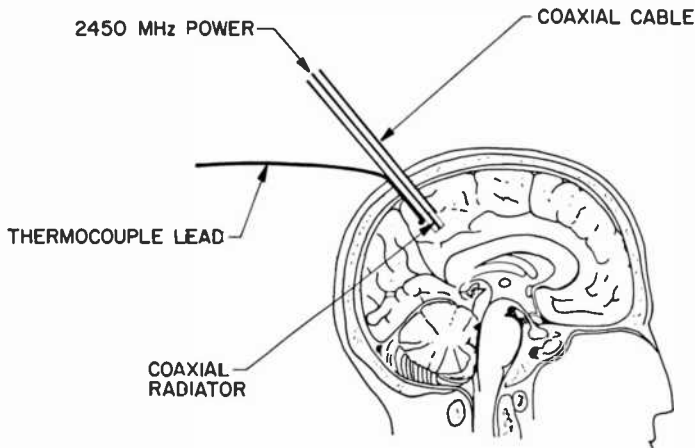
Fig. 3—A sketch of the placement of a miniature coaxial applicator for treating a brain tumor.

in the tumor with the aid of a computerized axial tomographic scanner (CAT-scan). The microwave probe is inserted into the guide, and an indicated temperature of 45°C is maintained for one hour. This treatment is usually given twice a week for one week at intervals of three to six weeks.

Miniature Patch Radiator

The miniature patch antenna, shown in Fig. 1(c), is constructed from a length of 0.86-mm semirigid coaxial line that is terminated on a 0.38-mm thick RT Duroid* substrate (14 × 16 mm). The bottom of the Duroid substrate is a full copper ground plane; the top surface is a copper radiator (13 × 13 mm) that is shorted on one side to the ground plane (see Reference [3] for the details of designing a shorted, quarter-wavelength antenna). The outer conductor of the semirigid coax is soldered to the ground plane; the center conductor of the coax goes through the bottom of the Duroid and is soldered to the radiator at a point that corresponds to an impedance of 50 ohms. A thermocouple junction is imbedded near the top surface of the silicone rubber that is molded around the Duroid substrate. The thermocouple wires and the shaft of the applicator are encased in a length of polyolefin heat-shrink tubing.

---

* #5880, Rogers Corp., Chandler, AZ.

The applicator, which operates at a frequency of 2450 MHz, was specifically designed to treat tumors on the brain stem, located at the base of the brain. Access to the brain stem would be through an opening made in the lower back of the skull. The radiating end of the applicator would be bent so that it looks like a dental mirror, and then inserted and placed against the tumor with a minimum exertion of pressure. The indicated temperature would be maintained at 45°C for one hour.

Choroidal Melanoma Applicator

Choroidal melanoma (a malignancy that grows in the outer vascular tissues of the eye) is the most common ocular malignancy in adults. At present there are two basic courses of treatment for this disease: surgical removal of the eye (enucleation) and local ionizing radiation with low-energy radiation sources such as iodine-125.[4] Since hyperthermia and ionizing radiation act synergistically,[5] it is reasonable to expect that the addition of hyperthermia would reduce the ionizing radiation dose previously required and possibly increase the number of cancer cells killed, thereby reducing the chance of spread or recurrence of the disease. Microwave hyperthermia is well-suited to the treatment of this malignancy since the microwave energy can easily penetrate through the schlera (the fibrous tissues that make up the outer covering of the eye) and selectively heat the underlying tumor. The microwave applicator shown in Fig. 1(b) was designed specifically to achieve this task.

The applicator is constructed using a short length of 0.86-mm semirigid coax that is terminated on a shorted spiral transmission line on a bowl-shaped RT/Duroid substrate. The substrate is 10 mm in diameter and 0.38-mm thick. The spiral transmission line is 6 mm in diameter with a 0.25-mm wide spiral transmission line. The bottom surface of the Duroid substrate is a full copper ground plane. A linear array of three copper-constantan thermocouples encased in a hard epoxy is inserted through the hole in the center of the substrate for temperature monitoring.

The protocol for treating human choroidal melanoma is still in the research stage, however it will most probably be similar to the following: the affected eye will be anesthesized and rotated in a direction that exposes the tumor; the microwave applicator will be placed over the tumor site and a gold bowl containing iodine-125 seeds will be sutured in place over the applicator; the tumor volume will be maintained at an elevated temperature for some period of time; and multiple heat treatments will be given over the total

period of the ionizing radiation treatment. This applicator operates at a frequency of 5800 MHz.

Temperature Profiles

A tissue equivalent material consisting of 69% water, 30% gelatin, and 1% sodium chloride[6] was used to determine the surface and depth heating patterns produced by the various applicators of Fig. 1.

Fig. 4(a) shows the axial and radial heating pattern produced by the miniature coaxial applicator of Fig. 1(a). The applicator was inserted in a silicone rubber cannula* (1.4 mm I.D. × 2.8 mm O.D.) for this measurement. The temperatures were measured with small diameter thermocouples that were pulled through thin-wall Teflon tubes after the tissue-equivalent material had been heated with 2 watts of 2450-MHz power for 30 seconds. The teflon tubes were
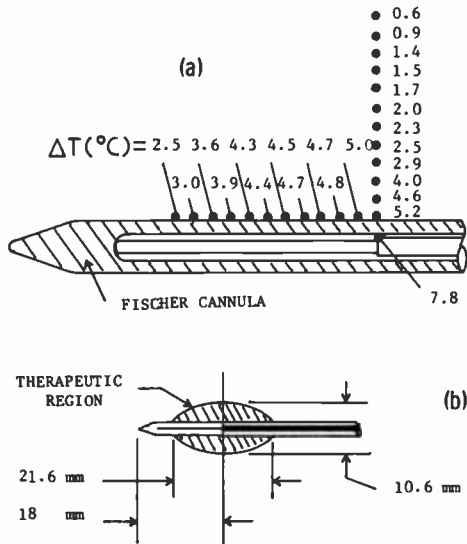
Fig. 4—(a) Measured axial and radial temperature profile of the miniature coaxial applicator in a silicone rubber cannula imbedded in a tissue-equivalent material; and (b) therapeutic region of heating for the miniature coaxial applicator.

* Fischer Ventricular Cannula, Heyer-Schulte, Anasco, Puerto Rico.

positioned alongside and across the cannula. The temperature increases measured at 1-mm intervals are shown in Fig. 4(a), and the therapeutic region is shown in Fig. 4(b). The therapeutic region is defined as the region bounded by the points of temperature increase that are one-half the increase at the center of the antenna. It was also noted that the temperature increase measured by the thermocouple that is epoxied to the shaft of the applicator was 2.6°C higher than the temperature increase measured just outside the cannula. This difference is primarily due to the self-heating of the thin coaxial line—its loss is approximately 0.25 dB/10 cm at 2450 MHz.

The surface and depth heating profiles measured for the patch antenna of Fig. 1(c) are shown in Fig. 5(a) and (b). The applicator heats uniformly within one degree over a 10 × 10 mm area on the surface of the patch and to a therapeutic depth of 7 mm at the location of thermocouple "X".

The surface temperatures and temperatures at depth produced by the eye applicator in Fig. 1(b) are shown in Fig. 6(b) and (c). 1.5 watts of input power at a frequency of 5800 MHz was applied for 30 seconds. The surface heating is fairly uniform over an 8-mm diameter surface area, with the hottest spots occurring at the center of the applicator and near the coax-to-microstrip transition. The therapeutic depth is 3.5 mm, measured at the center of the applicator.

Animal Studies

Two separate animal experiments were performed using anesthetized dogs and the miniature coaxial applicator. In each case the dogs were treated with an array of four applicators that were placed into one hemisphere of their brain through a burr hole in the skull. The applicators were each inside a radiopaque Teflon tube.† Each tube was located on the corners of a square, 2 cm on a side. In addition to the thermocouples on the shafts of the applicators, a thermocouple was placed in the center of the array and another was placed near the optic nerve approximately 6 cm from the center of the array. The temperatures measured in the brain of the first dog are plotted in Fig. 7. The temperatures measured by the integral thermocouples were 1.5°C higher than the temperatures just outside

---

† Field-Lee Biopsy Needle Sheath, V. Mueller, Chicago, IL.
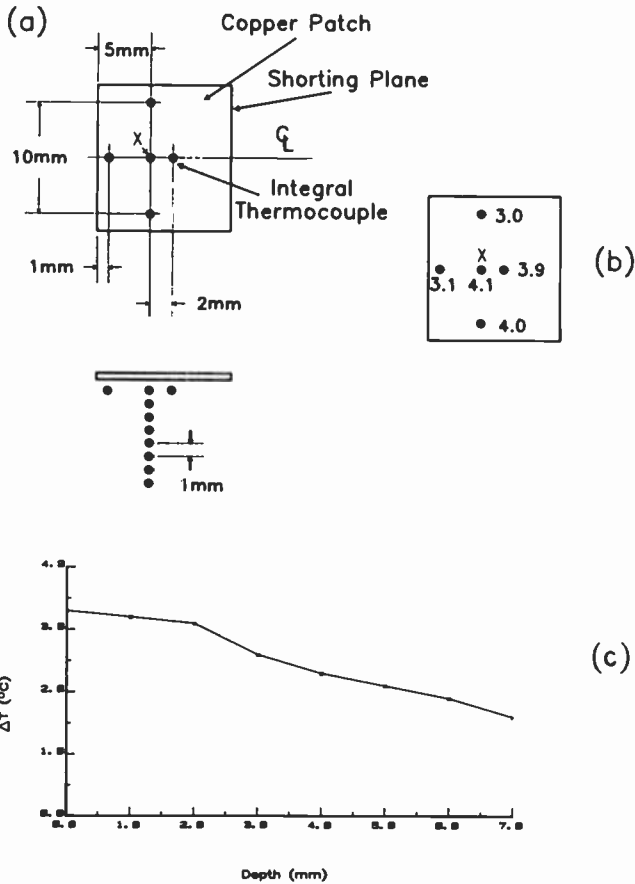
Fig. 5—(a) Location of the thermocouples in the bottom and side views of the patch radiator; (b) temperature increases (°C) measured on the radiating surface of the patch antenna; and (c) temperature increases measured as a function of depth (measured at point "X").

the Teflon tubes. (The wall of the Teflon tube is thinner than the wall of the silicone rubber tube used in the phantom experiments; this accounts for the smaller difference in measured temperature.) If the temperature data for curves 1–4 are reduced by 1.5°C, then curves 1–5 become nearly identical; curve 6 remained below the hyperthermic range during the entire treatment.

A similar experiment was performed on a second dog and, in this case, the indicated temperature was maintained at 47°C. The pathology on both brains showed that the hyperthermia had produced
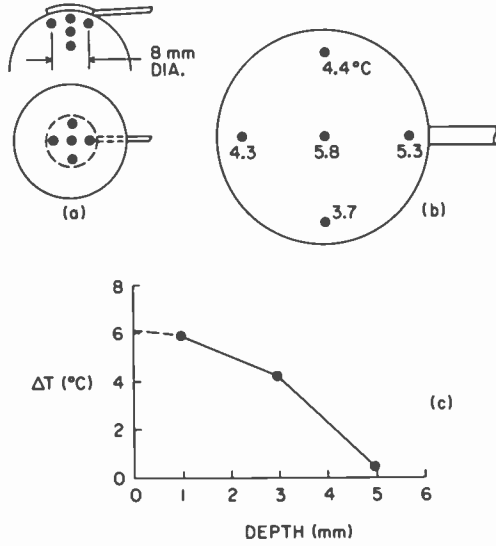
Fig. 6—(a) Position of the thermocouples in the tissue-equivalent material; (b) temperature rise measured 1 mm from applicator surface; and (c) temperature rise in center of applicator measured at depths of 1, 3, and 5 mm.

Time (min)
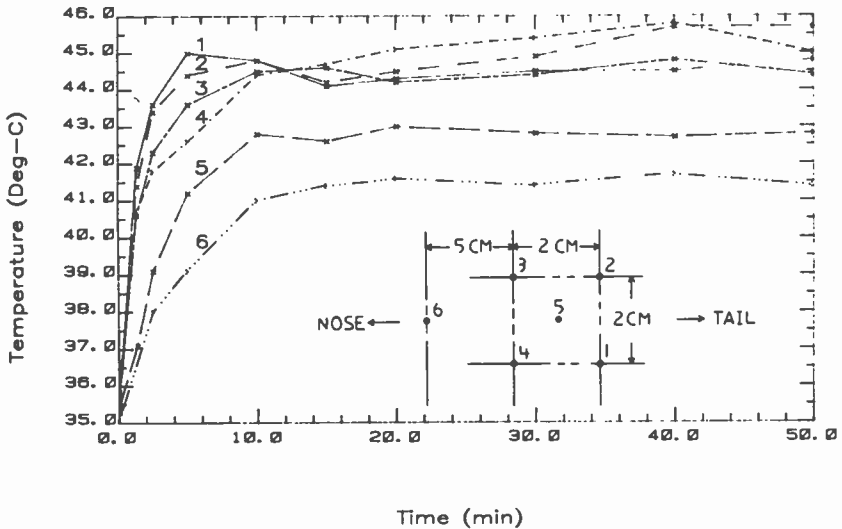
Fig. 7—Temperatures measured in the dog brain as a function of time while heating with an array of four miniature coaxial applicators.

an ellipsoidal lesion (area of necrosis) with edema (swelling) around the area of thermalization.

The eye applicator was used by Drs. Packer and Finger at the Brookhaven National Laboratories to heat the normal eye and tumor-bearing eyes of several 2–3 kg New Zealand white rabbits (the average rabbit eye is 2–4 mm smaller in diameter than the human eye). The tumor is a Green strain of amelanotic melanoma which is placed in and grows from the rabbit choroid. The local growth characteristics and metastatic pattern of this tumor strain is very similar to the human. The normal and tumor-bearing eyes were heated to a maximum intratumor temperature of 47°C for periods of one-half or one hour on each of 1, 3, or 5 consecutive days. The eyes were removed for pathology one month after treatment.

In normal eyes, no adverse effects were noted outside the area of treatment and the schlera beneath the applicator remained intact. Adequately treated intraocular tumors exhibited evidence of cellular damage and cessation of growth in the treated area. Histologic examination of the schlera, adjacent retina, and normal ocular structures showed no apparent adverse effects.

No animal studies have been performed as yet with the patch antenna.

Clinical Trials

Ten patients with malignant brain tumors have been treated by Dr. Arthur Winter at the Hospital Center at Orange, New Jersey, using the miniature coaxial applicator. Each patient has received at least one microwave treatment (indicated temperature of 45°C for one hour) with a single applicator (one patient has now received seven treatments, two of those using four applicators in an array). The case history of the first patient, H.D., is given below:

12/81	Onset of throbbing frontal headaches becoming progressively more severe, unremitting. Progressive loss of vision. Progressive weakness, and an inability to walk.
3/25/82	Frontal craniotomy. Removal of tumor (5 × 10 cm). Tumor site: Dominant left hemisphere. Pathology: Angioblastic meningioma. Post-operative: mild weakness in right leg for 3–4 days, general improvement.
4/15–5/28/82	5600 rd of ionizing radiation to tumor site.
11/82	Severe headaches, increased lethargy and confusion. CT scan shows regrowth of tumor (~5 cm diameter).

12/8,12/10, Microwave hyperthermia sessions.
12/16/82
1/11,1/13/83

Each hyperthermia session used a single implanted applicator in a silicone rubber cannula positioned in the center of the tumor. The tumor was heated each time to 45°C indicated (42.5°C actual) for one hour. A typical plot of indicated temperature and input power as a function of treatment time is shown in Fig. 8. This patient's headaches started to remit almost immediately after the first treatment, and soon he became ambulatory with no headaches and no confusion.

Fig. 9 shows three CT scans of the brain of this patient taken during the course of the hyperthermia treatments. In these scans the nose is at the top of each scan, and the plane shown is approximately at the level of the ears. The bone flap from the original surgery can be seen on the right side of the scans. The bean-shaped black areas are portions of the left and right ventricles—chambers in the brain that contain cerebral-spinal fluid. The ventricles are normally symmetrical about the centerline between the two hemispheres of the brain and they should be approximately the same

Patient: H.D.   Date: 16DEC82
12 cm Probe   2450MHz   9 cm Fischer Cannula
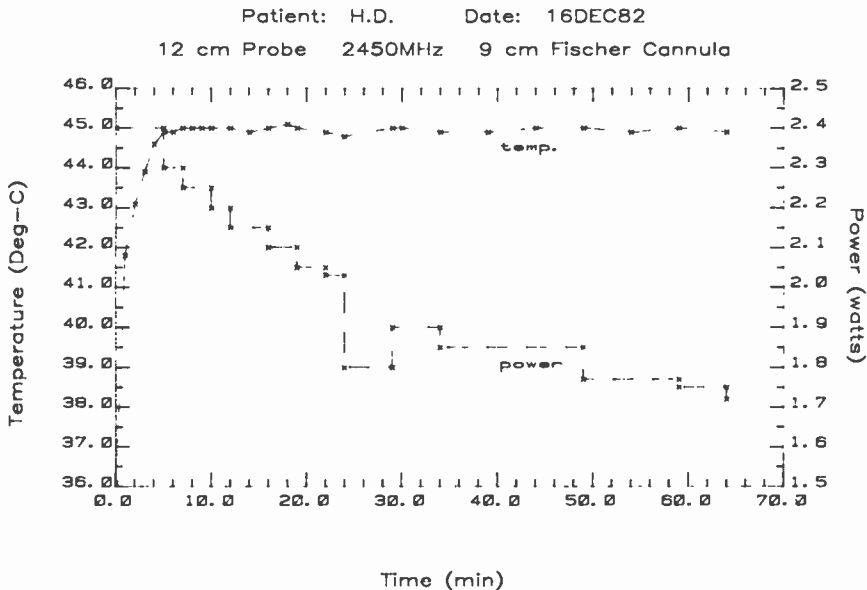
Fig. 8—Treatment temperature response and input power level as a function of time for a miniature coaxial applicator in a silicone rubber cannula in the brain tumor of patient H.D.

(a)

(b)

(c)
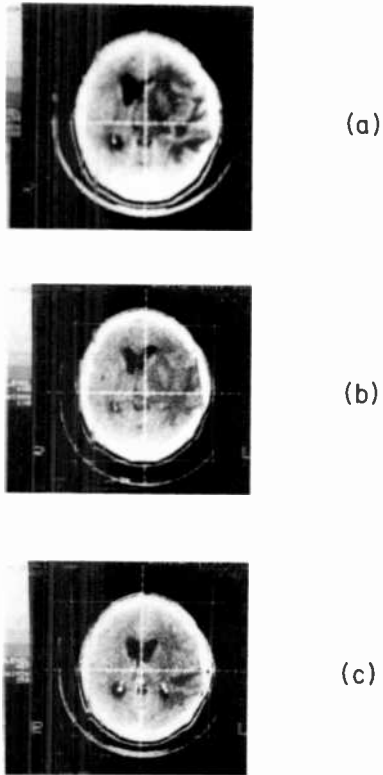
Fig. 9—CT scans of patient H.D. taken (a) prior to the first hyperthermia session; (b) after the second treatment; and (c) after the third treatment.

size. The scan of Fig. 9(a) was taken on 12/7/82, one day prior to the first hyperthermia treatment. Note that the left ventricle (the left side of the head is on the right side of the scan) is nearly occluded due to the pressure exerted by the tumor, and the line of symmetry between the ventricles has been forced beyond the centerline of the skull (the vertical white line on the scan). Fig. 9(b) was taken on 12/14/82, after the second hyperthermia treatment. The left ventricle is opening and the line of symmetry is beginning to shift towards the centerline of the skull. Fig. 9(c), taken after the third treatment, shows that the ventricles are essentially back to normal. Biopsies taken at each time of treatment have shown that there is a progressive change taking place in the tumor cells.

These applicators have also been used by Drs. Botstein, Friedenthal, and Mendecki in conjunction with brachytherapy to treat six

patients at the Montefiore Hospital and Medical Center, Bronx, New York. The patients have tumors located in the breast, on the neck, and in the rectal-vaginal areas. All patients were treated for 72 hours with a prescribed interstitial dose of ionizing radiation followed by a one-hour hyperthermia treatment using an array of four miniature coaxial probes.

The patch radiator and eye applicator have not yet been used on humans, but protocols are being formulated at this time for their future use.

Conclusions

The three applicators described, the miniature coaxial, the patch radiator, and the choroidal melanoma applicator, have all been observed to induce a localized and well-quantified elevation in intra-tumor temperature within the therapeutic range. No adverse effects have been noted during the animal experiments or clinical trials that might preclude the use of these devices, and every indication suggests that these applicators satisfy the requirement for hyper-thermia treatments in their respective areas.

Acknowledgment

References:

[1] A. Winter, J. Laing, R. Paglione, F. Sterzer, and P. Engler, "Microwave Thermotherapy for the Treatment of Human Brain Cancer," *1983 IEEE MTT-S Digest*, 1983, pp 180–182.
[2] P. Finger, S. Packer, P. Svitra, R. Paglione, D. Albert, and J. Chess, "A 5.8 GHz

Ophthalmic Microwave Applicator for Treatment of Choroidal Melanoma," *1983 IEEE MTT-S Digest,* 1983, pp 177–179.

[3] Krall, McCorkle, Scarzello, and Sylles, "The Omni Microstrip Antenna: A New Small Antenna," *IEEE Trans. Ant. and Prop.,* **AP-27,** No. 6, p 850, Nov. 1979.

[4] S. Packer and M. Rotman, "Radiotherapy of Choroidal Melanoma with Iodine-125," *Ophthalmology,* **97,** p. 587, 1980.

[5] J. Kim, E. Hahn, and S. Ahmen, "Combination of Hyperthermia and Radiation Therapy for Malignant Melanoma," *Cancer,* **50,** p. 478, 1982.

[6] M. Stuchly and S. Stuchly, "Dielectric Properties of Biological Substances—Tabulated," *J. Microwave Power,* **15,** No 1, p 19, 1980.

Phase-Locked Injection Laser Arrays with Integrated Phase Shifters

D. E. Ackley, D. Botez and B. Bogner
RCA Laboratories, Princeton, NJ 08540

Abstract—We propose a new type of phase-locked laser array with integrated phase shifters to produce a single, diffraction-limited output beam. By introducing phase-shifting sections either internal to the structure or in the form of selective facet coatings, the phase difference between beams from adjacent array elements can be controlled. The desired operating mode with 0° phase shift between all the array elements can be achieved by varying the optical length of the phase shifters.

Introduction

There is considerable interest in high-power (>100 mW) injection lasers for optical communication links between satellites and spacecraft. For optical communication links to be of practical use, the injection laser source must operate at these high output powers while maintaining good output beam quality. It is also necessary that the sources be modulated at high bit rates (at present 100–400 Mbits/sec, but likely to increase to 1 Gbit/sec or higher for more advanced systems) without significant changes in their output characteristics. A promising candidate to meet these stringent requirements is a phase-locked array of injection lasers that utilizes coupling between adjacent laser devices to lock all the sources into phase, creating a stable far-field pattern at output powers that are the sum of the total available outputs from the individual devices. By combining large numbers of devices it is possible to achieve high output powers while still maintaining reliable device parameters.

Phase-locked arrays with some of the desirable properties described above have already been demonstrated. Arrays that operate in a single longitudinal mode to cw output powers as high as 80

mW have been observed.[1,2] A fundamental problem with the phase-locked arrays demonstrated to date is that nearly all devices have operated in such a manner that the far-field in the junction plane has consisted of two lobes symmetrically located about the facet normal. This far-field distribution is the result of the fact that, because of gain-loss considerations, adjacent stripes tend to operate such that the relative phase difference between them is 180°, which in turn produces the two-lobed far-field. A far-field of this type is undesirable from a systems point of view because it will require excessively large optics to collimate the beam, and the overall beam will still be of poor quality. A fundamental point of investigation is then how to fabricate phase-locked arrays with a phase distribution that results in a single, diffraction-limited beam centered about the facet normal. We propose a new type of phase-locked array that incorporates phase shifters either internally or on its emitting area(s) to produce a device that will operate with a single lobe in the far-field.

Proposed Array Structures

The primary advantage of our proposed array structures will be operation in what will be described within this paper as the in-phase mode. By in-phase mode we mean to describe the operating configuration for phase-locked arrays in which each individual emitter is operating in phase with its neighbors. The two operating modes that are generally observed in the laboratory (i.e., the in-phase and out-of-phase modes) are schematically depicted in the near-field amplitude distributions shown in Fig. 1 for an array with five emitters. If adjacent stripes are operating in phase (i.e., 0° phase shift), their optical fields sum directly and produce a near-field that is similar to a group of uncoupled lasers, as shown in the top section of the figure. However, if the stripe fields operate with a 180° phase shift, the fields will destructively interfere between the stripes and the array field will go through nulls, as is evident in the bottom section of the figure. This difference in array fields is important in the array-mode selection process where gain considerations are significant. In most practical configurations for phase-locked arrays, between two adjacent lasing stripes there is either an absorbing region (c.f., Ref. [1] and [2]) or a region that is essentially unpumped.[3] Since the out-of-phase mode goes through a null in these regions of sharply reduced gain, it will have a smaller overlap with the absorbing regions and, therefore, have a lower threshold modal gain.

FIELD–AMPLITUDE PROFILES

UNCOUPLED
LASERS

0°–PHASE–SHIFT
ARRAY OPERATION

180°–PHASE–SHIFT
ARRAY OPERATION
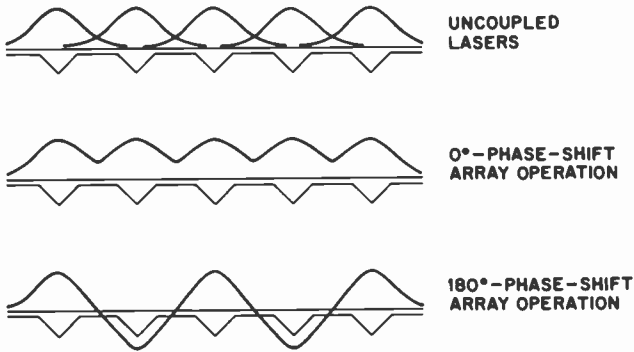
Fig. 1—Field-amplitude profiles for the in-phase (0° phase shift) and out-of-phase (180° phase shift) operating modes of a five-element phase-locked array.

This gain differential results in the out-of-phase mode having a lower threshold than the in-phase mode and is the reason that almost all experimentally realized phase-locked arrays have operated in the out-of-phase mode.

The array structures that we propose will utilize these gain considerations to our advantage. The overall intent of the device design is to utilize the favorable gain considerations to set-up the individual lasing stripes in the out-of-phase mode and then to utilize phase-shifters to change the phase of alternate stripes so that all of them appear to be operating in phase at, or in front of, the lasing facet. The schematic of a few coupled stripes, shown in Fig. 2, de-

PHASE
SHIFTERS

EMITTERS
OUT OF PHASE

EMITTERS
IN PHASE

FACET

FACET
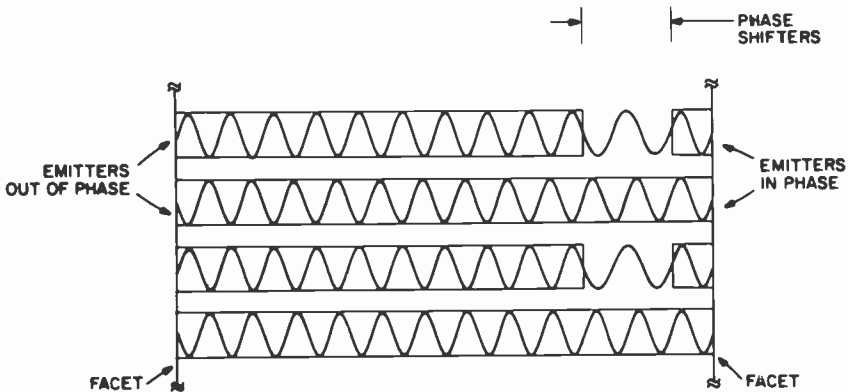
Fig. 2—Standing waves in a few coupled stripes of a phase-locked array showing the effect of the internal phase shifters.

picts the appropriate standing waves set up as they would be for a group of phase-locked injection lasers. It is evident from the diagrams that most of the overall stripe length will configure to operate with 180° phase shifts to minimize the overall gain required for lasing, in the same manner that the usual phase-locked arrays set up in the out-of-phase mode. By fabricating internal phase shifting sections that introduce phase delays equivalent to a 180° phase shift, the individual stripes appear to be in phase at the emitting facets, as can be seen in the figure. It is then evident that, upon Fourier transforming the facet amplitude distribution, the array will produce the desired single lobe in the far-field. The essential requirement to achieve that lasing configuration is that the length of the phase-shifting sections plus the stripe length where the fields are in phase be substantially shorter than the overall stripe length. This enables us to get maximum benefit from the gain discrimination between the in-phase and out-of-phase modes, because most of the length of each emitter will be operating in the favored out-of-phase configuration. An additional desirable and necessary result of using 180° internal phase shifters is that the closure condition for the Fabry-Perot modes is satisfied automatically. If one considers the Fabry-Perot mode as the sum of two traveling waves propagating in opposite directions, the waves see a total phase shift of 360°, which allows them to constructively sum over most of the device length to form a proper cavity mode.

The proposed internal-phase-shift array structure will be a modification of the CSP-LOC arrays recently published by Botez and Connolly.[2] The mechanism by which lateral optical waveguiding in a structure such as this is induced via the interaction of the traverse optical field with the substrate has been well described.[4] It should also be evident that, by allowing the mode to interact with the substrate in the longitudinal direction, some modification of the wave propagation will occur. The result of this interaction is a reduction of the propagation constant of the mode where the active region is in close proximity to the substrate. While there will also be absorption of the mode by the substrate, this can be offset by the gain in the rest of the stripe region. Thus, by fabricating devices with broken stripes to produce unetched regions longitudinally, we can fabricate the phase shifters that we require.

A schematic of the substrate after etching but prior to growth is shown in Fig. 3. To determine the desired length of the phase shifting sections we note that, as is well known, the propagation constant β of an optical mode traveling in a waveguide may be
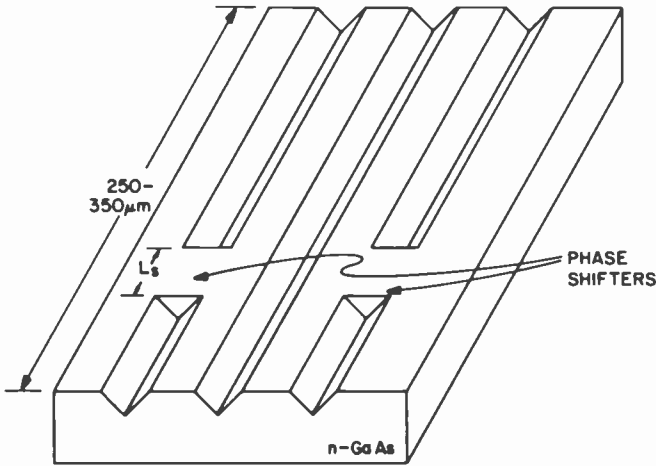
Fig. 3—Etched substrate prior to growth for a CSP-LOC phase-locked array with internal phase shifters.

written in terms of the free-space wavevector k_o and an effective index of refraction n_{eff} as $\beta = k_o n_{eff}$. For the CSP-LOC array we have determined that the difference between the effective refractive indices in the etched and unetched portions of the waveguide is Δn_{eff} $\approx 0.003-0.01$ depending on the active layer thickness and distance to the substrate. This difference is sufficient to fabricate internal phase shifters of reasonable length. As shown in Fig. 3, by utilizing a photomask with breaks in alternating stripes one can fabricate unetched regions in the stripes that will have the reduced effective index of refraction described above. These regions will have slightly different propagation constants and hence a phase delay will be introduced in the alternating stripes. To give a better idea of what the finished device structure will look like when the epitaxial layers are grown we show two cross-sectional cuts through a finished device in Fig. 4. At the facet, all channels are etched; while in the phase shifters, alternate channels are unetched allowing the lasing spots to interact with the substrate.

The propagation along the stripes in the z-direction may be described as

$$\psi(z) \propto \exp(j\beta_c z) \tag{1}$$

in the channel (etched) region. In the phase shifters, the same expression is valid with the propagation constant β_c replaced by a
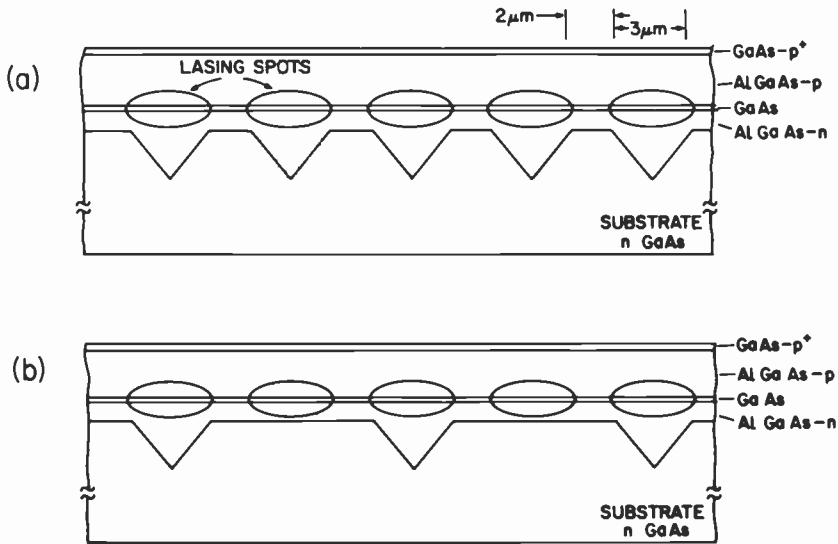
Fig. 4—Schematic cross-sections of a CSP-LOC array with phase shifters taken (a) through the stripes and (b) through the phase-shifting sections.

modified propagation constant β_s. From the expression for the wave propagation, it is obvious that the length of phase shifter L_s required for the required phase shift of 180° is given in terms of the effective index difference as

$$L_s = \frac{\lambda_0}{2(n_s - n_c)},$$ [2]

where n_s and n_c are the effective indices over the shifters and channels, respectively, and λ_o is the lasing wavelength. Of course, if it is desirable, the optical lengths of the phase shifters may be chosen to be odd multiples of π, but these longer shifters would just result in longer devices with no functional advantage. It is evident from the available differences in effective indices for our structure that the phase shifter lengths for a shift of π will be of the order of 30–130 μm, which will probably necessitate making the lasers 250–350 μm long depending on the specific design parameters. The exact optical length of the shifting sections will be somewhat difficult to control, but we can rely on the strength of the phase-locking to pull the propagation constants somewhat and compensate for imperfec-
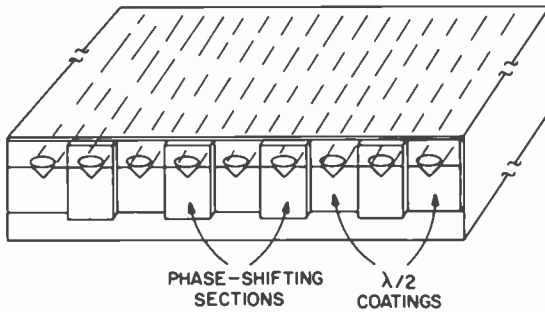
Fig. 5—CSP-LOC phase-locked array with selective facet coatings acting as surface phase shifters. The regions of thicker coating shift the phase of beams propagating through them by 180°.

tions in the device fabrication. To make the overall propagation constants and the required threshold gain equivalent for all the lasing stripes, it may be desirable to utilize phase shifters in every stripe but at opposite ends on alternating stripes to achieve the desired phase fronts at the facet.

An alternate way to fabricate arrays with integrated phase shifters is the use of selective facet coatings to provide the desired phase distribution for the array far-field. An array of CSP-LOC lasers with "broad-area" contact can then be used. As usual, due to gain-loss considerations, the array is assumed to operate in the 180°-phase-shift mode.

By introducing a coating thickness equivalent to a phase shift of 180° on alternate array elements, one can achieve the desired in-phase operating condition for a single-lobed far-field pattern. A schematic of this device is shown in Fig. 5. The selective facet coating can be delineated using photolithographic techniques and, possibly, a two-step coating procedure. Typically one can use $\lambda/2$ passivation coatings on one set of stripes and thicker coatings on the alternate set. The extra coating thickness, t, should provide for a 180° phase shift for the light propagating through the coating versus light propagating through the air. The situation is quite similar to the one shown in Fig. 2 for internal phase shifters. That is, light propagating through the coating of thickness t is delayed by π with respect to light propagating in the air gap between coatings. Then the array far-field distribution will consist of a single main lobe. The value of t for a 180° phase shift is determined by a

formula similar to the one used for internal phase shifters (i.e., Eq.[2]):

$$t_s = \frac{\lambda_0}{2(n_c - 1)}, \qquad [3]$$

where n_c is the index of refraction of the coating and the index of air has been taken as unity. In addition, the thickness of the phase shifter should be a multiple of $\lambda/2$ (in the coating) so that the facet reflectivity is the same for all lasing elements. That condition is

$$t_s = \frac{m\lambda}{2} = \frac{m\lambda_0}{2n_c}, \qquad [4]$$

where m is an integer. To satisfy both Eqs. [3] and [4], the following relationships have to exist:

$$n_c = \frac{m}{m - 1} \qquad [5a]$$

$$t_s = \frac{\lambda_0}{2}(m - 1) = \frac{m\lambda}{2}. \qquad [5b]$$

For $m = 2$, the phase-shifting section has to be $(\lambda_o/2)$-thick and be made of material of index of refraction 2 (e.g., silicon oxinitride). The case $m = 3$ implies a phase-shifter of λ_o thickness and a rather practical value for the index of refraction (1.5). Either SiO_2 or Al_2O_3 $(3\lambda/2)$ coatings could be used. For higher m values the phase-shifter thickness continues to be an integer number of $(\lambda_o/2)$ with the index of refraction of the coating material taking smaller and smaller discrete values. The most practical case appears to be the use of $3\lambda/2$ Al_2O_3 selective coatings fabricated on uncoated or $(\lambda/2)$-coated laser facets. In general, phase-shifting selective coatings can also be applied to phase-locked arrays of gain-guided lasers[3] to force out-of-phase operating arrays to emit a single, narrow beam normal to the facet. There is also an optics analogy in that the set of internal or surface phase shifters we propose can be thought of as a phase grating placed near the array emitting facet.

Summary

By utilizing array structures with integrated phase shifters we expect to achieve devices with stable operation in the desired in-phase

mode. These arrays will be useful for any application that requires high optical power in a diffraction-limited beam.

References:

[1] D. E. Ackley, "Single Longitudinal Mode Operation of High Power Multiple-Stripe Injection Lasers," *Appl. Phys. Lett.*, **42,** p. 152, 15 Jan. 1983.
[2] D. Botez and J. C. Connolly, "High-Power Phase-Locked Arrays of Index-Guided Diode Lasers," *Appl. Phys. Lett.*, **43,** p. 1096, 15 Dec. 1983.
[3] D. R. Scifres, R. D. Burnham, and W. Streifer, "High-Power Coupled Multiple Stripe Quantum Well Injection Lasers," *Appl. Phys. Lett.*, **41,** p. 118, July 1982.
[4] T. Kuroda, M. Nakamura, K. Aiki, and J. Umeda, "Channeled-Substrate-Planar Structure $Al_xGa_{1-x}As$ Lasers: An Analytical Waveguide Study," *Appl. Optics*, **17,** p. 3264, Oct. 1978.

Patents Issued to RCA Inventories—Third Quarter 1983

July

J. G. Amery and R. W. Jorgenson Signal Translating Apparatus for Composite Signal Subject to Jitter (31326)

E. F. Belohoubek Adjustable Phase Shifter (4,395,687)

J. P. Bingham and J. F. Benford Split Phase Stereophonic Sound Synthesizer (4,394,535)

D. Botez High Power Semiconductor Laser (4,393,504)

D. J. Carlson Television Remote Control System for Selectively Controlling a Plurality of External Apparatus (4,392,022)

J. Cowden Method and Apparatus for Holding Styli (4,391,696)

E. R. Ganssle and N. F. Samhammer Modular Spacecraft Structures (4,395,004)

E. R. Ganssle Apparatus for Remotely Indicating Alignment of Male and Female Members (4,395,005)

B. Goldstein, J. Dresner, and D. J. Szostak Method and Apparatus for Determining Minority Carrier Diffusion Length in Semiconductors (4,393,348)

R. N. Gounder Solar Cell Array with Lightweight Support Structure (4,394,529)

J. F. Hacke and L. J. Bazin Balance Modulator with Feedback Stabilization of Carrier Balance (4,393,395)

F. Z. Hawrylo Light Emitting Device with a Continuous Layer of Copper Covering the Entire Header (4,394,679)

L. V. Hedlund and D. G. Herzog Helical Scan Tape Recording and/or Replay Apparatus (4,395,738)

D. D. Holmes Television Ghost Signal Detector with Color Burst Phase Delay Control (4,393,397)

D. D. Holmes FM Counter Detector (4,395,735)

R. N. Hurst Time Changing System for VTR (4,393,415)

G. Kaganowicz and J. W. Robinson Adherent Perfluorinated Layers (4,391,843)

W. Kern and G. L. Schnable Selective Etching of Phosphosilicate Glass (4,395,304)

M. Kumar, R. J. Menna and H. Huang Hybrid Power Divider/Combiner Circuit (4,394,629)

H. G. Lewis, Jr. Digital Video Signal Processing Filters with Signal-To-Noise Enhancement (4,395,729)

P. R. Liller and D. J. Shahan Method of Electrically Processing a CRT Mount Assembly to Reduce Afterglow (4,395,242)

G. N. Mehrotra Audio Processor for Single Channel, Matrixed Two-Channel and Un-Matrixed Two-Channel Signals (4,393,489)

L. W. Nero Television Receiver High Voltage Generator (4,394,722)

T. R. Pampalone Aqueous Developable Poly (Olefin Sulfone) Terpolymers (4,393,160)

J. I. Pankove and C. P. Wu Solar Cell Structure Incorporating a Novel Single Crystal Silicon Material (4,392,011)

S. G. Policastro and D. S Woo Method of Making Low Leakage N-Channel SOS Transistors Utilizing Positive Photoresist Masking Techniques (4,393,572)

G. A. Reitmeier Horizontal-Rate Phase-Change of TV Pixel Distribution Among Multiple Recorder Tracks for Dropout Concealment (4,393,414)

J. K. Rinehart, D. H. Willis, and D. W. Luz Remote Responsive Television Receiver Ferroresonant Power Supply (4,392,090)

J. C. Ruda, R. E. Wartzok, and R. J. Wedekind Active Tape Storage Bin (4,394,951)

O. H. Schade, Jr. Low Drift Amplifier (4,392,112)

R. L. Schelhorn Porcelain Coated Metal Boards Having Interconnections Between the Face and Reverse Surfaces Thereof (4,393,438)

J. M. Shaw Method of Manufacturing Low Resistance Gates and Interconnections (4,392,299)

E. M. Smith Method for Aging a Cathode of a Cathode-Ray Tube (4,392,834)

P. D. Southgate and I. Gorog Defect Detection System (4,395,122)

E. F. Steigmeier and H. Auderset Method for Determining the Quality of Light Scattering Material (4,391,524)

P. J. Straub, Jr. Stylus Cartridge (4,393,487)

J. L. Vossen, Jr. and J. Zelez Transparent Conductive Film Having Areas of High and Low Resistivity (4,395,467)

C. C. Wang and R. F. Bates Bis(Hydroxyalkyl)Disiloxanes and Lubricant Compositions Thereof (4,391,720)

L. Weinberg Memory Addressing Circuit for Converting Sequential Input Data to Interleaved Output Data Sequence Using Multiple Memories (4,393,444)

J. H. Wharton and J. E. James VideoDisc Slow Down Processor with Reverse Color Detector/Corrector (4,395,737)

D. Wierschke Method to Center and Separate Electroformed Replicas from a Matrix (4,394,341)

D. H. Ziegel Technique for Optical Alignment of a Workpiece (4,391,520)

G. S. Zorbalas Rapid Stepping of a Moving Recorded Medium (4,393,421)

August

L. R. Avery Integrated Circuit Protection Device (4,400,711)

V. S. Ban Radiation Heated Reactor Process for Chemical Vapor Deposition On Substrates (4,401,689)

B. F. Bogner Non-Contacting RF Shielding Gasket with Folded Stub Members (4,396,795)

R. J. Bosselaers High Speed Sampling Head (4,399,413)

G. N. Butterwick Photomultiplier Assembly Having Universal Alignment Means (4,396,859)

H. Chen Color Picture Tube Having an Improved Expanded Focus Lens Type Inline Electron Gun (4,400,649)

D. Chin, J. G. Henderson, and R. J. Maturo Signal-Seeking Tuning System with Automatic Bandswitching for a Television Receiver (4,398,303)

N. V. Desai and E. S. Poliniak Method of Forming Pattern in Positive Resist Media (4,396,702)

N. V. Desai and E. J. Gavalchin Method of Forming Resist Patterns Using X-Rays or Electron Beam (4,397,938)

C. B. Dieterich Signal Expander/Compressor with Adaptive Control Circuit (4,398,157)

D. F. Dion and M. J. Cantella Quantized Video Signal Level Interpolator (4,399,411)

R. A. Dischert Controlled RAM Signal Processor (4,396,938)

R. E. Fernsler, S. A. Steckler, and A. R. Balaban SCR Regulator Control Circuit (4,396,873)

R. E. Fernsler, S. A. Steckler and A. R. Balaban Dual Mode Horizontal Deflection Circuit (4,396,948)

A. M. Goodman Method of Making CCD Imagers (4,396,438)

J. A. Guarrachini and J. P. Walentine VideoDisc Mastering Using a Gimballed Air Puck (4,402,072)

J. R. Hale Self-Indexing Insulating Support Rods for An Electron Gun Assembly (4,400,644)

L. A. Harwood, R. L. Shanley, 2nd, and J. Hettiger Video Signal Peaking Control System With Provision for Automatic and Manual Control (4,399,460)

L. V. Hedlund Overcoming Drum Stall in Record and/or Replay Systems (4,396,956)

J. H. Helm Apparatus for Molding a Recorded Disc (4,397,627)

W. Hinn Dynamic De-Emphasis Compensation System (4,400,720)

L. M. Hughes Caddy Loading VideoDisc Player (4,398,281)

R. H. Hughes Color Picture Tube with Means for Affecting Magnetic Deflection Fields in Electron Gun Area (4,396,862)

K. C. Kelleher Bidirectional Pulse Generator for VideoDisc Stylus Deflector Transducer (4,397,014)

K. B. Kilichowski Method of Using a Positive Electron Beam Resist Medium (4,397,939)

S. P. Knight and J. G. Henderson Television Tuning System with Electronic Frequency Adjustment Apparatus (4,402,089)

H. G. Lewis, Jr. Clock Generator for a Digital Color Television Signal Receiver (4,402,005)

F. C. Liu and Y. Kao Impulse Noise Detection Circuit for TV Signals (4,398,210)

E. T. Manson and B. K. Taylor Pickup Arm Suspension for VideoDisc Cartridge (4,400,806)

J. D. Mazgy Wide Temperature Range Switching Circuit (4,400,635)

J. M. Neilson Transistor with Integrated Diode and Resistor (4,398,206)

J. I. Nubani and F. S. Sawicki Method of Processing a Cathode-Ray Tube for Eliminating Blocked Apertures Caused by Charged Particles (4,398,897)

S. Osaka and M. Toda Rotative Motor Using a Triangular Piezoelectric Element (4,399,385)

S. Osaka and M. Toda Rotative Motor Using Plural Arrays of Piezoelectric Elements (4,399,386)

T. R. Pampalone and A. Z. Miller Method of Mounting Electronic Components (4,398,660)

T. R. Pampalone and S. S. Seffren Epoxy Encapsulating Formulation (4,401,775)

K. H. Powers Television Display System with Reduced Line-Scan Artifacts (4,400,719)

A. N. Prabhu and K. W. Hang Conductor Inks (4,339,320)

A. N. Prabhu and K. W. Hang Overglaze Inks (4,401,709)

J. J. Prusak Matrixing Process for the Manufacture of Molded Records (4,400,245)

H. V. Rangachar and K. D. Powell System and Method for Controlling an Etch Line (4,400,233)

G. A. Reitmeier and R. A. Dischert Use of a Single Set of Steering Bits in a Plural Channel System (4,396,937)

P. M. Ritt Method for Removing Insolubilized PVA from the Surface of a Body (4,401,508)

P. Sickert Preparation of VideoDisc Molding Composition (4,399,061)

C. F. Smollin Cascaded Digital Broadcast Transmitter (4,399,558)

R. G. Stewart Gated Parallel Decoder (4,398,102)

G. C. Taylor Method of Forming Metal Lines (4,400,257)

G. E. Theriault Diplexer for Television Tuning Systems (4,397,037)

G. E. Theriault Voltage Controlled Tuner with Voltage Variable Frequency Selective Arrangements Controlled in Response to a Control Voltage Generated Independently of the Tuning Voltage (4,399,559)

L. C. Upadhyayula Signal Switching Matrix (4,399,439)

R. A. Wargo Video Signal Analyzer (4,402,013)

J. H. Wharton Stereophonic Bilingual Signal Processor (4,399,329)

H. A. Wittlinger Voltage Reference Circuit with Feedback Circuit (4,399,398)

O. M. Woodward Non-Contacting RF Shielding Device (4,399,316)

A. Yamada and J. Makino Shutter Control System (4,396,831)

L. H. Yorinks and C. E. Milton, Jr. Broadband, High Power, Coaxial Transmission Line Coupling Structure (4,401,955)

T. D. Yost Synchronizing Pulse Separator (4,400,733)

W. C. Young Filtered Connector (4,401,355)

P. J. Zanzucchi and W. R. Frenchu Device for Multisample Infrared Analysis of Materials in Microgram Quantity (4,399,361)

J. Zelez and J. L. Vossen, Jr. Transparent Conductive Film (4,399,194)

September

J. H. Atherton Input Buffer Circuit (4,406,957)

L. R. Avery Protective Integrated Circuit Device Utilizing Back-to-Back Zener Diodes (4,405,933)

S. C. Blackstone Method of Forming Closely Spaced Lines or Contacts in Semicondutor Devices (4,402,128)

M. E. Breese and A. S. Robinson Controllable Phase Shifter Comprising Gyromagnetic and Non-Gyromagnetic Sections (4,405,907)

E. F. Cave and J. J. Cowden Stylus Coning Fixture (4,403,453)

M. D. Coutts and D. L. Matthies VideoDisc Processing (4,405,541)

M. E. Deangelis System for Removing Shadow Mask Assemblies From Kinescope Panels of Varying Sizes (4,406,638)

E. H. Deirio Ion Implanter End Processing Station (4,405,864)

C. E. Deyer System and Method for Use With Apparatus for Sensing Bare Metal on a Moving Strip of Insulatively Coated Conductive Material (4,404,515)

A. G. Dingwall Active Load Pulse Generating Circuit (4,404,474)

D. W. Fairbanks Stylus Dispensing Apparatus and Method (4,406,381)

S. C. Forberger Method of Printing Intelligible Information (4,403,547)

I. Gorog and L. P. Fox Method for the Manufacture of a Metallic Recording Substrate for a Capacitance Electronic Disc and the Recording Substrate Obtained Thereby (4,402,798)

P. D. Griffis Matching Volume Control Characteristics for Two Channels (4,404,429)

P. D. Griffis Volume Control Signal Coupling Circuit in an Audio Signal Processing System (4,405,948)

K. G. Hernqvist Processing the Mount Assembly of a CRT to Suppress Afterglow (4,406,637)

R. H. Hughes Color Picture Tube Having an Expanded Focus Lens Type Inline Electron Gun With an Improved Stigmator (4,406,970)

S. P. Knight Television Signal Converting Apparatus Providing an On-Screen Tuning Display (4,405,946)

M. E. Labib Capacitance Electronic Disc Stamper Having Improved Stain Resistance and Method for the Manufacture Thereof (4,405,670)

P. A. Levine Electrical Compensation for Misregistration of Striped Color Filter in a Color Imager With Discrete Sampling Elements (4,404,587)

P. T. Lin Internal Caddy Cleaning Apparatus (4,403,369)

A. R. Marcantonio Interrupt Signal Generating Means for Data Processor (4,404,627)

A. Miller Array Positioning System (4,404,465)

M. E. Miller Stylus Assembly (4,404,669)

D. B. O'Leary and G. D. Ross, Jr. VideoDisc Player (270,442)

T. R. Pampalone and K. B. Kilichowski Positive Radiation Sensitive Resist Terpolymer From Omega Alkynoic Acid (4,405,776)

D. H. Pritchard Signal Processing Apparatus Effecting Asymmetrical Vertical Peaking (4,404,584)

J. J. Prusak Apparatus for Producing Disc Records With a Molded-In Center Hole (4,402,660)

L. N. Schiff FM/TV Automatic Gain Control System (4,403,255)

R. L. Shanley, 2nd and L. A. Harwood Brightness Control Circuit (4,404,593)

R. G. Stewart Precharge With Power Conservation (4,405,996)

M. L. Tarng and W. A. Hicinbothem, Jr. Method for Improving Adhesion of Metal Film on a Dielectric Surface (4,404,235)

B. K. Taylor Pickup Arm Retainer for Video Disc Cartridge (4,404,670)

C. H. Thomas, Jr. Digital Sequence Detector (4,404,542)

G. E. Thornberry Vertical Detail Enhancement On/Off Switch (4,403,246)

J. Tults and M. P. French Dual Search Mode Type Tuning System (4,405,947)

M. H. Wardell, Jr. Television Display System Handling and Adjustment Apparatus (4,405,950)

R. H. Williams Wet Processing of Electrodes of a CRT to Suppress Afterglow (4,406,639)

C. M. Wine Servo System for a Video Disc Player Carriage Assembly (4,406,002)

AUTHORS

Donald Ackley received his BS, MS, and PhD degrees from Brown University, Providence, RI, in 1975, 1976, and 1979, respectively. As part of his doctoral studies, he constructed a subpicosecond modelocked dye diode which he used to study the dynamics of hot carriers in amorphous semiconductors on a picosecond time scale. From 1979 to 1982 Dr. Ackley was a Member of the Technical Staff at Hewlett-Packard Laboratories in Palo Alto, CA, where he was involved in the development of high-power phaselocked injection diode arrays for ranging applications. He was also involved more recently with the development of nonplanar single-mode AlGaAs injection diode structures fabricated by organometallic vapor-phase epitaxy (OMVPE). Since joining RCA, Dr. Ackley has continued his interest in phaselocked arrays and has been responsible for specifying a new OMVPE system for the Optoelectronic group. He has been responsible for the internal research effort in diode arrays for pumping Nd:YAG and has also been involved in investigating the reliability of CDH-LOC diodes.

Dr. Ackley holds two patents and has authored a number of publications.

Robert E. Askew was awarded a BSEE degree from the Newark College of Engineering, where he also attended graduate courses. He joined RCA's Microwave Tube Operation in 1961. After an assignment in the pencil tube design and applications group, he worked on microwave solid-state design projects as part of the Advanced Development activity, where he developed solid-state oscillators for radiosonde applications and projectile telemetry transmitters. He transferred to the RCA Solid State Division, where he supervised the fabrication and test of microwave power amplifiers for military and space applications. In addition, he served as type engineer for thick-film hybrid devices used in heart pacers. After a stay at Microwave Semiconductor Corporation in 1977/1978, Mr. Askew returned to RCA Laboratories' Microwave Technology Center, where he is currently engaged in the design of state-of-the-art microwave low-noise amplifiers and down converters and other advanced microwave components.

He has published several papers on microwave solid-state components, and has been awarded two patents. He is a Member of the IEEE and of its Professional Group on Microwave Theory and Techniques.

Bruce F. Bogner earned a BS degree in Electrical Engineering from City College of New York in 1953. In 1958 he received the MS degree in Electrical Engineering from the Polytechnic Institute of Brooklyn. His master's thesis is entitled "Narrowband Microwave Filter Techniques for Strip Transmission Lines." From 1955 to 1958, at Airborne Instruments Laboratory, Mr. Bogner was engaged in research and development of microwave components and subsystems, and, from 1958 to 1960, he was a section manager in charge of

antenna-array design and development at G. B. Electronics Corp. From 1960 to 1964 at Avien, Inc., he was a section manager in charge of the microwave phase of all antenna development, including an ultra-broad-band surveillance-tracking antenna array for Cape Kennedy and a special command antenna for external use on the Apollo space vehicle. After a brief spell as a senior engineer at Loral Electronics, he joined Sperry Gyroscope as a senior engineer to develop electronic-scanning antennas for a nuclear environment, supersonic aircraft, and an air-transportable battlefield radar. From 1966 to 1970, Mr. Bogner was a manager at Jasik Laboratories, in charge of the antenna phase of all programs. Mr. Bogner joined RCA in 1970 as a Principal Member of the Engineering Staff at the Missile and Surface Radar Division, Moorestown, NJ. For five years, he was in the Advanced Microwave Techniques group where he invented a new type of feed for cylindrical arrays of antennas. From 1975 to 1980 he was the system engineer for three elements of the Aegis Combat System, and in 1980 he received the Aegis Excellence Award for outstanding performance in integrating the Navy's new IFF System into the Aegis Command and Control computer system. In the same year, he transferred to RCA Laboratories, Princeton, where he is involved with microwave shielding and susceptibility of the VideoDisc player.

Mr. Bogner is an expert witness in the field of police radar. He has written two books on radar defense and has lectured to both lawyers and the general public on the subject. Mr. Bogner has five U.S. patents issued and four pending. He is a registered Professional Engineer in the State of New Jersey, a member of Eta Kappa Nu and of the NSPE, and a Senior member of the IEEE.

Dan Botez received the BS degree (with highest honors) and the MS and PhD degrees in Electrical Engineering from the University of California, Berkeley, in 1971, 1972, and 1976, respectively. His doctoral studies were concerned with the characteristics of layers deposited over preferentially etched channels in GaAs, as well as with novel optical devices made possible by this method. For one year following graduation, he was a Postdoctoral Fellow at the IBM Watson Research Center. In 1977 Dr. Botez joined the Technical Staff at RCA Laboratories, Princeton, NJ, where his work resulted in "thick-window" high-radiance surface-emitting LEDs and in the development of a novel type of single-mode-stabilized cw diode laser: the constricted double-heterostructure (CDH) laser. The CDH laser has demonstrated cw and pulsed operation up to the highest ambient temperatures ever reported and represents the least temperature sensitive diode laser commercially available. His recent work has resulted in the constricted double-heterojunction large-optical-cavity (CDH-LOC) laser, which to date is the most powerful single-mode semiconductor cw laser and has made possible the optical recording of information at the highest data rates ever achieved.

In 1979 he received an RCA Laboratories Outstanding Achievement Award for contributions to the development of a high-density optical recording system employing an injection laser. In 1982 he was appointed a Research Leader in the Opto-Electronics group. Dr. Botez holds nine patents and has seven patents pending. He is a member of Phi Beta Kappa and the IEEE.

Joseph E. Brown attended the Indiana Institute of Technology during the years from 1967 to 1969 and served in the U.S. Army from 1970 to 1972. He then joined the RCA Laboratories in 1973 where he has been engaged in computer controlled measurements, mechanical design, and assembly of semiconductors for microwave circuits. He is presently a Senior Technical Associate of the Laboratories. His present interests include design of microwave components, and software and hardware development for computer-controlled rf measurement systems.

Hans L. Hartnagel received the Dipl.-Ing. degree in 1960 from the Technical University Aachen, Germany, and the Ph.D. and the Dr.Eng. degrees from the University of Sheffield, England, in 1964 and 1971, respectively. After working for a short period with Telefunken in Ulm, Germany, he joined the Institut National des Sciences Appliquées, Villeurbanne, Rhône, France. He then joined the Department of Electronic and Electrical Engineering of the University of Sheffield, first as a Senior Research Assistant, then as a Lecturer, and later as a Senior Lecturer and Reader. In January 1971 he became Professor of Electronic Engineering at the University of Newcastle upon Tyne, in England. Since October 1978 he has been Professor of High Frequency Electronics at the Technical University of Darmstadt in West Germany.

Dr. Hartnagel has written several books and numerous scientific papers on microwave tubes and on microwave semiconductor devices and their technology and circuits. He has held many counsulting positions while on temporary leave of absence from his University positions.

Karl-Heinz Kreschmer received the Dipl.-Ing. degree in electrical engineering from the Technical University Darmstadt, West Germany, in 1983. Since January 1983 he has been employed at the Institute of High-Frequency Electronics at this University, where he is now engaged in studies on high frequency properties and lifetime prospects of GaAs power FETs.

Daniel D. Mawhinney received his B.E.E. from the Polytechnic Institute of Brooklyn in 1957, and his M.S.E.E. from the Newark College of Engineering in 1965. He was in military service from 1948 to 1952. In 1952 Mr. Mawhinney joined the RCA Microwave Tube Operations Department where he contributed to the development of special microwave equipment used for the test and evaluation of microwave tubes. In 1959 he became Engineering Leader of Microwave Equipment Design with the responsibility for the planning and development of test equipment as part of an integrated manufacturing system. In 1965 he became Engineering Leader of Solid State Systems Development and was assigned to the Lunar Module (LM) team engaged in the design and fabricaton of solid state multiplier units. He developed

a tunnel diode amplifier system for a commercial aircraft radar system and worked on other tunnel diode and parametric amplifier devices. Later, as Manager of Solid State Product Design, he was responsible for product development of various types of microwave solid-state devices including transferred electron oscillators, ferrite components, and microwave integrated circuits. In this position, he directed the design of a series of solid-state TR switches for a high-reliability commercial radar system, an integrated circuit version of a meteorological telemetry oscillator, and an X-band transferred electron oscillator for a lightweight military doppler radar system, and several voltage controlled oscillator subsystems. In 1975 he was transferred to the Microwave Technology Center at RCA Laboratories in Princeton, where he has continued to work on advanced VCO subsystems, hyperabrupt varactor tuned VCO's, frequency memory systems for ECM applications, and FET discriminators.

Mr. Mawhinney is a member of the IEEE and a licensed professional engineer in the State of New Jersey.

Robert W. Paglione received the BSEE degree from New Jersey Institute of Technology (formerly Newark College of Engineering), Newark, N.J. in 1968, and the MEE degree from Stevens Institute of Technology, Hoboken, N.J., in 1972. Mr. Paglione joined RCA Laboratories in 1967 and has been a Member of the Technical Staff since 1970. He is presently affiliated with the Microwave Technology Center as a project engineer engaged in the development of rf and microwave heating equipment for industrial, medical, and scientific applications.

Mr. Paglione has authored many publications in the microwave field and holds five U.S. patents. He is a member of the IEEE and the International Microwave Power Institute.

Barry S. Perlman received a B.E.E. from the City College of New York in 1961, and an M.S.E.E. and Ph.D. in Electrophysics from the Polytechnical Institute of Brooklyn in 1964 and 1974, respectively. He is presently Manager of CAD and Testing in the Microwave Technology Center at RCA's David Sarnoff Research Center, Princeton, N.J. His group is responsible for the management of dedicated computer resources and the development of computer-aided design, automatic test systems, and other computer aides to microwave engineering. He has published more than 40 technical papers in the fields of solid state devices, microwave network design, and computer-aided microwave systems and has received four patents. In 1969, he received an Engineering Achievement Award for advanced device development, and in 1970 he shared an RCA Laboratories Outstanding Achievement Award for his part of a team effort in the development of wideband transferred electron amplifiers. In 1975, he received an Individual Achievement Award for his contribution to computer-aided design and laboratory automation, and in 1983 an Outstanding Achievement Award for his part in the development of the first all solid-state power amplifier for space application.

Dr. Perlman is a member of Sigma Xi, the IEEE, and a registered professional engineer in the State of New York. He is a member of the IEEE Microwave Theory and Techniques, Instrumentation and Measurements, and Computer Societies. He is a charter member and past-Chairman of

the HP-1000 International Computer Users Group and Chairman of its North-American Regional Committee.

Franco N. Sechi received the degree of Doctor in Electrical Engineering in 1964 from the Polytechnic Institute of Milano, Italy. From 1965 to 1968 he was employed by ITT in Milano, where he was concerned with the design of solid-state microwave radio-link equipment. In 1968, he joined RCA, Electronic Components, as a design engineer in the Solid State Product Design Group. In this position he designed transferred-electron oscillators and developed a technique for measuring the impedance of transferred-electron diodes under large-signal conditions. In 1973, he transferred to the Microwave Technology Center, RCA Laboratories, Princeton, NJ. In his present position he is involved in the development of power transistor amplifiers. For his work on linear microwave power amplifiers, he received an RCA Laboratories Outstanding Achievement Award in 1976. He received a second Achievement Award in 1979 for his work on a solid-state radar system for aircraft.

Dr. Sechi has authored papers on transferred-electron oscillators, the thermal and large-signal characterization of microwave devices, and high-power microwave transistor amplifiers. He currently holds six U.S. patents. Dr. Sechi is a member of the IEEE.

Kenneth J. Sleger received the B.S. and M.S. degrees in electrical engineering from Case-Western Reserve University, Cleveland, Ohio, in 1962 and 1965, respectively, and the Ph.D. degree in electrical engineering from Carnegie-Mellon University, Pittsburgh, Pa. in 1971. Since joining the Naval Research Laboratory, Washington, D.C., in 1971, Dr. Sleger has pursued several discrete device and integrated circuit research interests. These include PbS-$PbS_{(1-x)}Se_x$ heterostructure lasers, GaAs FETs, InP FETs, InP/GaAs TEDs and InP mixer diodes. More recently these research interests have been extended to include InP and GaAs monolithic components for microwave and millimeter wave circuits and InP digital ICs. In the course of this device and IC research, Dr. Sleger has also done work on GaAs FET reliability and improved metallizations for GaAs FETs, InP FETs and other microwave and millimeter wave devices. He is currently Head of the High Frequency Devices Section with responsibility for exploratory investigations of new microwave, millimeter wave, and high speed devices and ICs in nonsilicon technologies. His additional responsibilities include technical management of several Navy contractual efforts in the GaAs/InP technology. Dr. Sleger has recently focussed his attention on GaAs technology insertion issues related to future military systems requirements and has authored several papers on the subject.

Dr. Sleger is a senior member of IEEE and a member of the IEEE Electron Devices Society, the IEEE Microwave Theory and Techniques Society, and the American Physical Society.

Oakley M. Woodward received the B.S.E.E. degree in 1938 from the University of Oklahoma Norman. He is Fellow of the Technical Staff at RCA Laboratories. His fourty-two years of professional experience at RCA have been devoted predominantly to antennas of all types and transmission-line components. He has received six RCA Achievement Awards, 41 U.S. patents, and has had 19 papers published.

Mr. Woodward is a member of Sigma Xi.

Binboga Siddik Yarman received his BS degree in Electrical Engineering from the Technical University of Istanbul, Istanbul, Turkey, in 1974 and his MEEE from Stevens Institute of Technology in New Jersey in 1977. He completed his Ph.D. in the area of broadband matching at Cornell University in November 1981. In 1982, he joined RCA Laboratories, David Sarnoff Research Center, Princeton, N.J. He is currently working on new design concepts for broadband, multi-stage microwave amplifiers. His interests include analytic and computer-aided designs of passive and active microwave circuits.

Dr. Yarman is a member of the IEEE and the Turkish Electrical Engineers Chamber.

Index Volume 44, 1983

December

Index to Authors, Volume 44, 1983

STATEMENT OF OWNERSHIP

Statement of Ownership, Management and Circulation (Act of August 12, 1970, Section 3685, Title 39, United States Code).